5-2011

Implementation of Delayed-Feedback Controllers on Continuous Systems and Analysis of their Response under Primary Resonance Excitations

Yousef Qaroush
Clemson University, ykyq78@gmail.com

Implementation of Delayed-Feedback Controllers on Continuous Systems and Analysis of their Response under Primary Resonance Excitations

---

A Dissertation
Presented to
the Graduate School of
Clemson University

---

in Partial Fulfillment
of the Requirements for the Degree
Doctor of Philosophy
Mechanical Engineering

---

by
Yousef K. Qaroush
May 2011

Accepted by:
Mohammed F. Daqaq, Chair
Gang Li
Scott Schiff
Ardalan Vahidi

ABSTRACT

During the last three decades, a considerable amount of research has been directed toward understanding the influence of time delays on the stability and stabilization of dynamical systems. From a control perspective, these delays can either have a compounding and destabilizing effect, or can actually improve controllers' performance. In the latter case, additional time delay is carefully and deliberately introduced into the feedback loop so as to augment inherent system delays and produce larger damping for smaller control efforts. While delayed-feedback algorithms have been successfully implemented on discrete dynamical systems with limited degrees of freedom, a critical issue appears in their implementation on systems consisting of a large number of degrees of freedom or on infinite-dimensional structures. The reason being that the presence of delay in the control loop renders the characteristic polynomial of the transcendental type which produces infinite number of eigenvalues for every discrete controller's gain and time delay. As a result, choosing a gain-delay combination that stabilizes the lower vibration modes can easily destabilize the higher modes. To address this problem, this Dissertation introduces the concept of filter-augmented delayed-feedback control algorithms and applies it to mitigate vibrations of various structural systems both theoretically and experimentally. In specific, it explores the prospect of augmenting proper filters in the feedback loop to enhance the robustness of delayed-feedback controllers allowing them to simultaneously mitigate the response of different vibration modes using a single sensor and a single gain-delay actuator combination. The Dissertation goes into delineating the influence of filter's dynamics (order and cut-off frequency) on the stability maps and damping contours clearly demonstrating the possibility of effectively reducing multi-modal oscillations of infinite-dimensional structures when proper filters are augmented in the feedback loop. Additionally, this research illustrates that filters may actually enhance the robustness of the controller to parameter's uncertainties at the expense of reducing the controller's effective damping.

To assess the performance of the proposed control algorithm, the Dissertation presents three experimental case studies; two of which are on structures whose dynamics can be discretized into a system of linearly-uncoupled ordinary differential equations (ODEs); and the third on a structure whose dynamics can only be reduced into a set of linearly-coupled ODEs. The first case study utilizes a filter-augmented delayed-position feedback algorithm for flexural vibration mitigation and external disturbances rejection on a macro-cantilever Euler-Bernoulli beam. The second deals with implementing a filter-augmented delayed-velocity feedback algorithm for vibration mitigation and external disturbances rejection on a micro-cantilever sensor. The third implements a filter-augmented delayed-position feedback algorithm to suppress the coupled flexural-torsional oscillations of a cantilever beam with an asymmetric tip rigid body; a problem commonly seen in the vibrations of large wind turbine blades.

This research also fills an important gap in the open literature presented in the lack of studies addressing the response of delay systems to external resonant excitations; a critical issue toward implementing delayed-feedback controllers to reduce oscillations resulting from persistent harmonic excitations. To that end, this Dissertation presents a modified multiple scaling approach to investigate primary resonances of a weakly-nonlinear second-order delay system with cubic nonlinearities. In contrast to previous studies where the implementation is confined to the assumption of linear feedback with small control gains; this effort proposes an approach which alleviates that assumption and permits treating a problem with arbitrarily large gains. The modified procedure lumps the delay state into unknown linear damping and stiffness terms that are function of the gain and delay. These unknown functions are determined by enforcing the linear part of the steady-state solution acquired via the Method of Multiple Scales to match that obtained directly by solving the forced linear problem. Through several examples, this research examines the validity of the modified procedure by comparing its results to solutions obtained via a Harmonic

Balance approach demonstrating the ability of the proposed methodology to predict the amplitude, softening-hardening characteristics, and stability of the resulting steady-state responses.

Dedication

I dedicate this dissertation to my wonderful parents, who made all of this possible, for their endless love, encouragement, and patience.

Acknowledgments

My sincerest gratitude and thanks go to Allah for all the blessings he bestowed on me; for giving me this opportunity, the strength and the patience to complete this dissertation by persevering through many challenges and difficulties.

My deepest gratitude goes to my advisor, Dr. Mohammed F. Daqaq, for his guidance and support. I have been very fortunate to have an advisor who gave me the freedom to explore on my own, while, at the same time, guiding me to recover when my steps faltered. Dr. Daqaq's support and friendship have helped me overcome many critical situations toward the completion of this dissertation.

I would also like to thank and acknowledge my committee members, Dr. Gang Li, Dr. Ardalan Vahidi, and Prof. Scot Schiff, for devoting the time to serve on my committee and for their invaluable guidance and patience throughout the process. Sincere thanks also go to the faculties of the Mechanical Engineering Department for their help and for the knowledge I gained during the courses I attend at Clemson University.

I would like to take this opportunity to thank all my friends and colleagues who have given their support and help, especially Prof. Mohammed Al-Nimr, Dr. Mohammad Elyyan, Dr. Mohammad Salah, Mr. Amin Bibo, Mr. Chris Stabler, Mr. Clodoaldo DaSilva, Mr. Ravindra Masana, Mr. Shyam Penyam, Mr. Abdelrouf Abusoua, Miss Tugba Demir, and Mr. Keyur Shah.

My sincerest gratitude goes to my family for their unflagging love and support throughout my life; this dissertation is simply impossible without them. I am indebted to my parents, my father Prof. Kayed and my mother Areefah, my brothers and sisters for their care and love. My sincere appreciation goes to Iyad, Bader and Abdulasalam for their continuous support and great help.

Finally, I am heartily thankful to my wife Wafa'a for her complete support, understanding, and care.

Table of Contents

List of Figures

List of Tables

Chapter 1

Introduction

1.1 Brief History and Overview of Delay Systems

Time-delay, hereditary, retarded, or time-lag represent different descriptions of dynamic systems that do not react instantaneously to actuation signals or whose temporal evolution is based on retarded communications or depends on information from the past. In order to accurately capture their response, mathematical models used to describe these systems must include information about the past dynamics of the states. In general, retardation can arise in many different disciplines including biology, engineering, economics, and ecology; and can be introduced to a dynamic system through one or a combination of the following phenomena [2]:

- *Communication and transport:* Delays can be introduced while information is being transferred from one subsystem through an interconnection to another subsystem. Examples include recycle streams [3, 4], heat exchanger dynamics [5], combustion models [6, 7], congestion dynamics [8, 9, 10], and neural networks [11].

- *Feedback measurements:* These occur in control systems and refer to the pe-

riod of time between the instant the feedback signal is measured and actual system actuation. It is well-understood that within digital circuits, actuation mechanisms, filters, and controllers' processing time; intrinsic time-delays unavoidably bring an unacceptable and possibly detrimental delay period between the controller input and real-time system actuation [12, 13].

- *Biological and population dynamics:* In general, models describing these systems include time delays because the future state not only depends on the current value but also depends on temporal variations occurring in the past. Examples include population growth models [14], pulse circulation models [15], and ecological models [16].

The first systematic work on delay systems is presented in the early 1900's with the epidemiological studies on the prevention of Malaria by Ross [17] followed by the work of Lotka [18] in 1923, who indicated the importance of including time-delays to account for the Malaria incubation times in Ross's model. In 1927, Volterra [19] introduced the retarded forms of predator-prey models used to describe population dynamics; while Minorski, in 1942, was among the first to address the presence of delays in mechanical systems [20]. Since those days, there has been a substantial increase of research activities and funding directed towards understanding the effects of time delays on the stability of various dynamical systems. This established a flourishing new branch of mathematics primarily concerned with stability and stabilization of Delay-Differential Equations (DDEs). Consequently, a variety of analytical, graphical, and numerical methodologies have been proposed and implemented to capture and assess the stability of systems operating with single, multiple, discrete, or continuous time delays.

The effect of time delays can also be seen in our daily life. Consider, for instance, controlling the temperature of shower water. The problem of delayed-feedback becomes evident when the desired comfortable temperature is sought. When the temperature

is too cold or too hot, the shower faucet is turned towards increasing or decreasing the flow of hot/cold water. However, the water temperature does not react instantly to the user input. The delay depends on the pipe length, water pressure, and mixing methods. After a certain amount of time, the user feels the water and decides whether to continue increasing the flow of hot/cold water or to reverse its direction. This temperature control process is usually oscillatory due to the presence of time delay in the feedback perception. Another example lies in the human driving habits of vehicles. Any time delay in the response to road obstacles, sudden changes in the environment, stormy and snowy weather can become destabilizing and of fatal consequences.

1.2 Effect of Delays on Feedback Control Algorithms

It is well-understood that digital circuits, actuation mechanisms, filters, and controller's processing time unavoidably bring about an unacceptable and possibly detrimental delay period between the controller's input and real-time system actuation. If unaccounted for, these inherent and compounding delays might inadvertently channel energy into or out of the system at incorrect time intervals, producing instabilities and rendering the controllers' performance ineffective.

From a mathematical perspective, the presence of delays in the feedback loop renders the characteristic equation associated with the system dynamics of the transcendental type. This transforms the system from a finite to an infinite-dimensional state. In other words, associated with every discrete time delay, the characteristic equation yields infinite number of eigenvalues in the complex plane. In order to create a better understanding of this concept[1], we shall consider the linear stability analysis of

[1]The linear stability analysis presented herein is only meant to build upon and is necessary to

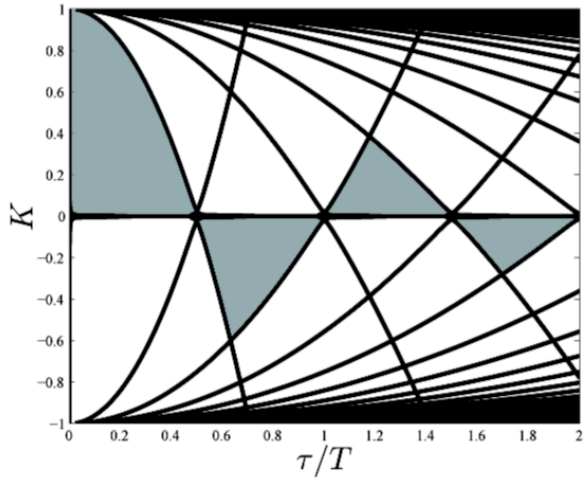

Figure 1.1: Stability map of the equilibrium solutions of Equation (6.1) for $\omega_n = 1$, $\mu = 0.005$, and $T = 2\pi/\omega_n$. Shaded regions represent asymptotically-stable equilibria.

a second-order dynamic oscillator subjected to delayed-acceleration feedback. The equation of motion governing the dynamic behavior of the system is given by

$$\frac{d^2u}{dt^2} + 2\mu\frac{du}{dt} + \omega_n^2 u = -K\frac{d^2u(t-\tau)}{dt^2}, \tag{1.1}$$

where $u \in \mathcal{R}$, $\mu \in \mathcal{R}^+$ is a linear damping term, $\omega_n \in \mathcal{R}^+$ is the natural frequency, $K \in \mathcal{R}$ is the coefficient of the linear-delayed state, loosely referred to as the linear gain, and $\tau \in \mathcal{R}^+$ is a discrete feedback delay.

The characteristic equation associated with Equation (1.1) can be written as

$$(\omega_n^2 + \lambda^2) + 2\mu\lambda + K\lambda^2 e^{-\lambda\tau} = 0, \tag{1.2}$$

where $\lambda \in \mathcal{C}$ is the eigenvalue. Note that, due to the presence of the term $e^{-\lambda\tau}$ in Equation (1.2), the characteristic polynomial becomes a quasi-polynomial of the transcendental type having infinite number of solutions associated with every set of fixed parameters (K,τ). Hence, by virtue of Equation (1.2), the trivial solutions

create a better understanding of the value of this work.

of Equation (1.1) are locally-asymptotically stable if all the eigenvalues, λ, have negative real parts and are unstable if at least one eigenvalue has a positive real part. The fact that the system has infinite number of eigenvalues complicates the stability analysis and requires tracking the location of all these eigenvalues in the complex plan as the system parameters are varied. Considering the case $K < 1$ to guarantee the stability of the delayless system, one can find the stability boundaries in the (K,τ) space by setting the real part of the eigenvalues equal to zero, i.e. letting $\lambda = \pm i\omega$ in Equation (1.2), then separating the real and imaginary parts of the outcome. This yields

$$\begin{aligned} \tau_{cr} &= \frac{1}{\omega_{cr}} \left(\tan^{-1} \frac{\omega_{cr}\mu}{\omega_{cr}^2 - 1} + n\pi \right), \qquad n = 0, 1, 2, ... \\ K_{cr} &= \pm \frac{\sqrt{\omega_{cr}^2\mu^2 + \omega_{cr}^4 - 2\omega_{cr}^2 + 1}}{\omega_{cr}^2} \end{aligned} \tag{1.3}$$

where τ_{cr}, K_{cr}, and ω_{cr} denote, respectively, the delay, gain, and response frequency at the stability boundaries. For a given frequency, ω_{cr}, Equations (1.3) can be solved for the delay τ_{cr} and the associated gain at the boundary, K_{cr}. To better visualize the stability of the equilibrium solutions, the gain-delay space is mapped into stable and unstable regions as depicted in Fig. 1.1, where shaded regions represent gain-delay combinations leading to asymptotically stable equilibria. It is clear from the figure that the presence of delay in the closed-loop system introduces different stability pockets. As the delay increases, the gain that stabilizes the system decreases initially then increases again then decreases (in a periodic manner). The size of the stability pockets shrinks as the delay increases.

The preceding technique for the stability analysis of delay systems is known as the graphical approach or the D-decomposition technique [21]. This approach works well when the system has one or two states at most. For larger number of states, many stability analysis techniques have been proposed and implemented. Among those are the frequency-domain techniques which have been analyzed in the manuscripts

by Stepan [22], Niculescu [2], Kamen [23], and Gu [21]. These techniques include, but are not limited to, the two variable criterion, the polynomial elimination methods [24, 25, 26], the pseudo-delay techniques [27], and the iterative approach [28]. In addition, time-domain methodologies have also been implemented to estimate the stability margins of delay systems. These include the constant matrix approach [29], the robust control approach [30, 2], and, most recently, the Lambert function approximation [31]. More details on the stability techniques used in this work is available in Chapter 2.

1.3 Motivations

The motivation behind this work are two folds: the first is associated with the implementation of delayed-feedback controllers to suppress harmful oscillations of structures using a single sensor single actuator approach. The second deals with the adaptation of the Method of Multiple Scales [32] to construct analytical solutions that aid in understanding primary resonances of externally-excited weakly-nonlinear delay systems. Following is a detailed discussion of these motivations:

1.3.1 Implementation of delayed-feedback control algorithms on structures:

Despite the fact that delays in the feedback are thought to be detrimental to controllers' performance and are usually associated with instabilities; large number of research efforts are currently directed towards implementing delayed-feedback control algorithms for vibration mitigation and external disturbances rejection on various dynamical systems [33, 34, 35, 36, 37, 38, 39, 40, 41, 42]. Delayed-position, -velocity and -acceleration feedback are some examples of such algorithms. This idea

arguably started with the work of Abdallah et al. [43] who showed that delayed-positive feedback can actually stabilize oscillatory systems. Since then, this same concept has received significant attention in the open literature because of the ability of such controllers to augment inherent system delays resulting from filters, processor's dynamics, computations, and feedback loops into a larger and stabilizing delay period. Furthermore, it has been shown that delayed feedback algorithms are capable of producing larger damping in systems for smaller control efforts.

Many researchers have explored these advantageous characteristics to augment the inherent destabilizing feedback delay into a fixed and possibly larger and stabilizing delay period. This started with a series of studies by Jalili and Olgac [33, 34, 35], who illustrated that, by choosing a proper gain-delay combination, the effective quality factor of the system can be decreased considerably producing larger damping which can be effectively utilized to mitigate vibrations of externally-excited systems. In other demonstrations, Hosek et al. [44] and Olgac et al. [40] implemented time-delayed velocity feedback control on torsional mechanisms. Robinett et al. [45] also employed a lag-stabilized force-feedback controller for damping initial and residual oscillations of a planar, cantilevered, flexible arm. In recent years, Masoud et al. [36, 37, 38, 39] successfully implemented delayed-acceleration feedback control to reduce pendulations of suspended cargo on ship-mounted cranes, structural boom cranes, and telescopic cranes. They showed that delayed-feedback controllers have a superior performance over traditional feedback algorithms.

Despite all the previously mentioned examples, a major concern remains in the implementation of these controllers on multi-degree-of-freedom (MDOF) and distributed-parameters structural systems. Specifically, as seen in Equation (1.2), due to the transcendental nature of the resulting characteristic quasi-polynomial associated with the delay-differential equation that describes the dynamics of every vibration mode, [46, 47, 48]; a gain-delay combination that stabilizes a given vibration mode can easily destabilize other vibration modes. Therefore, as the number of modes

increases, the stability pockets in the gain-delay space shrink significantly and the complexity of finding a gain-delay combination that can simultaneously stabilize multiple vibration modes increases [49].

As an example, consider the problem of utilizing a delayed-feedback algorithm to mitigate the vibrations of a homogeneous, uniform thin beam due to some initial conditions. Using Euler-Bernoulli's beam theory, the partial differential equation that describes the response characteristics can be written as

$$\begin{aligned} &EI\frac{\partial^4 w(x,t)}{\partial x^4} + c\frac{\partial w(x,t)}{\partial t} + m\frac{\partial^2 w(x,t)}{\partial t^2} = Kw(s_0, t-\tau), \\ &w(x,0) = f(x), \quad \dot{w}(x,0) = g(x). \end{aligned} \tag{1.4}$$

with some boundary conditions depending on the type of support at either end of the beam. Here, $w(x,t)$ represents the beam deflection in space x, and time t; E is the beam's modulus of elasticity, I is the area moment of inertia, c is a viscous damping coefficient, and m is the mass per unit length of the beam. The terms on the left-hand side of the equations are, respectively, the stiffness, damping, and inertia terms. The term on the right-hand side represents the delayed-position feedback control law, which is obtained by measuring the deflection of the beam at a distance s_0, multiplying it by a proper gain K, and delaying it by a period τ. A Galerkin expansion of the form $\sum_{i=1}^{\infty} \phi_i(x) q_i(t)$ can be used to discretize Equation (1.4) into an infinite number of linear second-order oscillators in the form

$$\ddot{q}_n + 2\zeta_n \omega_n \dot{q}_n + \omega_n^2 q_n = K\alpha_n \sum_{i=1}^{\infty} \phi_i(s_0) q_i(t-\tau), \qquad n = 1, 2, 3, .., \infty, \tag{1.5}$$

where ω_n and ζ_n are, respectively, the modal frequencies and damping ratios; and α_n are constants describing the relative projection of the control effort on the different vibration modes. Keeping a single mode in the series expansion, the characteristic

quasi-polynomial of the response can be written as

$$\lambda^2 + 2\zeta_1\omega_1\lambda + \omega_1^2 - K\alpha_1\phi_1(s_0)e^{-\lambda\tau} = 0, \tag{1.6}$$

where λ represents the eigenvalue. Equation (1.6) is transcendental and has infinite number of solutions (eigenvalues) associated with every single gain and delay combination. It has been shown by various researchers that a gain-delay combination can be easily found to not only stabilize system (1.6) (all λ's are in the left-hand side of the complex plane) but also increase the effective damping in the response. However, it was noted that, this same gain-delay combination can become destabilizing if the second or higher modes are kept in the expansion [50, 51]. The higher the number of modes included, the harder it is to find a single gain-delay combination that stabilizes the response. Figure 1.2 presents the rightmost eigenvalues for the first and second modes. It can be clearly seen that for the same first-mode stabilizing control parameters (K and τ), the emergence of the second mode dynamics renders the time-delayed feedback response unstable (i.e., the rightmost eigenvalue is now located on the right half of the complex plane). As such, one of the main objectives of this Dissertation is to derive methodologies that permit implementation of delayed-feedback algorithms to suppress multi-modal oscillations od infinite-dimensional structures. Details of this objective are available in Section 1.4.

1.3.2 Primary resonances of weakly-nonlinear delay systems:

Despite the significant body of research that deals with the stability and stabilization of delay systems, most of these efforts are directed towards characterizing the stability of the free response by proposing various methodologies to predict and estimate the location of the eigenvalues relative to the imaginary axis [52, 53]. Little attention has been paid to understand the effect of time delays on the response of

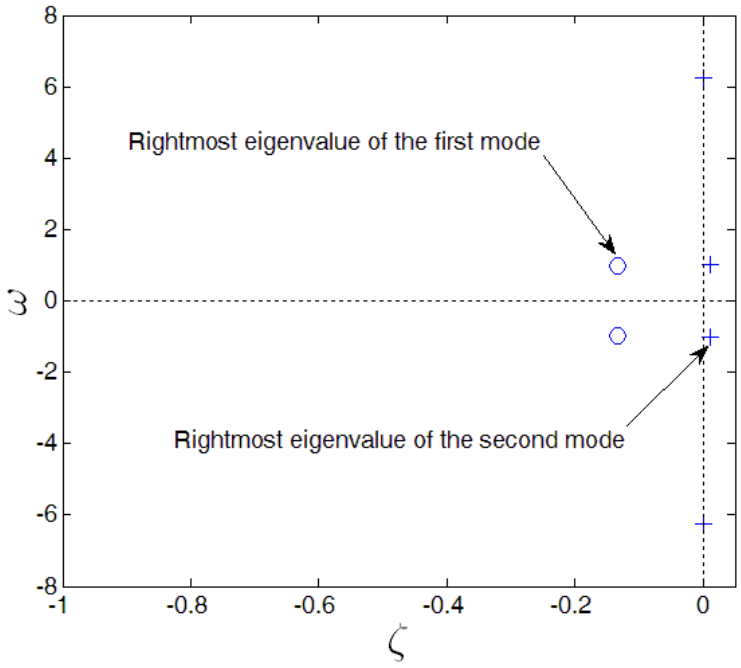

Figure 1.2: Rightmost eigenvalues of the first and second modes of a cantilevered beam for K=0.2 and τ=0.2.

nonlinear externally-excited systems [54, 55]. In particular, the nonlinear response of a delayed system to primary-resonance excitations has yet to be addressed comprehensively. Such studies were not necessary in the past due to the limited number of applications in which time delays and external excitations coexist in the operation of a dynamic system. Currently, and due to the emergence of micro and nanodevices as the next generation sensors and actuators, this type of analysis is becoming more imperative. For instance, to realize large dynamic responses, microdevices are usually excited at one of their resonant frequencies. Further, to enhance their dynamic characteristics, feedback control algorithms are being implemented to close the loop and provide real-time information about the states. However, due to their high natural frequencies, the presence of the infinitesimal measurement delays in the control loop can be of the order of magnitude of the response period, thereby channeling energy into or out of the system at incorrect time intervals producing instabilities

that render traditional controllers' performance ineffective [56].

To resolve these issues, there is a growing interest in the control and dynamic communities to utilize delayed-feedback controllers for vibration mitigation and control of microsystems. It has been shown that augmenting the system delay into a carefully and deliberately selected delay period (*shaded regions in Fig. 1.1*) is capable of producing substantial damping that can actually augment controllers' design [43]. Most recently, this idea was also adapted to control microcantilevers in dynamic force microscopy [57], to eliminate chaotic motions in taping-mode atomic force microscopy [58], for sensor sensitivity enhancement in nanomechanical cantilever sensors [59, 60], and to control the quality factor in dynamic atomic force microscopy [56]. Successful implementation of these controller on nonlinear delay systems, especially when the objective is to control an externally-excited system requires a deep analytical understanding of the primary resonance phenomenon in time-delayed systems. As such, it is the objective of this Dissertation to derive analytical techniques that permit investigation primary resonances of weakly-nonlinear delay systems. Further details are available in next Section.

1.4 Dissertation Contributions

The contributions of the conducted research can be summarized as follows:

- *Augmentation of low-pass filters into time-delay control algorithms to suppress vibrations in multi-degree-of-freedom and structural systems using a single-input single-output control approach:* The Dissertation introduces the concept of filter-augmented delayed-feedback algorithms and applies it to different structural systems both theoretically and experimentally. In specific, it explores the prospect of augmenting proper filters in the feedback loop to enhance the stability and robustness of delayed-feedback controllers; thereby

allowing them to simultaneously mitigate the response of different vibration modes using a single sensor and a single gain-delay actuator combination. The thesis goes into understanding the effect of filter dynamics (order and cut-off frequency) on the stability maps and damping contours of single-degree-of-freedom (SDOF) and multi-degree-of-freedom (MDOF) systems. Results from this work has been published in the 2009 *American Institute of Aeronautics and Astronautics (AIAA) Conference* [61].

- *Implementation of filter-augmented delay-feedback algorithms on structural systems that can be discretized into a system of linearly-uncoupled ODEs:* The concept is implemented to reduce the multi-modal oscillations of a linearly-uncoupled system of modal equations resulting from the discretization of a linear PDE and its associated boundary conditions. As an example, we considered two problems that involve reducing large-amplitude oscillations of an Euler-Bernoulli macro-cantilever beam, and a micro-cantilever sensor. We studied, both theoretically and experimentally, the influence of low-pass filters on the stability of the closed-loop system in the gain-delay space and on the robustness of the controller to parameter's uncertainties. (*Note that this Dissertation marks the first implementation of a delayed-feedback controller on the micro-scale*). Results form this work has been published in the *Journal of Smart Materials and Structures* [62].

- *Implementation of filter-augmented delayed-feedback algorithms on structural systems that can only be discretized into a set of linearly-coupled ODEs:* The third implementation considers a structure whose equations of motion are represented by two PDEs coupled through the boundary conditions, and hence, can only be discretized into an infinite set of linearly-coupled modal equations. The coupling complicates the stability analysis and makes it even more difficult to find a gain-delay combination that stabilizes all modes simultaneously.

As an example, we considered the problem of utilizing a delayed-position feedback controller to mitigate the linearly-coupled flexural-torsional oscillations of a cantilever beam with an asymmetric tip rigid body. This research is motivated by recent developments in the fields of turbomachinery, light-weight flexible space structures, and wind turbine blades. (*Note that this Dissertation marks the first implementation of a delayed-feedback controller on systems with linearly-coupled modes*). Results form this work have been submitted for publication in the *AIAA Journal*.

- *Adaptation of the "Partial Differential Equation Representation of the Delay Differential Equation" to obtain the damping contours of delayed-feedback controllers:* This approach is used for the first time to generate damping contours within the stability pockets of the closed-loop system. The adapted approach is proven to be beneficial for systems consisting of a large number of linearly-coupled modes as it significantly reduces computational cost. The resulting damping contours are used throughout this study to facilitate the choice of the optimal controller's gain-delay combinations.

- *Investigating primary resonances of weakly-nonlinear delay systems:* This Dissertation also provides a modified Method of Multiple Scales approach to characterize the nonlinear response of a delay system near primary resonance excitations. Unlike previous research efforts, the modified approach can describe the response behavior for large control gains and near multiple delay frequencies. It can also, for the first time, predict variations in the *softening-hardening* characteristics of the response due to variations in the controller's time delay. Results from this research have been published in the *Journal of Nonlinear Dynamics* [63].

1.5 Dissertation Outline

The rest of the Dissertation is organized as follows:

Chapter 2 presents an overview of linear time-invariant time-delay systems with constant delays. It provides a brief description, some classification, and the common methods used to analyze the stability of such systems. Chapter 3 investigates the role of low-pass filters in the stability and stabilization of MDOF systems using delayed-feedback algorithms. The Chapter starts by formulating the response of a general structural system as a series of a second-order oscillators subjected to an external excitation and a delayed control actuation force obtained by low-pass filtering a feedback signal. Subsequently, the Chapter provides a general stability analysis of the closed-loop system and investigates the influence of filter's cut-off frequency and order on the stability of the system in the gain-delay space for SDOF and MDOF systems. To validate the theoretical concepts, Chapter 4 discusses two different experimental implementations on systems with linearly-uncoupled modes. In the first demonstration, a filter-augmented delayed-position feedback algorithm is used to mitigate the vibrations of a macrocantilever beam. In the second demonstration, a filter-augmented delayed-velocity feedback algorithm is used to mitigate the vibrations of a microcantilever sensor.

Chapter 5 investigates the implementation of similar filter-augmented delayed-feedback control algorithms on a structural system that can only be discretized into a set of linearly-coupled modal equations. As an example, the Chapter considers the problem of suppressing the coupled flexural-torsional oscillations of a cantilever beam with an asymmetric tip rigid body using a single input (piezoelectric patch) and a single output (laser sensor). Chapter 6 presents a novel implementation of the Method of Multiple Scales to investigate primary resonances of weakly-nonlinear second-order delay systems with cubic nonlinearities. In contrast to previous studies where the analysis is confined to the assumption of linear delay terms with small

gains, the Chapter proposes a modified approach which alleviates that assumption and permits treating a problem with arbitrarily large gains. Chapter 6 also provides a validation of the modified procedure by comparing its results to solutions obtained via a Harmonic Balance approach. Several examples are discussed demonstrating the ability of the proposed methodology to predict the amplitude, softening-hardening characteristics, and stability of the resulting steady-state responses. Finally, Chapter 7 provides our conclusions and recommendations for future work.

Chapter 2

Stability of Time-Delay Systems

This Chapter provides a brief overview of linear time-invariant time-delay systems with constant delays. It provides a brief description, some classification, and the common methods used to analyze the stability of such systems. Some of these methods will be utilized in later chapters of this proposal. As such, a general understanding of some of these concepts is necessary to grasp the research presented later in the manuscript.

2.1 Classification of Linear Time-Invariant Delay Systems

Typically, time-delay systems are divided into two main groups: *retarded* and *neutral*. A time-delay system is said to be retarded when it does not contain delays in its highest-order derivatives. On the other hand, a system in which there is delay associated with the highest-order derivative is called neutral. The stability of both systems is determined by the location of the infinite number of eigenvalues associated with the characteristic equation in the complex plane. The system is said to

be asymptotically stable when all eigenvalues are located in the left hand-side of the complex plane and is unstable when at least one eigenvalue is located in the right-hand side of the complex plane. Nevertheless, there is a main peculiarity between retarded and neutral delay systems in terms of the distribution of the characteristic eigenvalues in the complex plane. In retarded delay systems, the number of eigenvalues crossing over to the right-half plane when a certain parameter changes is always finite. Therefore, it is possible to keep track of the number of right-half plane eigenvalues. However, this does not apply to a neutral delay system. To overcome this obstacle, the stability criterion is usually made stricter in the case of neutral systems by forcing the eigenvalues to strictly lie to the left of a specific line in the left-hand side of the complex plane [21, 2, 64].

Based on the type of delay present in the equations, time-delay systems can also be classified as *commensurate* or *incommensurate*. If the time delays are integer multiples of a common positive number, τ, then the delay system is called commensurate. Otherwise, it is called incommensurate. Because of the nature of the resulting quasi-polynomial associated with commensurate delay systems, their stability analysis tends to be much simpler [65, 66].

2.2 Common Methods for the Stability Analysis of Linear Time-invariant Delay Systems:

This Section describes some of the numerical techniques that are used to approximate or solve the characteristic quasi-polynomial associated with time-delay systems. To that end, we start by considering the following general linear retarded system

$$\dot{x}(t) = Ax(t) + A_d x(t-\tau); \quad t \geq 0, \tag{2.1}$$

where $x \in \mathcal{R}^n$ is the state vector, A is the state matrix, and A_d is the delay coefficient matrix. Both A and $A_d \in \mathcal{C}^{m \times m}$. To solve Equation (2.1), we define the initial function

$$x(t) = \phi(t); \quad -\tau \leq t \leq 0, \tag{2.2}$$

where $\phi(t) \in \mathcal{C}([-\tau, 0], \mathcal{C}^m)$. We then apply Laplace transform (denoted by $\mathcal{L}[*]$) to transform Equation (2.1) into the frequency domain. This yields

$$sX(s) - \phi(0) = AX(s) + A_d \left(e^{\tau s} X(s) + \int_0^{\tau} e^{-s\tau} \phi(t-\tau) dt \right); \; X(s) = \mathcal{L}(x(t)). \tag{2.3}$$

Rearranging and simplifying Equation (2.3), we have

$$X(s) = \left(sI - A - A_d e^{-\tau s} \right)^{-1} \left(\phi(0) + A_d \int_0^{\tau} e^{-s\tau} \phi(t-\tau) dt \right). \tag{2.4}$$

The poles of the transfer function given by Equations (2.4) represent the eigenvalues of the characteristic quasi-polynomial. These poles can be obtained by solving

$$Det \left[sI - A - A_d e^{-\tau s} \right] = 0. \tag{2.5}$$

In general, Equation (2.5) can be solved numerically for the infinitely many characteristic roots [65, 21, 66]. However, such solutions can be cumbersome and time consuming especially for systems with large dimensions. To circumvent this problem, many techniques have been proposed in the open literature to approximate the roots of the characteristic polynomial. Of special interest is the search for the dominant pole (closest eigenvalue to the imaginary axis) which is necessary to characterize the stability of the system. Next, we provide an overview of some of most common and important techniques available.

2.2.1 The Padé approximation

The Padé approximation provides a finite-dimensional rational approximation of the exponential term in the characteristic equation [67]. Specifically, the approximation expands the term $(e^{-s\tau})$ as

$$e^{-s\tau} \approx \frac{N_n(\tau s)}{D_n(\tau s)}, \tag{2.6}$$

where

$$N_n(-\tau s) = \sum_{j=0}^{n} \frac{(2n-j)!}{j!(n-j)!}(-\tau s)^j \quad and \quad D_n(-\tau s) = \sum_{j=0}^{n} \frac{(2n-j)!}{j!(n-j)!}(\tau s)^j, \tag{2.7}$$

where n is the approximation order. The method can be very accurate for some small delays but diverges as the time delay is increased requiring higher-order approximation in order to obtain accurate results. Furthermore, in some cases, the technique yields *spurious* roots. In other words, roots that are not even a solution of the original quasi-polynomial. Such roots can be problematic because they might affect the stability results. Additionally, the step-response of this approximation exhibits a jump at $t = 0$ due to the equal numerator and denominator degree. In other words, an output at time t=0 appears in the response, where it is supposed to show a delay output at $t = \tau$. Having said that, Padé approximation has many advantageous properties in the frequency domain and, when carefully implemented, can be used for model-order reduction [68].

2.2.2 Lambert function approach

Based on the definition of Lambert and Euler in 1758, a Lambert W function , $W(s)$, satisfies the equation

$$W(s)e^{W(s)} = s. \tag{2.8}$$

The Lambert W function has an infinite number of branches and the zeroth branch is called the principle branch. In 2000, Asl et al. [69] showed that the principle branch of the Lambert W function can be related to the rightmost pole (dominant eigenvalue) of the characteristic quasi-polynomial of a time-delay system. Followed by this work, several researchers [70, 71, 72, 73, 74, 75] explored different aspects of employing the Lambert W function in the stability evaluation of time delay systems.

To explain this approach, we start with the characteristic equation

$$sI + A + A_d e^{-s\tau} = 0, \tag{2.9}$$

and multiply both sides by $\tau e^{A\tau}$, then rearrange, to obtain

$$\tau(sI - A)e^{\tau(sI-A)} = -A_d \tau e^{-A\tau}. \tag{2.10}$$

The matrices A and A_d may not necessarily commute and neither do A or sI. However, it can be shown that when A and A_d commute, then sI and A_d also commute. Thus, in general

$$\tau(sI - A)e^{\tau sI}e^{-\tau A} \neq \tau(sI - A)e^{\tau(sI-A)}. \tag{2.11}$$

As a result, to write the solution in terms of the matrix Lambert function, we introduce an unknown matrix Q that satisfies,

$$\tau(sI - A)e^{\tau(sI-A)} = -A_d \tau Q. \tag{2.12}$$

Using Equation (2.8), one can write

$$W(-A_d \tau Q)e^{-W(A_d \tau Q)} = -A_d \tau Q. \tag{2.13}$$

Now, comparing Equation (2.12) to Equation (2.13), it can be realized that

$$\tau(sI - A) = W(-A_d \tau Q). \tag{2.14}$$

According to Lambert, Equation (2.14) have infinite branches of solution. The solution associated with k^{th} branch can be written as

$$s_k = \frac{1}{\tau} W_k(-A_d \tau Q) + A, \tag{2.15}$$

where s_k is the k^{th} eigenvalue. Note that s_0 represents the dominant pole. Substituting Equation (2.15) into Equation (2.10) to solve for the Q matrix, we obtain

$$W_k(A_d \tau Q_k) e^{(W_k(A_d \tau Q_k) + A\tau)} = A_d \tau. \tag{2.16}$$

Equations (2.15) and (2.16) represent a system of two nonlinearly-coupled algebraic equations, with two unknown parameters (Q_k, s_k) of the k^{th} branch. The zeroth branch of Lambert function W_0 corresponds to the rightmost pole [75]. Some mathematical modeling packages like Maple, Matlab, and Mathematica have predefined Lambert function installed and ready to use. The numerical command "fsolve" is used to solve for the stability exponents of the time-delay systems by defining an initial condition on Q_0. However, for higher-dimensional problems, the solution for Q_0 depends entirely on the initial guesses used, and hence, it is a very tedious and cumbersome task to find the proper initial condition.

2.2.3 Discretization of the PDE representation of the DDE

In the year 2000, Bellen and Maset [76] presented an approach for the numerical solution of DDE's in the form of an abstract Cauchy problem. The core of the technique is to transform the DDE into a PDE then descritizing it into a set of linear

Ordinary Differential Equations (ODEs) using the method of lines. The eigenvalues resulting from the solution of the system of ODEs represent the eigenvalues of the characteristic quasi-polynomial. Obviously, the number of eigenvalues resulting from this approach is finite and will increase as the number of ODEs resulting from the discretization is increased. Furthermore, the accuracy of the resulting eigenvalues increases with the number of ODEs resulting from the discretization. The important characteristic of this scheme is that the resulting eigenvalues can always be ordered in terms of their closeness to the imaginary axis which allows for identifying the dominant eigenvalue necessary for the stability analysis. Various researchers have demonstrated the asymptotic convergence of the proposed approach [77, 78].

To better demonstrate how to implement this approach to a DDE, we consider Equation (2.1) with the initial function as defined in Equation (2.2). If one considers the delay as another variable, say θ, defined over the interval $[-\tau, 0]$, then it becomes possible to introduce a function of two different variables $u(t, \theta)$ to describe the dynamics of the DDE. The trick here is to find an equivalent PDE whose characteristic equation resembles that of the DDE. To that end, let us consider the following first-order Hyperbolic PDE:

$$\frac{\partial u}{\partial t}(t, \theta) = \frac{\partial u}{\partial \theta}(t, \theta), \quad t \geq 0, \quad -\tau \leq \theta \leq 0, \tag{2.17}$$

with the boundary condition

$$\frac{\partial u}{\partial \theta}(t, 0) = Au(t, 0) + A_d u(t, -\tau), \quad t \geq 0, \tag{2.18}$$

and the initial condition

$$u(0, \theta) = \phi(\theta), \quad \theta \in [-\tau, 0] \tag{2.19}$$

A solution of Equation (2.17) with the associated boundary and initial conditions

can be obtained using the Laplace transform. Taking the Laplace transform of both sides and substituting the initial condition, one obtains

$$\frac{dU}{d\theta}(s,\theta) - sU(s,\theta) = \phi(\theta). \tag{2.20}$$

A solution of Equation(2.20) can be obtained by integrating and substituting the boundary conditions. This yields the following eigenvalue problem for s

$$Det[sI - A - A_d e^{-\tau s}] = 0, \tag{2.21}$$

which is identical to Equation (2.5). Hence, the two problems are equivalent. Now, that the problem has been transformed into a set of PDEs, one can use a discretization algorithm to solve it. Here, we use the method of lines (which is a form of the finite difference approach) to discretize the dependence on θ in Equation (2.17). To that end, we introduce the mesh Ω_N given by

$$\begin{cases} \Omega_N = \{\theta_n | n = 0, 1, ..., N\}), \\ \theta_n = -nh, \quad n = 0, 1, ..., N, \\ h = \frac{\tau}{N}, \end{cases} \tag{2.22}$$

on the interval $[-\tau, 0]$. Further, we substitute the partial derivative by a forward first-order approximation as

$$\frac{\partial u}{\partial \theta} \approx \frac{1}{h}\left(u(t, \theta + h) - u(t, \theta)\right). \tag{2.23}$$

This yields the following linear system of $m(N+1) \times m(N+1)$ ODEs

$$\begin{cases} \frac{d}{dt}u_N(t) = \mathcal{A}_N u_N(t), \quad t \geq 0, \\ u_N(0) = \phi_N \end{cases} \tag{2.24}$$

where

$$\mathcal{A}_N = \begin{bmatrix} B_N & \otimes & I \\ A & 0 \dots & A_d \end{bmatrix} \in \mathcal{C}^{(1+N)m \times (1+N)m}, \tag{2.25}$$

where I is $m \times m$ identity matrix, $\phi_N = (\phi(-\tau), \dots, \phi(-h), \phi(0))$, and

$$B_N = \frac{1}{h} \begin{bmatrix} -1 & 1 & & & & & \\ & \ddots & \ddots & & & & \\ & & \ddots & \ddots & & & \\ & & & \ddots & \ddots & & \\ & & & & -1 & 1 & \\ & & & & & -1 & 1 \end{bmatrix} \in \mathcal{R}^{N \times (1+N)} \tag{2.26}$$

The eigenvalues of the matrix $\mathcal{A}_N$ represent the first N eigenvalues of the quasi-polynomial. It is worth noting that the accuracy of the resulting solution increases as N increases and as the delay decreases. However, the method has been shown to have very fast convergence with small values of N especially when it comes to approximating the dominant root of the characteristic quasi-polynomial [79, 80].

Chapter 3

Filter-Augmented Delayed-Feedback Control Algorithm

This Chapter explores augmenting proper filters in the feedback loop to enhance the stability and robustness of delayed-feedback controllers; thereby allowing them to simultaneously mitigate the response of different vibration modes using a single sensor and a single gain-delay actuator combination. However, it is known that filters introduce their own dynamics into the system and can also produce additional delays. As such, it is the purpose of this Chapter to investigate the role that low-pass filters can play in the stability and stabilization of multi-degree of freedom systems using delayed-feedback algorithms. We start by formulating the response of a general structural system as a series of a second-order oscillators subjected to an external excitation and a delayed control actuation force obtained by low-pass filtering a feedback signal. We then carry out a general stability analysis on the closed-loop system and study the effect of the filter's cut-off frequency and order on the stability of the system in the gain-delay space for single- and multi-degree of freedom systems.

3.1 Problem Formulation

We consider a general MDOF linear system representing a reduced-order model of a structural system. The governing dynamics is represented by a series of linear second-order oscillators as follows:

$$\begin{aligned} \ddot{x}_i(t^*) + 2\zeta_i\omega_i\dot{x}_i(t^*) + \omega_i^2 x_i(t^*) &= a_i^* F(t^*) + d_i^*\delta(t^*), \\ x_i(0) = x_{i0}, \dot{x}_i(0) &= v_{i0} \quad i = 1, 2, ..., n, \end{aligned} \tag{3.1}$$

where x_i are dimensionless modal terms, t^* denotes time, ω_i are modal frequencies, ζ_i are modal damping ratios, $F(t^*)$ is the actuation control signal, $\delta(t^*)$ is an external disturbance, and a_i^* and d_i^* are constants representing, respectively, the relative projection of the control signal and external disturbance onto the different modes. The goal here is to choose a control signal $F(t^*)$ which can augment system delays while simultaneously mitigating system vibrations resulting from the external disturbance δ or the initial conditions. For this purpose, it is assumed that a feedback signal can be obtained using a sensor that measures a linear combination of the modal terms as

$$y_f(t^*) = \sum_{i=1}^{n} c_i x_i, \tag{3.2}$$

where c_i are constants.

In common practice, the feedback signal $y_f(t^*)$ is usually passed through a low-pass filter to remove noise, signal interferences, and other higher-order dynamic distortion. For that purpose, a general k^{th} order Butterworth low-pass filter (BLPF) is utilized, see Fig. 3.1. The Butterworth filter is usually used for its simplicity and ability to have a flat frequency response up to the desired cut-off frequency after which the response dies rapidly with a roll-off slope depending on the filter's order. The filter output can be related to the sensor's signal through the following filter

dynamics:

$$\frac{b_k}{\omega_{cf}^k} y_1^{(k)} + \frac{b_{k-1}}{\omega_{cf}^{k-1}} y_1^{(k-1)} + ... + \frac{b_1}{\omega_{cf}} \dot{y_1} + b_0 y_1 = y_f(t^*), \tag{3.3}$$

where y_1 is the filter output, ω_{cf} is the filter's cut-off frequency and b_k are the coefficients of the polynomials obtained by evaluating either one of the following Equations [81, 82]:

$$b_k(s) = \prod_{j=1}^{\frac{k}{2}} \left\{ \left(\frac{s}{\omega_{cf}} \right)^2 - 2 \left(\frac{s}{\omega_{cf}} \right) \cos \left(\frac{2j+k-1}{2k} \pi \right) + 1 \right\}, \ for \quad k \quad even \tag{3.4a}$$

$$b_k(s) = \left(\left(\frac{s}{\omega_{cf}} \right) + 1 \right) \prod_{j=1}^{\frac{k-1}{2}} \left\{ \left(\frac{s}{\omega_{cf}} \right)^2 - 2 \left(\frac{s}{\omega_{cf}} \right) \cos \left(\frac{2j+k-1}{2k} \pi \right) + 1 \right\}, \tag{3.4b}$$

$for \quad k \quad odd$

where k is the order of the filter.

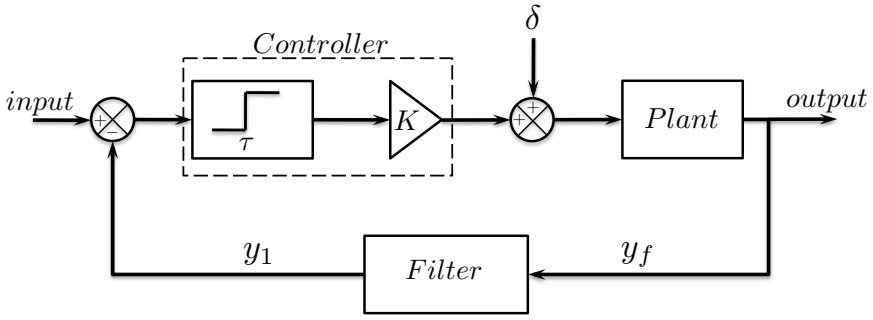

Figure 3.1: Block diagram of a delayed-position feedback control algorithm.

The control signal is chosen as the filtered sensor's signal amplified by a proper gain, K^*, and delayed by a deliberately-introduced delay period τ^* such that

$$F(t^*) = K^* y_1(t^* - \tau^*) \tag{3.5}$$

Using Equation (3.5), the closed-loop system dynamics can be written as

$$\ddot{x}_i(t^*) + 2\zeta_i\omega_i\dot{x}_i(t^*) + \omega_i^2 x_i(t^*) = k_i^* y_1(t^* - \tau^*) + d_i^*\delta(t^*) \tag{3.6a}$$

$$\frac{b_k}{\omega_{cf}^k} y_1^{(k)} + \frac{b_{k-1}}{\omega_{cf}^{k-1}} y_1^{(k-1)} + ... + \frac{b_1}{\omega_{cf}}\dot{y_1} + b_0 y_1 = \sum_{i=1}^{n} c_i x_i \tag{3.6b}$$

where $k_i^* = a_i^* K^*$ and $i = 1, 2, 3, ..., n$.

To non-dimensionalize Equations (3.6a) and (3.6b), we introduce the non-dimensional time $t = t^*\omega_1$, delay period $\tau = \tau^*\omega_1$, modal damping $\mu_i = \zeta_i\omega_i/\omega_1$, and the frequency ratio $\epsilon = \omega_1/\omega_{cf}$. With that, Equations (3.6a) and (3.6b) become

$$\ddot{x}_i + 2\mu_i\dot{x}_i + \frac{\omega_i^2}{\omega_1^2} x_i = k_i y_1(t - \tau) + d_i\delta \tag{3.7a}$$

$$b_k\epsilon^k y_1^{(k)} + b_{k-1}\epsilon^{k-1} y_1^{(k-1)} + ... + b_1\epsilon\dot{y_1} + b_0 y_1 = \sum_{i=1}^{n} c_i x_i \tag{3.7b}$$

where $k_i = \frac{k_i^*}{\omega_1^2}$ and $d_i = \frac{d_i^*}{\omega_1^2}$.

3.2 Stability Analysis

As mentioned previously, delayed-feedback control algorithms, similar to Equation (3.5), have been widely utilized as effective means for vibration mitigation and oscillation reduction on various systems [33, 34, 35, 36, 37, 38, 39, 40]. Although low-pass filters, similar to the one adopted here, are usually used to augment controllers' design in practice; their effect on the stability margins of delayed-feedback algorithms has never been investigated. To elucidate the role of augmenting such filter in the stability of delayed-feedback algorithms, we obtain the gain, K, and delay period, τ, that render the closed-loop system of Equations (3.7a) and (3.7b) stable. To that

end, we assume that these equations admit a solution of the form:

$$\begin{bmatrix} x_i \\ y_1 \end{bmatrix} = \begin{bmatrix} X_i \\ Y \end{bmatrix} e^{\lambda t}, \qquad i = 1, 2, ..., n, \tag{3.8}$$

where $[X_i\ Y]$ is the eigenvector associated with the system eigenvalue, λ. Substituting Equation (3.8) into Equations (3.7a) and (3.7b) yields in matrix form

$$A(\lambda) \begin{bmatrix} X_i \\ Y \end{bmatrix} = 0, \tag{3.9}$$

where

$$A(\lambda) = \begin{bmatrix} \lambda^2 + 2\mu_1\lambda + 1 & 0 & \cdots & 0 & k_1 e^{-\lambda\tau} \\ 0 & \lambda^2 + 2\mu_2\lambda + \left(\frac{\omega_2}{\omega_1}\right)^2 & \cdots & 0 & k_2 e^{-\lambda\tau} \\ \vdots & \vdots & \vdots & \vdots & \vdots \\ 0 & 0 & \cdots & \lambda^2 + 2\mu_n\lambda + \left(\frac{\omega_n}{\omega_1}\right)^2 & k_n e^{-\lambda\tau} \\ -c_1 & -c_2 & \cdots & -c_n & \eta(\lambda) \end{bmatrix} \tag{3.10}$$

and $\eta(\lambda) = \left(b_k \epsilon^k \lambda^k + b_{k-1}\epsilon^{k-1}\lambda^{k-1} + ... + b_1\epsilon\lambda + b_0\right)$

To obtain the eigenvalues, λ, we set the determinant of the coefficient matrix $A(\lambda)$ to zero. The result is a transcendental characteristic equation in λ. This equation has infinite number of eigenvalues. For an asymptotically stable closed-loop response, all the λ_i's must be located in the left-hand side of the complex plane.

3.2.1 Filter's influence on the stability of a Single-Degree-of-Freedom (SDOF) system

We begin by trying to understand how the filter dynamics affect the stability of a SDOF system in the presence of a delayed-position feedback controller. We inves-

tigate the effect of the filter's cut-off frequency and order on the stability pockets. In the SDOF case, the stability is governed by the sign of the infinite roots of the following quasipolynomial:

$$(\lambda^2 + 2\mu_1\lambda + 1)\eta(\lambda) + c_1 k_1 e^{-\lambda\tau} = 0. \tag{3.11}$$

To find the stability boundaries, we set $\lambda = \pm i\omega$ and obtain

$$(-\omega^2 + 2i\mu_1\omega + 1)\eta(i\omega) + c_1 k_1 e^{-i\omega\tau} = 0. \tag{3.12}$$

In the case we have a first-order filter ($b_n = 0, n > 1$), it is easy to parameterize the space of $K - \tau$ into stable and unstable regions using the D-decomposition approach [83, 84]. To that end, we separate the real and imaginary parts of Equation (3.12) and obtain the following equations:

$$\begin{aligned} b_0(1-\omega^2) - 2b_1\epsilon\mu_1\omega^2 + c_1 k_1 \cos[\tau\omega] = 0; \\ -2b_0\mu_1\omega + b_1\epsilon(\omega^2 - 1) + c_1 k_1 \sin[\tau\omega] = 0. \end{aligned} \tag{3.13}$$

The previous equations can be solved for the critical gain and delay at the stability boundary as

$$\begin{aligned} k_1 &= \pm\frac{1}{c_1}\sqrt{(b_0^2 + b_1^2\epsilon^2\omega^2)(1 + (4\mu_1^2 - 2)\omega^2 + \omega^4)}, \\ \tau &= \frac{1}{\omega}\left\{ \arctan\left(\frac{\omega(-2\mu_1 b_0 + b_1\epsilon(\omega^2 - 1))}{(b_0 + 2b_1\epsilon\mu_1)\omega^2 - b_0}\right) + n\pi \right\}, n = 1, 2, \ldots, \infty \end{aligned} \tag{3.14}$$

Equations (3.14) represents the value of the gain and delay at the stability boundary. These equations can be used to generate a stability map of the system by varying ω and plotting the corresponding values of k_1 and τ in the gain delay space. The stability of a given pocket is assessed by choosing a gain-delay combination within each pocket, solving Equation (3.11) for the eigenvalues λ and assuring that the dominant roots have a negative real part. With that, we construct the stability

Table 3.1: Numerical values used for simulations.

First modal frequency, ω_1 [rad/s]	1
First modal damping ratio, μ_1	0.005
First modal force projection constant, a_1	1
First modal feedback projection gain, c_1	1
Second modal frequency, ω_2 [rad/s]	7
Second modal damping ratio, μ_2	0.005
Second modal force projection constant, a_2	0.5
Second modal feedback projection gain, c_2	1
Third modal frequency, ω_3 [rad/s]	12
Third modal damping ratio, μ_3	0.005
Third modal force projection constant, a_3	0.25
Third modal feedback projection gain, c_3	1

maps shown in Fig. 3.2(a).

The influence of the filter's cutoff frequency ω_{cf} with respect to ω_1 (i.e. $\epsilon = \omega_1/\omega_{cf}$) on the stability pockets is shown in Figs. 3.2(a)-3.2(d) for the numerical values listed in Table 3.1. We choose a first-order BLPF and plot the stability boundaries for four values of ϵ, namely, $\epsilon = 0, 0.1, 0.5, 0.667$, and 1. We observe that, as ϵ increases, i.e., ω_{cf} is chosen closer to ω_1, the stability boundaries shift to the left along the delay axis. This is also evident in Equations (3.14) which demonstrate that, for a given ω, the value of the critical τ is always smaller when compared to the unfiltered case ($\epsilon \to 0, b_0 = 1$). This causes the first and largest stability pocket to shrink which, in turn, can reduce the robustness of the controller to variations in the system's and control design parameters. The shift can be attributed to the additional delay introduced by the filter which depends on the input signal frequency. In addition, we observe that, for very small values of ϵ, the effect of the cut-off frequency is small and can be neglected. Further, it is observed that the cut-off frequency can increase the size of the second and third stability pockets because, as seen in Equation (3.14), increasing ϵ will increase the value of k_1 which shifts the curves upwards along the gain axis.

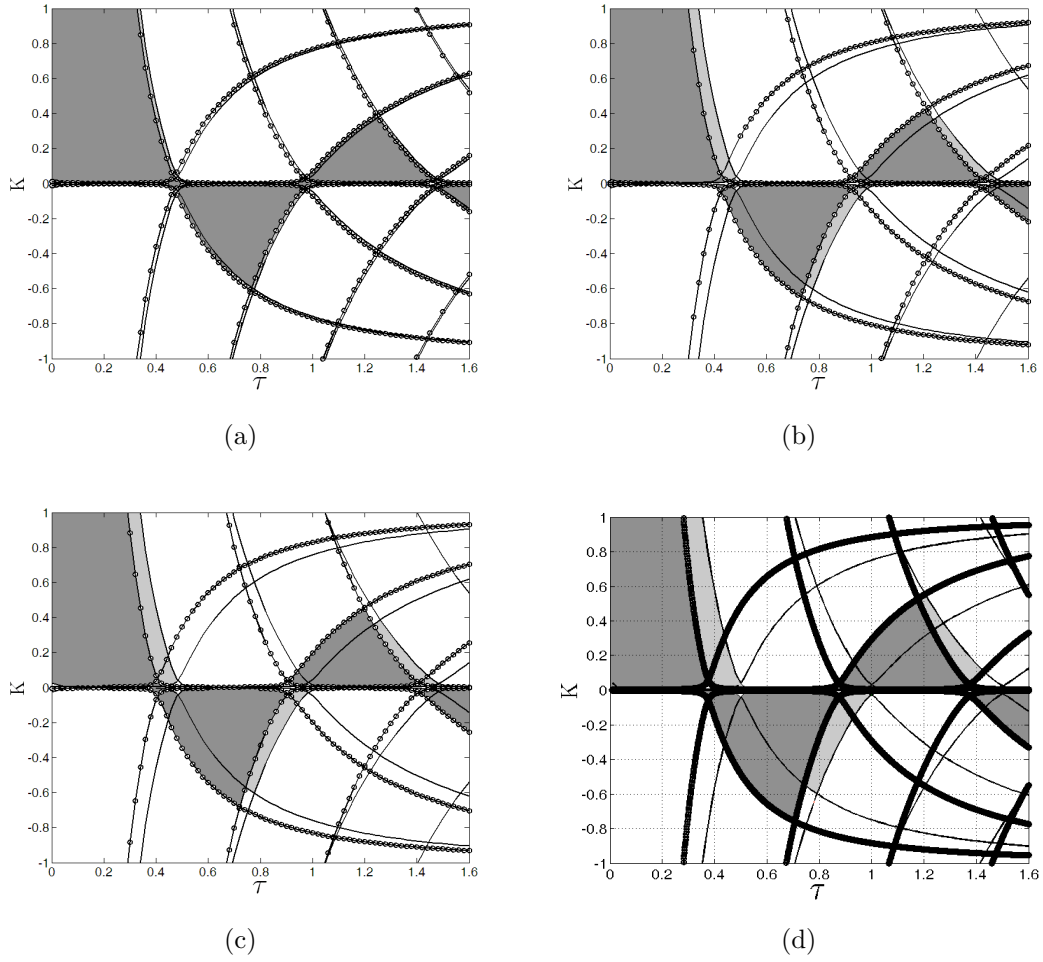

Figure 3.2: Theoretical stability pockets for a SDOF system. Results compare a) no filter to first-order filter with $\epsilon = 0.1$, b) no filter to first-order filter with $\epsilon = 0.5$, c) no filter to first-order filter with $\epsilon = 0.667$, and d) no filter to first-order filter with $\epsilon = 1$. Circles represent stability boundaries in the presence of a low-pass filter and shaded regions represent stable gain-delay combinations.

The influence of the filter's order on the stability pockets is shown in Figs. 3.3(a)-3.3(c). Similar to the effect of the cut-off frequency, increasing the filter's order leads to a shift in the stability pockets towards the left along the delay axis. This again has a negative influence on the stability margins, and, hence, the robustness of the controller. It also influences the size of the pockets. For instance, the first-order BLPF slightly enlarges the second and third pockets. As the order of the filter

increases, the size of these pockets starts to shrink again. As such, in general, it can be concluded that, augmenting a low-pass filter to a delayed-position control algorithm applied to a SDOF system has a negative influence on the stability margins in the gain-delay space.

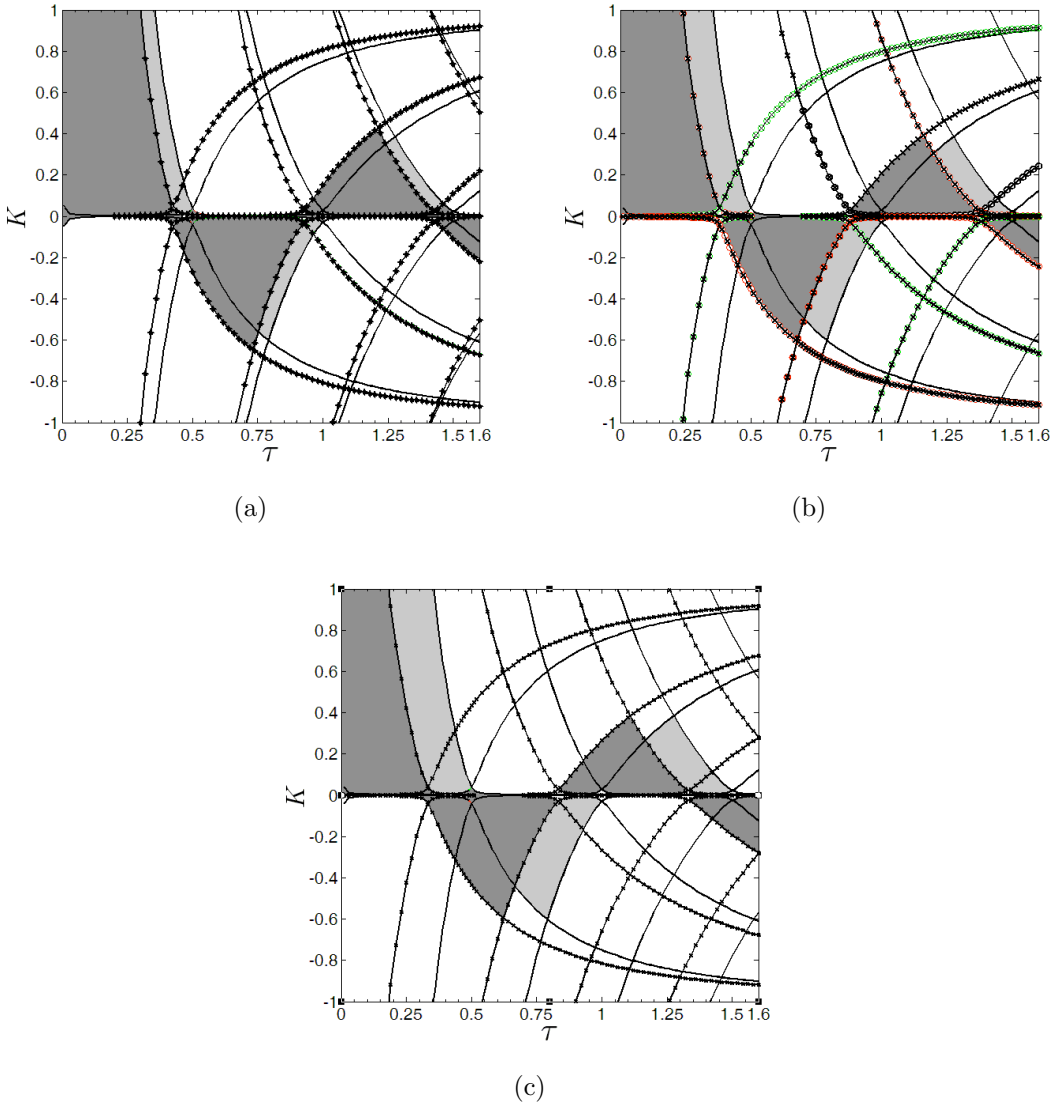

Figure 3.3: Theoretical stability pockets for a SDOF with $\epsilon = 1/3$. Results are obtained when a) no filter is used versus first-order BLPF, b) no filter is used versus second-order BLPF, and c) no filter is used versus third-order BLPF. Circles represent stability boundaries in the presence of a low-pass filter and shaded regions represent stable gain-delay combinations.

3.2.2 Filter's influence on the stability of a 2-DOF system

Next, we take into account an additional vibration mode such that ω_2 is arbitrarily chosen as seven times ω_1. We investigate the influence of the second-mode dynamics on the stability in the gain-delay space for various orders of the BLPF. Figures 3.4(a)-3.4(d) depict the stability pockets corresponding to the two-mode response for different orders of the BLPF and a fixed cut-off frequency. The cut-off frequency is chosen such that it is three times the first modal frequency. It can be seen that, as a result of the second-mode dynamics, within each stability pocket associated with the first mode, seven new stability pockets appear. Consequently, the shaded areas which provide gain-delay combinations that yield a stable response shrink significantly affecting the overall stability margins of the controller. A closer look at the resulting stable pockets reveals that the new stability diagram can be constructed by simply mapping the stability pockets of the second mode (which can be obtained by scaling the delay axis with respect to the second-mode frequency) on top of the stability pockets of the first mode with the new stable pockets being those representing only the intersection of the stable pockets of both modes. With this finding, adding more modes to the dynamics is expected to cause the stability pockets to shrink even further. Figure 3.5 shows clearly that by considering a third mode in the system, the stable pockets shrink even further due to the additional dynamics.

Figures 3.4(a)-3.4(d) reveal that, increasing the BLPF order, yields two distinct shifts in the stability diagram. The first moves the whole stability diagram to the

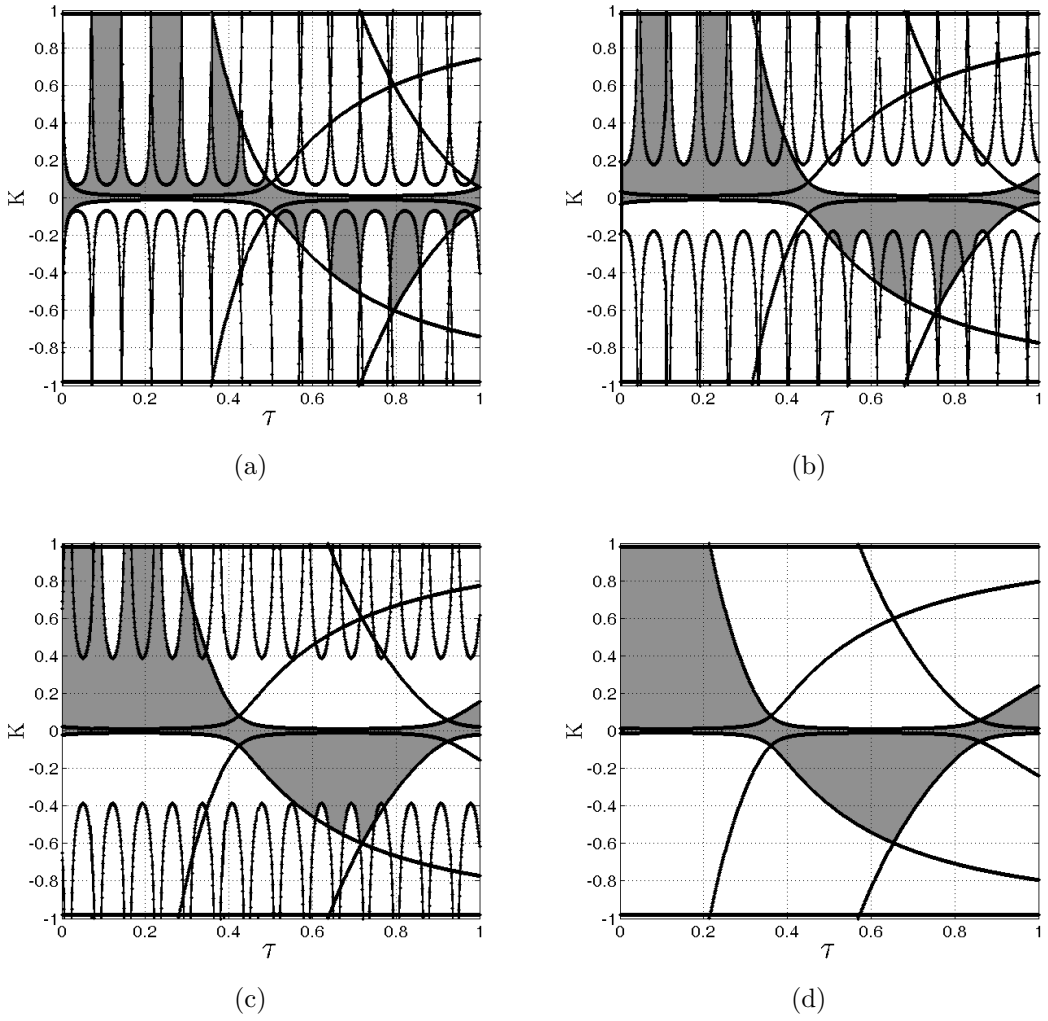

Figure 3.4: Theoretical stability pockets for a 2-DOF system augmented with a BLPF ($\epsilon = 1/3$). Results are obtained when a) no filter is used, b) first-order filter, c) second-order filter, and d) fourth-order filter.

left along the delay axis and corresponds to the delay in the filter dynamics which increases with the order of the filter. Again, this shift causes the first and largest stable pocket to shrink. The second shift is associated with the stable boundaries corresponding to the second-mode dynamics. It is observed that by increasing the order of the filter, those boundaries move up along the gain axis until their effect is totally rejected from the stability diagram when a fourth-order filter is used, as

shown in Fig. 3.4(d). It is clearly seen from these results that, by augmenting a proper filter, the influence of the higher modes' on the stability map can be completely avoided. This increases the stability margins of the controller significantly. For instance, if we were to use Fig. 3.4(a) to pick a gain-delay combination that stabilizes the first two modes simultaneously; any small uncertainties or variations in the control or design parameters can destabilize the response. This, however, can be avoided if we were to augment a fourth-order filter with the controller. It is also worth noting that, even when the cut-off frequency is chosen well below the second modal frequency, the effect of the second mode can still be seen for lower-order filters. This is attributed to the small roll-off slope. In the case presented here, a fourth-order filter is required to completely reject the effect of the second mode from the stability diagram.

Similar conclusions can be extended to 3-DOF or even a general MDOF system. Specifically, if a high-order filter which can reject the influence of the second vibration mode completely from the stability diagram is implemented, then one would correctly expect that it will also prevent the higher vibration modes from influencing the stability of the closed-loop system. However, in the case that a low-order filter with a large cut-off frequency is used, then higher modes can have a detrimental influence on the stability of the controller.

3.2.3 Damping characteristics

For vibration mitigation purposes, stability alone is not a sufficient measure of the controller's performance. The effective damping is actually an essential measure for the controller's ability to mitigate vibrations and reject external disturbances. Hence, within each stable pocket, we pick a given gain, vary the delay and plot the real part of the dominant root (the root closest to the imaginary axis) for three different filters. The dominant root governs the dynamic response and represents

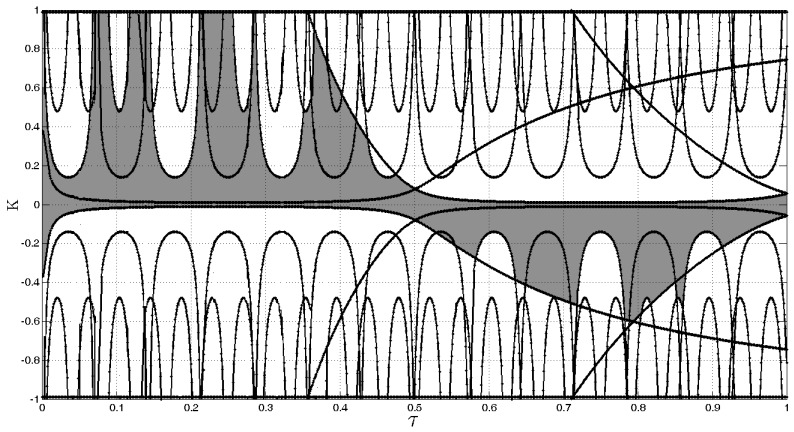

Figure 3.5: Theoretical stability pockets for a 3-DOF system without filtering.

a measure of the damping characteristics. Figure 3.6 shows variation of the real part of the dominant root with the delay for a gain, $K = 0.4$. Results illustrate that, for the three filters, the magnitude of the real part of the dominant root varies harmonically with the delay exhibiting a series of minima and maxima within a given stability pocket. Hence, for some delays, the damping can be increased and for some others it can actually be decreased. What is even more interesting is that these variations become less prominent as the filter's order is increased for the chosen gain. This implies that higher-order filters that can reject higher modes from the feedback can actually reduce the maximum effective damping in the system by shifting the dominant roots closer to the imaginary axis.

This can also be illustrated by simulating the response of the first two modes to some initial conditions as depicted in Figs. 3.7. Three delay values were chosen from Fig. 3.6 such that, for every BLPF, the chosen delay will produce the maximum damping. It is clear that, when compared to the free response, the first-order BLPF yields the fastest settling time and best performance characteristics. The reason being that the dominant pole of the closed-loop system produces an effective damping ratio of about $\zeta = -0.015$ which is approximately one and a half times

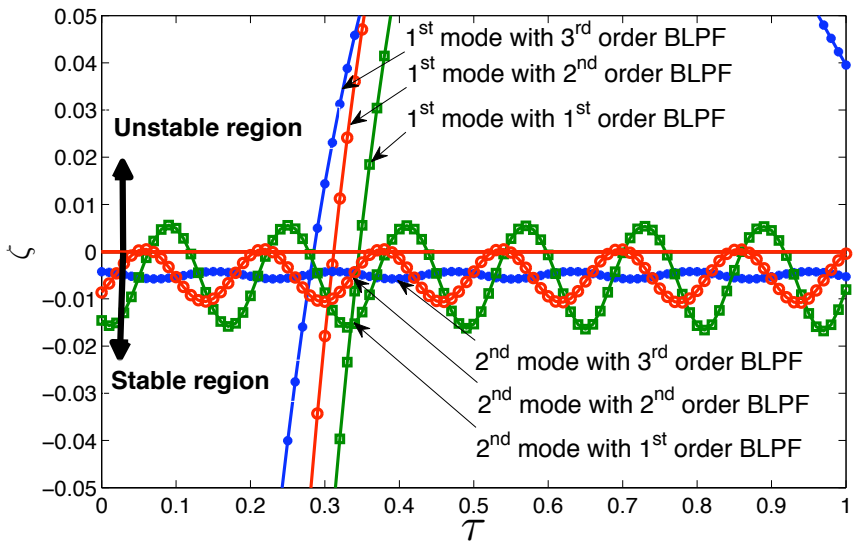

Figure 3.6: Theoretical damping (real part of the dominant eigenvalues) with $K = 0.4$. Results are obtained for a first-order BLPF (squares), second-order BLPF (circles), and third-order BLPF (stars).

that resulting from the second-order filter and three times that resulting from a third-order filter. It should be noted, however, that in the case of the first-order BLPF, small variations in the delay around the chosen design value due to parameter uncertainties or the slightest additional and unaccounted for delays can destabilize the system. Such issue is avoided when using the third-order BLPF filter.

While Fig. 3.6 reveals interesting conclusions about the effect of the filter order on the damping characteristics of the controller, it does not provide sufficient information about the damping contours within the stable pockets. Part of the proposed future work, see Chapter 5, deals with implementing a new method to obtain these essential damping contours.

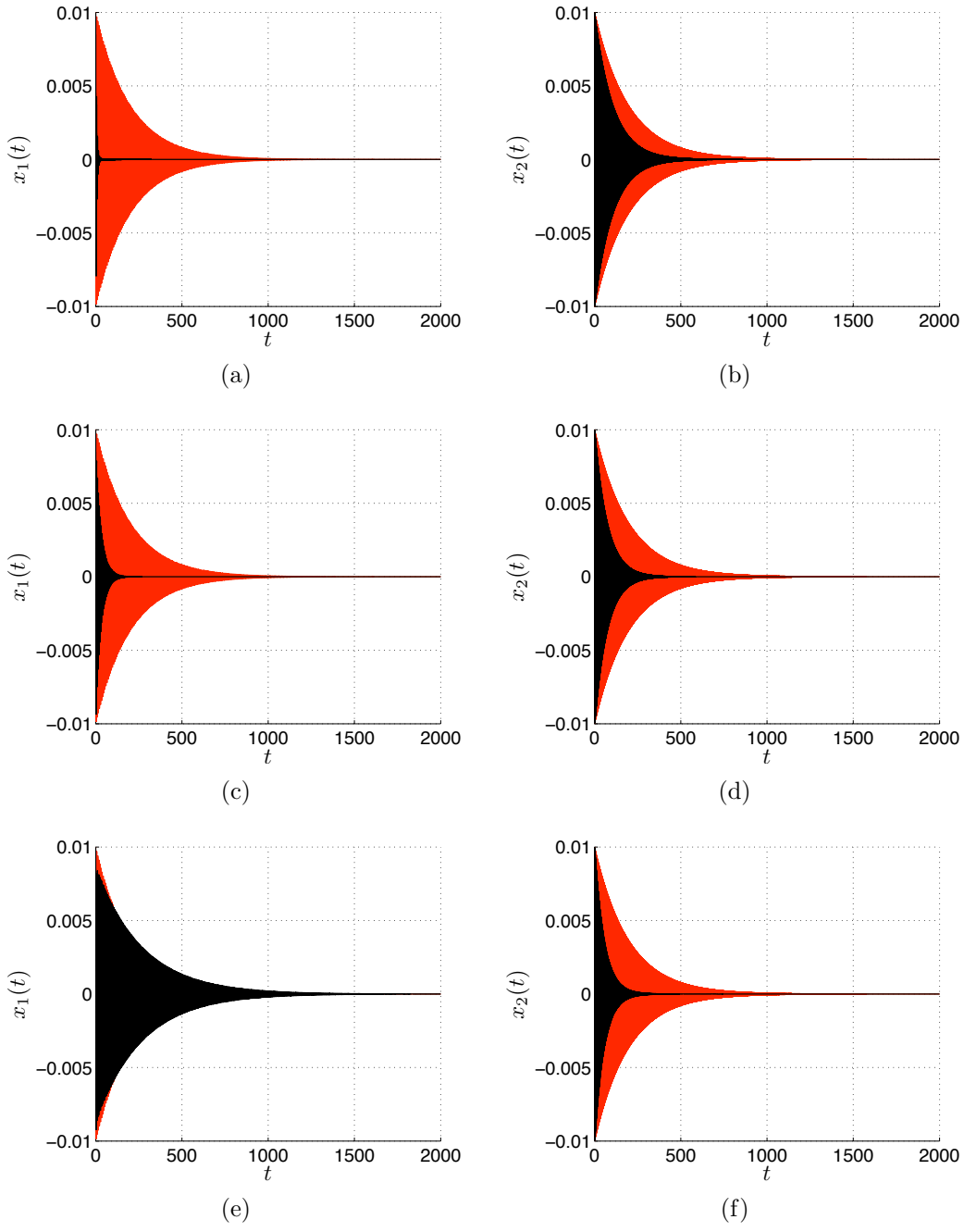

Figure 3.7: Time histories of a 2-DOF system subjected to the initial conditions ($x_1(0) = 0.01, x_2(0) = 0.01$, $\dot{x}_1(0) = 0, \dot{x}_2(0) = 0$). Results are obtained for (a, b) first-order BLPF with $\tau = 0.17$, and $K = 0.4$, (c, d) second-order BLPF with $\tau = 0.14$, and $K = 0.4$, and (e, f) third-order BLPF with $\tau = 0.07$, and $K = 0.4$.

Chapter 4

Experimental Implementation on a Macro-Cantilever Beam and a Micro-Cantilever Sensor

In this Chapter, we carry two different experimental implementations on systems with uncoupled frequencies to validate the theoretical concepts and demonstrate the ability of filter-augmented delayed-feedback algorithms to simultaneously reduce the vibrations of multiple vibration modes using a single gain-delay combination. In the first demonstration, we use a filter-augmented delayed-position feedback algorithm to mitigate the vibrations of a macrocantilever beam. In the second demonstration, we implement a filter-augmented delayed-velocity feedback algorithm to mitigate the vibrations of a microcantilever sensor.

4.1 Experimental Implementation

To demonstrate the influence of augmenting low-pass filters on the ability of delayed-feedback algorithms to mitigate vibrations of continuous systems and the stability margins of the controller, we consider two experimental implementation. The first treats the reduction of a macro-cantilever's beam vibrations using a single-input single-output filter-augmented delayed-position feedback controller. The second involves rejecting external disturbances on a micro-cantilever sensor using a single-input single-output delayed-velocity feedback controller.

4.1.1 Reduction of a macro-cantilever beam's vibrations using a filter-augmented delayed-position feedback

We consider a stainless-steel cantilever beam subjected to external base excitations, Fig. 4.1. The control effort is applied as an external moment exerted by a piezoelectric layer attached to the beam's surface. To model the system, we assume an isotropic inextensible Euler-Bernoulli beam and consider only planar motions. With these assumptions, the equations of motion and associated boundary conditions can be written as [50]

$$\rho A\ddot{v} + c\dot{v} + EIv^{iv} = q(s,t^*) + \rho A a_b(t^*), \tag{4.1}$$

$$v = 0 \quad and \quad v^{'} = 0 \quad at \quad s = 0, \quad v^{''} = 0 \quad and \quad v^{'''} = 0 \quad at \quad s = l, \tag{4.2}$$

where v is the displacement component along the y-axis, s is the neutral axis, $t^\star$ is time, ρ is the density; l, t_b, and w are the beam length, thickness, and width, respectively; $A = t_b w$ is the beam cross-sectional area; c is the coefficient of linear viscous damping per unit length; E is the beam Young's modulus of elasticity; I is the area moment of inertia about the neutral axis, a_b is the transversal acceleration of

the supported end which is assumed to be harmonic of the form $h_0 \cos(\Omega^* t^*)$, where h_0 and Ω^* are its amplitude and frequency, respectively; and the primes and overdots represent derivatives with respect to s and t^*. Finally, $q(s, t^*)$ is a distributed moment applied by the piezoelectric layer to mitigate the beam vibrations and is given by

$$q(s, t^*) = \frac{\partial^2 M}{\partial s^2}, \tag{4.3}$$

where

$$M = b d_{31} E_a (t_a + t_b) V_a(t^*)[H(s - s_1) - H(s - s_2)], \tag{4.4}$$

where b and t_a are the width and thickness of the piezoelectric layer, respectively; d_{31} is a piezoelectric constant; E_a is the actuator Young's modulus; $V_a(t^*)$ is the actuation voltage; $H(s)$ is the Heaviside step function; and s_1 and s_2 are, respectively, the starting and ending coordinates of the piezoelectric layer.

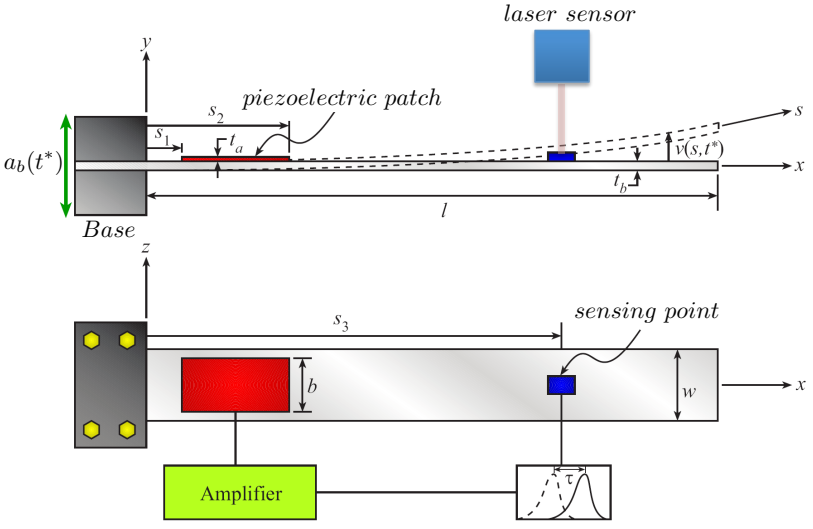

Figure 4.1: A schematic drawing of a piezoelectrically-actuated cantilever beam.

The feedback signal $y_f(t^*)$ is obtained by measuring the deflection at a point s_3

along the beam using a laser sensor, see Fig. 4.2 for the actual experimental setup,

$$y_f(t^*) = K_s v(s_3, t^*), \tag{4.5}$$

where K_s is the gain of the sensor. The controller's actuation voltage, $V_a(t^*)$, is obtained by passing the sensor's signal through a BLPF according to Equation (4.5), then amplified by a proper gain, K, delayed by a proper delay, τ^*, and supplied to the piezoelectric patch as a input voltage which can be written as

$$V_a(t^*) = K y_1(t^* - \tau^*). \tag{4.6}$$

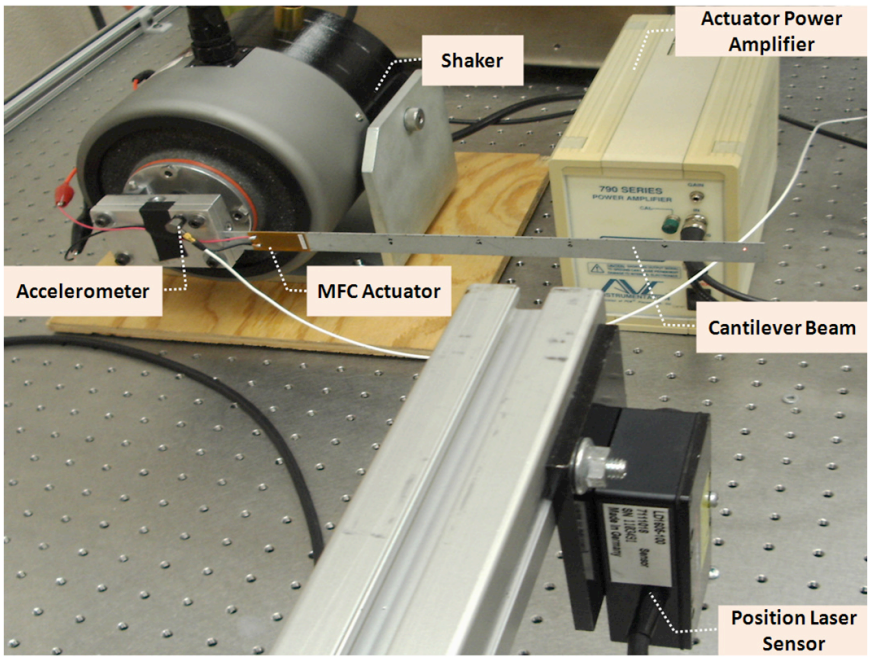

Figure 4.2: Setup of the cantilever beam experiment.

Substituting Equation (4.6) into Equation (4.7), the moment exerted by the piezoelectric patch on the beam becomes

$$M = K b d_{31} E_a (t_a + t_b) y_1(t^* - \tau^*)[H(s - s_1) - H(s - s_2)] \tag{4.7}$$

To discretize Equation (4.1), we use a Galerkin expansion in which we express the beam's deflection, $v(s,t^*)$ as a linear combination of an infinite set of spatial mode shapes, $\phi_i(s)$, multiplying some generalized temporal coordinates, $w_i(t^*)$, such that

$$\phi_i(s) = C_i \left(\cosh(r_i s) - \cos(r_i s) - \frac{\cosh(r_i L) + \cos(r_i L)}{\sinh(r_i L) + \sin(r_i L)} \times [\sinh(r_i s) - \sin(r_i s)] \right), \tag{4.8}$$

and

$$v(s,t^*) = \sum_{i=1}^{\infty} \phi_i(s) w_i(t^*), \tag{4.9}$$

where r_i is obtained via the solution of $1+\cos(r_i s)\cosh(r_i s) = 0$. Substituting Equations (4.7) and (4.9) into Equation (4.1), taking the inner product of the outcome with $\phi_j(s)$, integrating over the length of the beam, and imposing the orthogonality conditions on the linear mode shapes, we obtain the following set of linearly-coupled ordinary-differential equations for the $w_j(t^*)$

$$\begin{aligned} &\ddot{w_j}(t^*) + 2\mu_j^* \dot{w_j}(t^*) + \omega_j^{*2} w_j(t^*) = M_j^* y_1(t^* - \tau^*) + f_j^* \cos(\Omega^* t^*), \\ &j = 1, 2, ..., \infty \end{aligned} \tag{4.10}$$

where ω_j^* is the *j-th* modal frequency of the beam, μ_j^* is the *j-th* modal viscous damping coefficient; f_j^* is the amplitude of excitation, and the M_j^* is a constant describing the projection of the external excitation and the piezoelectric actuation onto the *j-th* vibration mode. M_j^*, μ_j^* and f_j^* can be written as

$$\begin{aligned} &M_j^* = K \frac{b d_{31} E_a K_s (t_a + t_b)}{\rho A} [\phi_j^{'}(s_1) - \phi_j^{'}(s_2)],\ \mu_j^* = \frac{c}{\rho A}, \\ &f_j^* = \frac{h_0}{\rho A} \int_0^l \phi_j \, ds,\ \omega_j^{*2} = \frac{EI}{\rho A} r_j^4. \end{aligned} \tag{4.11}$$

We non-dimensionalize Equation (4.10) using the nondimensional time $t = t^* \omega_1^*$, delay period $\tau = \tau^* \omega_1^*$, and the generalized coordinate $x_j^*(t) = w_j(t^*)/l$. This yields

Table 4.1: Geometric and material properties of the beam and piezoelectric actuator.

Beam	
Modulus of elasticity, $E[GPa]$	210
Density, $\rho[kg/m^3]$	7500
Length, $l[mm]$	300
Width, $w[mm]$	15
Thickness, $t_b[mm]$	0.783
PZT patch starting point distance, $s_1[mm]$	20
PZT patch ending point distance, $s_2[mm]$	48
Laser sensor measuring point distance, $s_3[mm]$	290
MFC (MFC M4010)	
Electromechanical coupling coefficient, $d_{31}[m/V]$	-210×10^{-12}
Modulus of elasticity, $E_a[GPa]$	30
Thickness, $t_a[mm]$	0.3
Length, $s_2 - s_1[mm]$	28
Width, $b[mm]$	15

equations that are identical to Equations (3.7a) and (3.7b) with

$$\begin{aligned} &M_j = K\frac{bd_{31}E_aK_s(t_a+t_b)}{\rho A}[\phi_j^{'}(s_1) - \phi_j^{'}(s_2)],\ \mu_j = \frac{\mu_j^*}{\rho A\omega_1^*}, \\ &f_j = \frac{f_j^*}{\rho A\omega_1^* l},\ c_j = K_s\phi_j(s). \end{aligned} \tag{4.12}$$

With this formulation, the stability analysis can be performed using Equation (3.9).

Stability Pockets

We perform several sets of experiments to validate the theoretical results pertaining to the effect of the filter's dynamics on the stability pockets. Table 4.1 lists the geometric and material properties of the cantilever beam and Micro Fiber Composite (MFC) actuator used in the experiments.

We start by generating the stability maps for different filters. The stability boundaries are generated by choosing a given controller gain then increasing the delay

incrementally. At each gain-delay combination, the beam is subjected to an initial condition and the response is monitored using a laser sensor. If the response decays with time then the gain-delay combination is stable, otherwise, it is unstable. In the first experiment, no filter is used. As such, small-amplitude high-frequency excitations due to noise were allowed into the feedback signal. In that case, even using the smallest feedback gains, higher-modes' oscillations were always excited for any value of the delay. Therefore, we could not generate any stability pockets. Subsequently, we added a first-order BLPF with a cut-off frequency that is seven times the first modal frequency ($\epsilon = 0.1429$). This cut-off frequency permits the second-mode's dynamics ($\omega_2 = 6.93\omega_1$) into the feedback signal. Figure 4.3(a) depicts the stability pockets in that case clearly indicating a very good agreement between the experimental and theoretical results. We also observe the clear influence of the second mode on the stability of the closed-loop system. However, due to filter augmentation, the influence of the third and higher modes, at least for the range of controller's gain considered, is not apparent in the stability pockets.

In Fig. 4.3(b), the cut-off frequency of the first-order BLPF is decreased to four times the first-modal frequency. Although the cut-off frequency is almost half that of the second-mode frequency, we observe very little effect on the stability pockets as they are only slightly shifted along the gain axis. This indicates that choosing the cut-off frequency such that it is smaller than a given vibration mode does not guarantee that the influence of that vibration mode can be neglected.

In Fig. 4.3(c), we keep the cut-off frequency constant but increase the order of the filter to third order. Now, we observe two distinct shifts, a shift of the whole stability diagram to the left along the delay axis due to the delay introduced by the filter, and a shift of the stability pockets associated with the second mode up along the gain axis. This illustrates that the order of the filter has a significant influence on the stability of the response. Choosing a fifth-order BLPF as shown in Fig. 4.3(d) completely eliminates the effect of the second mode on the response stability. This

provides a larger stability pocket in the gain-delay domain which increases the robustness to variations in the delay, control gain, and system parameters. It is also worth mentioning, that due to restriction on the maximum moment exerted by the MFC, the maximum gain achieved by the controller is limited to $K = 0.29$ as shown in the figures.

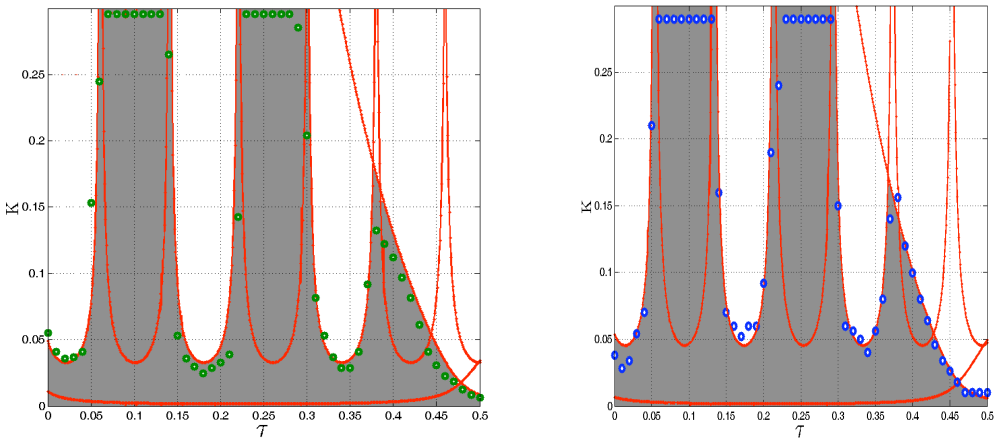

(a) (b)

(c) (d)

Figure 4.3: Gain-delay stability maps using the theoretical model (solid lines) and experimental data (circles). Results are obtained for a) first-order BLPF with $\epsilon = 0.1429$, b) first-order BLPF with $\epsilon = 0.25$, c) third-order BLPF with $\epsilon = 0.25$, and d) fifth-order BLPF with $\epsilon = 0.25$

Performance in mitigating external disturbances

We evaluate the effectiveness of the controller to mitigate oscillations resulting form an external disturbance by subjecting the beam to an impulse at the base using the electrodynamic shaker shown in Fig. 4.2. Figures 4.4(a)-4.4(d) depict time histories of the beam response corresponding to different control parameters K and τ. Since, as demonstrated previously, the damping intensity which is governed by the dominant eigenvalue varies within a stability pocket, the performance of the controller depends on the gain delay chosen in the feedback. For a third-order BLPF filter with $\epsilon = 0.25$, the control parameters ($K = 0.2$, $\tau = 0.1$) showed excellent disturbance rejection properties.

Performance in mitigating persistent harmonic excitations

We also investigate the forced-response of the cantilever beam to an external harmonic excitation applied at the base using the electrodynamic shaker. Figures 4.5(a)-4.5(b) show the frequency-response curves for the first and second modes. It is observed that a filter-augmented delayed-position feedback controller is capable of reducing the beam vibrations for both the first and second mode simultaneously using the same gain-delay combinations and one piezoelectric patch. This represents excellent performance characteristics of the controller as one can now mitigate large beam oscillations at different frequencies using a single input and a single output and the same control parameters.

4.1.2 Reduction of a micro-cantilever sensor vibration using a filter-augmented delayed-velocity feedback

One important area where such delayed-feedback control algorithms can prove very beneficial is microsystems. Microdevices are subjected to a myriad of low and high

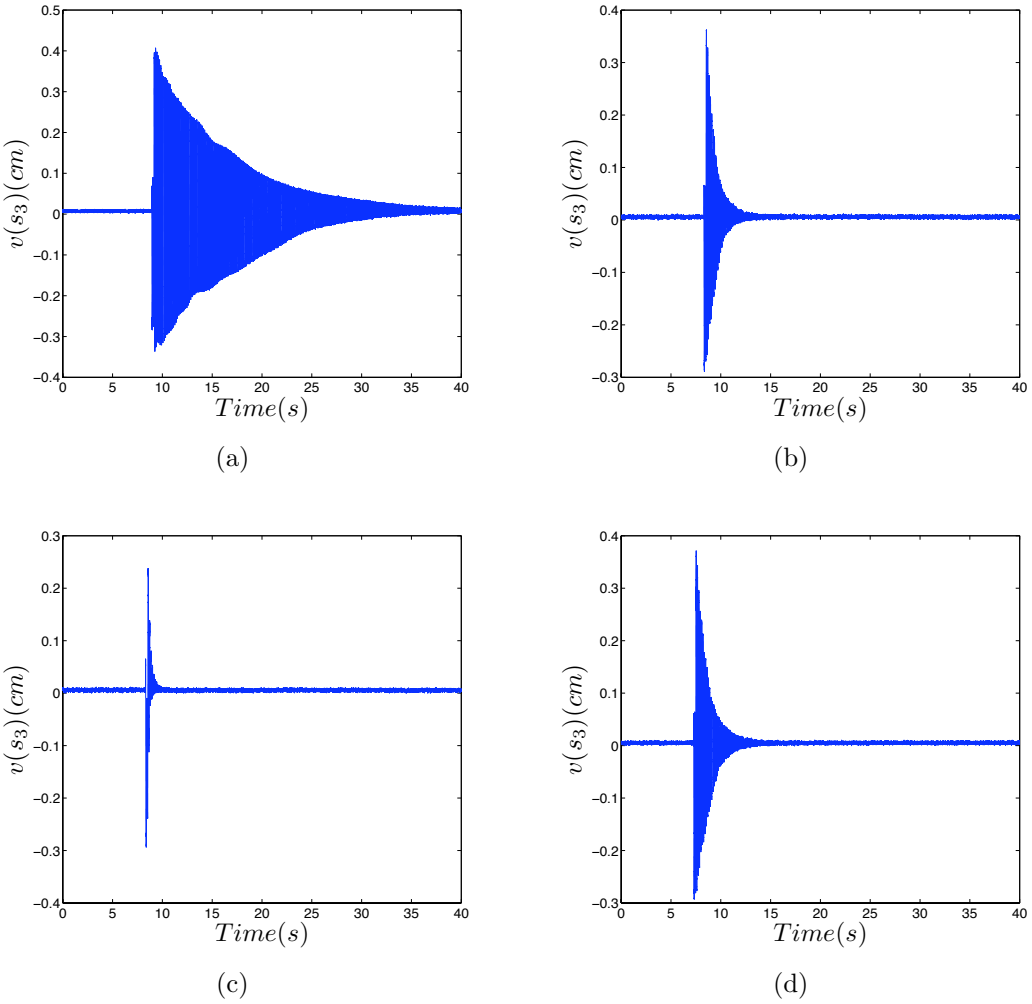

Figure 4.4: Experimental time history of the beam's response to an input impulse using a third-order BLPF with $\epsilon = 0.25$. a) Response without control, b) controlled response with $K = 0.08$ and $\tau = 0.1$, c) controlled response with $K = 0.2$ and $\tau = 0.1$, and d) controlled response with $K = 0.08$ and $\tau = 0.25$

frequency external excitations emanating from external package vibrations, shock, impact, and electrical interferences. If not suppressed, such disturbances could be very detrimental to the system's performance and are usually responsible for decreased fatigue life and device failure. To overcome these issues, there is a growing interest in implementing feedback control algorithms to mitigate the effect of external excitations on the response of microdevices.

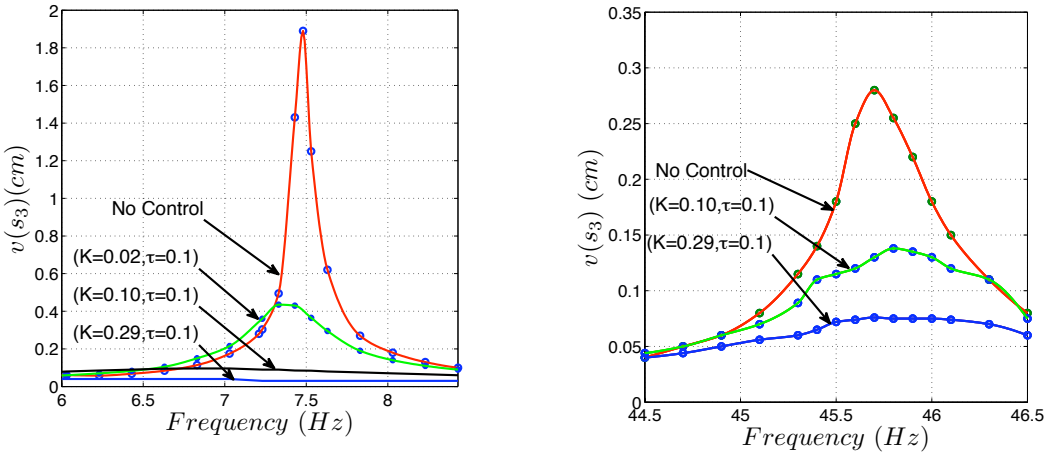

(a) (b)

Figure 4.5: Frequency-response curves of the beam with first-order BLPF. a) First-mode response and b) second-mode response.

Micro-cantilever beams represent one of the most widely utilized structures at the micro-scale and has significant applications in atomic force microscopy, scanning force microscopy, and micro-mechanical sensing. At that scale, the implementation of feedback control can be a very formidable task. Issues related to the complexity and availability of feedback signals, sampling rates, as well as data storage pose significant obstacles. In addition, due to the extremely high natural frequency associated with microdevices (10 kHz-10 MHz), the presence of the infinitesimal measurement delays in the control loop could be of the same order of the response period channeling energy into and out of the system at incorrect time intervals, thereby producing instabilities and rendering controllers' performance ineffective.

Delayed-feedback algorithms offer unique advantages at the microscale. System delays due to filtering, processing, sampling, and input actuation can be successfully augmented into a larger delay period which when combined with a proper feedback gain and augmented with a proper filter can be utilized as an effective mechanism for vibration mitigation at the microscale. Note that this marks one of the initial

experimental implementations of such algorithms at the microscale. In this work, we conduct two sets of experiments to investigate the effectiveness of a filter-augmented delayed-velocity feedback controller for real-time reduction of a microcantilever sensor's vibration. The geometric and material properties of the beam are listed in Table 4.2.

Table 4.2: Geometric and material properties of the micro-cantilever sensor.

Silicon modulus of elasticity, $E[GPa]$	185
Silicon density, $\rho[kg/m^3]$	2350
Length, $l[\mu m]$	460
Width, $w[\mu m]$	50
Thickness, $t_b[\mu m]$	2
Primary modal frequency, $\omega_1^\star[Hz]$	11750
Quality factor, Q	87.8
Geometric non-linearity coefficient, $\alpha^\star$	2.43×10^{20}
Inertia non-linearity coefficient, $\beta^\star$	2.360883×10^{10}

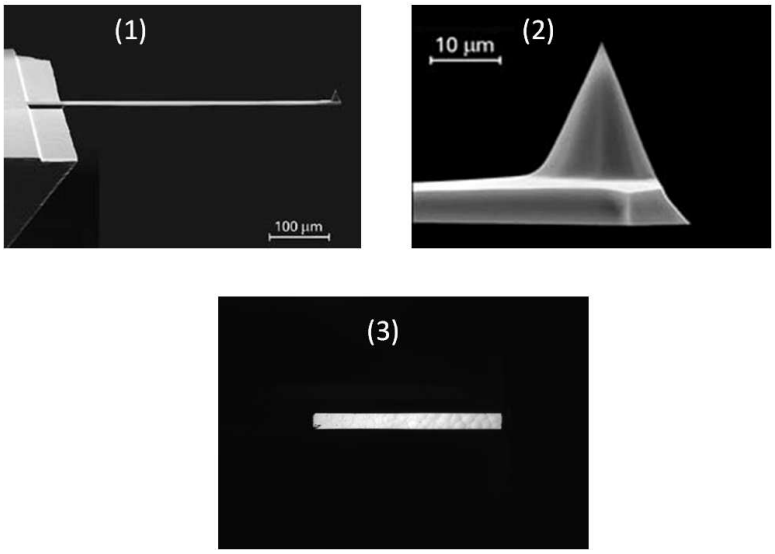

Figure 4.6: (1) CSC17/Cr-Au micro-cantilever fabricated by MikroMasch [1] (2) CSC17/Cr-Au microcantilever tip (3) CSC17/Cr-Au micro-cantilever backside.

The feedback signal is measured using a microsystem analyzer, the MSA-400 man-

ufactured by Polytech [85]. The analyzer which implements a combination of laser-doppler vibrometry, stroboscopic video microscopy, and white light interferometry, was utilized to measure the velocity of the micro-cantilever tip with a sub-picometer resolution. A digital signal processing board receives the feedback signal, multiplies it by the appropriate gain, and then delays it by a period sufficient to augment the inherent system delay without destabilizing the beam response. The feedback loop is closed when the conditioned and filtered signal is applied to a piezoelectric actuator mounted beneath the cantilever base, thus providing a base-excitation type feedback signal. A schematic of the experimental setup is shown in Fig. 4.7.

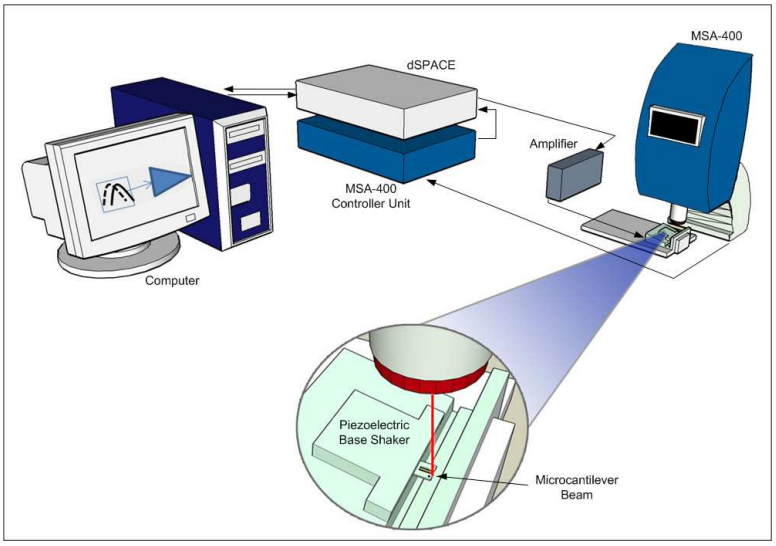

Figure 4.7: Schematic diagram of the experimental setup.

Using the stability analysis of Section 3.2, we map the controller gain-delay domain into stable and unstable regions as illustrated in Fig. 4.8(a) where the shaded regions represent combinations that yield an asymptotically stable cantilever response. In the experiments, we considered a third-order BLPF with $\epsilon = 0.3333$ as shown in Fig. 4.8.

In the first experiment, we investigate the ability of the controller to reject external

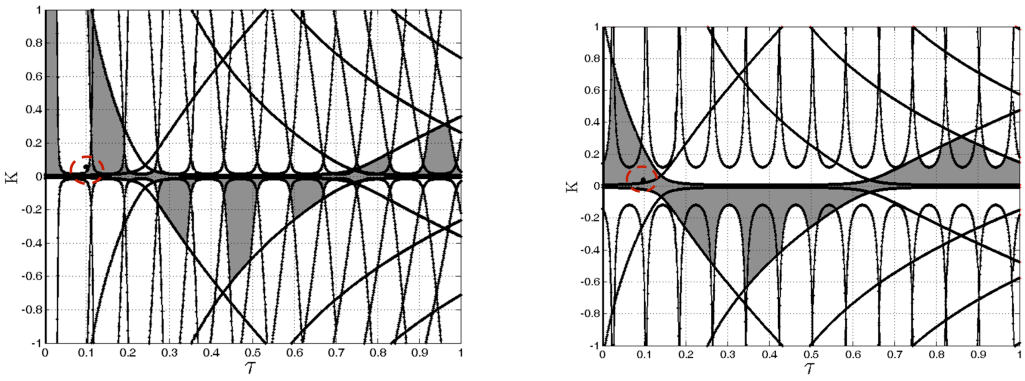

(a) (b)

Figure 4.8: Stability maps of the delayed velocity-feedback controller. Shaded regions represent stable solutions. a) No filter is used, and b) third-order filter with $\epsilon = 0.3333$.

disturbances. Towards that end, we utilize the piezoelectric actuator to generate a periodic square wave with a very low frequency $f_s = 20Hz$. Compared to the first modal frequency of the beam under consideration, $f_b \approx 11170Hz$, this frequency is very small, and, hence can be considered as a discrete disturbance event. The response of the uncontrolled beam to the square wave is shown in Fig. 4.9(b). It is clear that the beam undergoes large velocities at the disturbance point. When compared to the beam period, these oscillations have a very large settling time. On the other hand, when a delayed-velocity feedback signal ($K = 0.085$, $\tau = 0.1$) is applied, the beam deflection remains within the noise level, Fig. 4.9(c).

In the second set of experiments, we investigate the ability of the controller to mitigate external periodic excitations near its first modal frequency. The excitation frequency is varied around the first modal frequency of the beam and the steady-state tip velocity is recorded at $1000Hz$ steps. In the first experiment, 5 $Volt$ input voltage is applied to the piezoelectric actuator and the uncontrolled response is shown in Fig. 4.10. When a filter-augmented delayed-velocity feedback algorithm ($K = 0.085, \tau = 0.1$) is incorporated in the feedback, the tip velocity is reduced significantly and the peak response is shifted towards larger values of the excitation

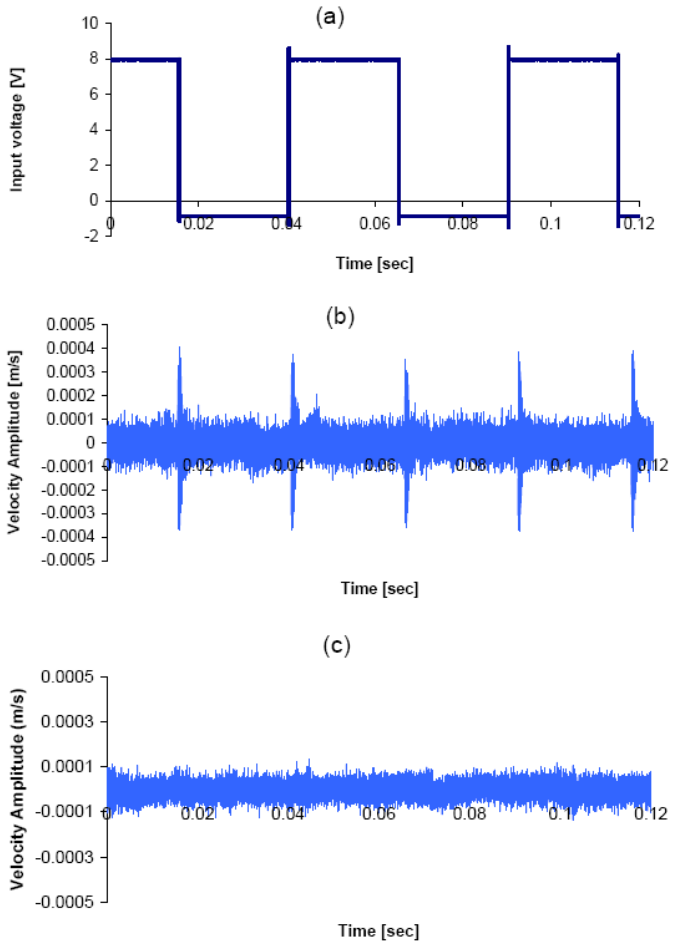

Figure 4.9: a) Input disturbance, b) Tip velocity of the beam without control, and c) Tip velocity with third-order filter and $\epsilon = 0.3333$ using control parameters ($K = 0.085$, $\tau = 0.1$).

frequency, Fig. 4.10(a). Another experiment was carried out for a larger input voltage of 9 $Volt$, Fig. 4.10(b). Again, we can see that by selecting the controller gain and delay based on the pockets shown in Fig. 4.8(b), we are capable of reducing the amplitude of the response velocity significantly.

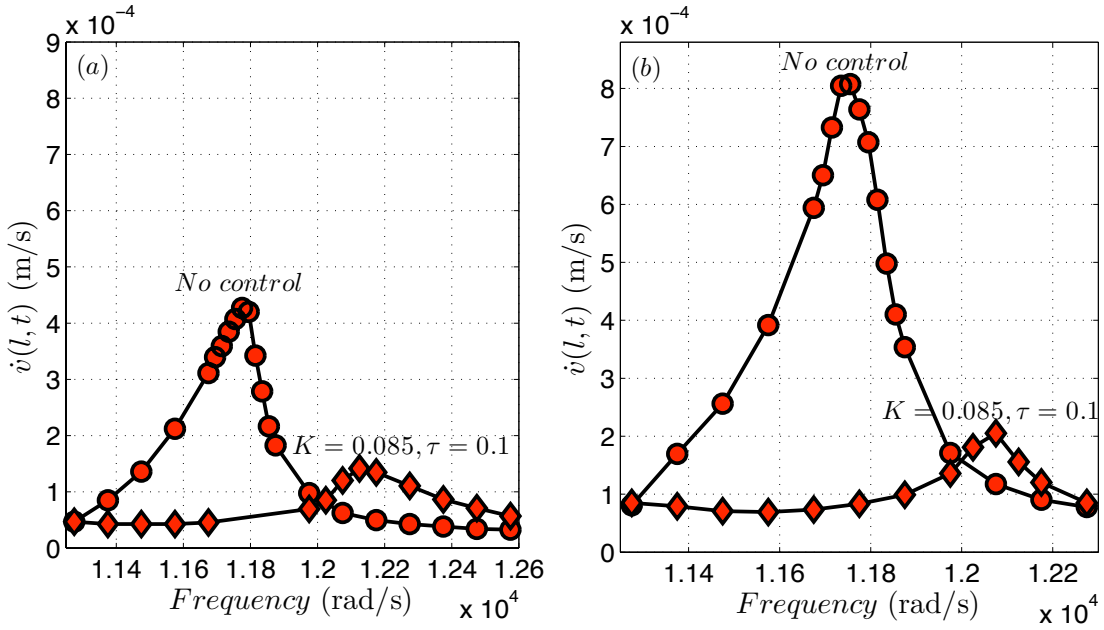

Figure 4.10: Microcantilever frequency-response curves before and after applying the designed controller with third-order filter and $\epsilon = 0.3333$. Controlled output is obtained using $K = 0.085$, and $\tau = 0.1$. Results are obtained for a) input voltage of 5 $Volts$, and b) input voltage of 9 $Volts$.

Chapter 5

Suppression of The Coupled Flexural-Torsional Vibrations of Cantilever Beams Using Filter-Augmented Position-Feedback Control Algorithms

This Chapter investigates the implementation of delayed-feedback control algorithms on a continuous system that can only be discretized into a system of linearly-coupled equations. As an example, the Chapter considers the problem of suppressing the coupled flexural-torsional oscillations of a cantilever beam with an asymmetric tip rigid body using a single piezoelectric patch and a single laser sensor. Following Euler-Bernoulli's beam theory, a system's model consisting of two Partial Differential Equation (PDEs) and the associated boundary conditions is developed and

subsequently validated. To implement the controller and analyze the stability of the closed-loop system, the resulting system of PDEs and boundary conditions is reduced into a set of linearly-coupled Ordinary Differential Equations (ODEs) using a Galerkin discretization scheme. The stability of the closed-loop system in the gain-delay space and in the presence of low-pass filters is also investigated using a numerical technique that involves transforming the resulting set of Delay Differential Equations (DDEs) into an equivalent PDE followed by a discretization of the PDE in the delay space into a set of equivalent ODEs. Using the resulting stability maps, the effectiveness of the controller in rejecting external disturbance and suppressing large-amplitude oscillations resulting from harmonic-base excitations is investigated theoretically and experimentally for different tip rigid bodies, filters, and piezoelectric patch orientations.

5.1 Introduction

In the previous Chapter, we considered the implementation of delayed-position feedback algorithms to reduce the multi-modal oscillations of a linearly-uncoupled system of equations resulting from the discretization of one linear PDE and its associated boundary conditions. As an example, we analyzed the problem of suppressing large-amplitude oscillations of an Euler-Bernoulli cantilever beam and studied the influence of low-pass filters on the stability of the closed-loop system in the gain-delay space and on the robustness of the controller to parameter's uncertainties. In this Chapter, we investigate the implementation of similar delayed-feedback control algorithms on a continuous system that can only be discretized into a set of linearly-coupled equations. As an example, we consider the problem of suppressing the coupled flexural-torsional oscillations of a cantilever beam with an asymmetric tip rigid body using a single piezoelectric patch and a single laser sensor. Following Euler-Bernoulli's beam theory, we develop and validate a system's model consisting

of two PDEs and the associated boundary conditions. To implement the controller and analyze the stability of the closed-loop system, we reduce the resulting system of PDEs and boundary conditions into a set of linearly-coupled ODEs using a Galerkin discretization scheme. We also investigate the stability of the closed-loop system in the gain-delay space and in the presence of low-pass filters using a numerical technique that involves transforming the resulting set of DDEs into an equivalent PDE followed by a discretization of the PDE into a set of equivalent ODEs in the delay space. Using the resulting stability maps, we investigate theoretically and experimentally the effectiveness of the controller in rejecting external disturbance and suppressing large-amplitude oscillations resulting from harmonic-base excitations for different tip rigid bodies, filters, and piezoelectric patch orientations.

While the problem at hand marks one of the first implementations of a delayed-feedback algorithm on an infinite-dimensional system that can only be discretized into a set of linearly-coupled ODEs, the research is also motivated by recent developments in the fields of turbomachinery, thin-walled sections, light-weight flexible space structures, and wind turbine blades that have undoubtedly propelled the research interest in the coupled flexural-torsional vibrations of structures. Such systems are known to experience large-amplitude coupled torsional-bending vibrations due to (*i*) linear geometric coupling as a result of asymmetries in the structure, (*ii*) non-uniform stiffness distribution, (*iii*) linear elastic coupling due to anisotropies, and (*iv*) nonlinear geometric coupling of linear in-plane and out-of-plane flexural modes due to large-amplitude vibrations and internal resonances [86].

Research studies addressing this important problem can be divided into two parts: some dealing with the modeling and vibration analysis aspects of it, while others investigating the development of control algorithms to mitigate large-amplitude coupled flexural-torsional vibrations that could arise due to external disturbances and/or persistent base excitations. From a modeling perspective, different methods were proposed to approximate the vibration response by utilizing the well-

established beam or plate theories including Euler–Bernoulli Theory, Vlasov Theory, and Timoshenko Theory [87, 88].

Many attempts have also been made to understand the vibratory response of many beam configurations. Adam [89] analyzed the coupled flexural–torsional vibrations of distributed–parameter beams . Eslimy–Isfahany [90] investigated the free vibratory motion of coupled bending–torsional beams and studied the dynamic response characteristics under random bending and torsional loads. Low [91] evaluated the eigenfrequency equation of a beam carrying multiple concentrated masses at arbitrary locations. Oguamanam [92] examined the free vibration of an Euler-Bernoulli beam with a rigid tip mass whose center of gravity does not coincide with its point of attachment to the beam. Banerjee [93] developed an exact dynamic stiffness matrix for a twisted Timoshenko beam in order to investigate its free vibration characteristics. Shubov [94] compared the asymptotic behavior of coupled Euler-Bernoulli and Timoshenko beam models. Gokdag and Kopmaz [95] studied coupled flexural-torsional free and forced vibrations of a beam with tip or in-span attachments.

In other demonstrations, Paolone et al. [96] analyzed the stability of narrow rectangular cross-section beams with thin walls under simultaneous action of conservative and nonconservative loads. Salarieh and Ghorashi [97] analyzed the free vibrations of a cantilevered Timoshenko beam with a rigid tip mass. They also compared the results obtained using the Timoshenko model with those of three other beam models (Euler-Bernoulli, shear, and Rayleigh). Rudavskii and Vikovich [98] addressed the forced flexural–torsional vibrations of a cantilever beam of constant cross section.

Many research efforts were also directed towards implementing different control techniques to suppress and mitigate harmful vibrations induced by external disturbances. Sun and Mills [99] described combining a proportional derivative feedback algorithm with a distributed piezoelectric polymer actuator for vibration suppression. They also investigated a control algorithm based on Lyapunov approach to

control a single-link flexible manipulator. Pai et al. [100] investigated the suppression of steady-state vibrations of a cantilevered and skewed aluminum plate using the nonlinear saturation phenomenon. Morita et al. [101] implemented a robust control algorithm for suppression of the bending–torsional vibrations of a flexible arm with a non-symmetric rigid tip mass. Jalili et al. [102] proposed an adaptive, non model-based controller for tracking control of a flexible cantilever beam with a translational base support. A piezoelectric patch actuator was bonded on the top surface of the beam to apply a controlled moment for vibration suppression. Park [103] presented a general approach for utilizing a resonant shunt–dampers for vibration suppression on a beam using a piezoelectric sensor/actuator combinations. He observed that additional damping can be introduced to the system using the shunt damping effect.

5.2 Model Development

We consider the linear dynamics of a cantilever beam of length, L, width w, and thickness, t_b with a rigid body attached to its free end as shown in Fig. 5.1. The center of gravity of the attached rigid body does not coincide with the neutral axis of the beam, thereby producing a moment which can excite torsional oscillations. As a result, the beam undergoes coupled flexural-torsional motions. The flexural and torsional dynamics are described, respectively, via the spatio-temporal functions, $v(x,t^*)$, and $\psi(x,t^*)$.

To describe the response behavior, we consider four coordinate systems as shown in Fig. 5.1. The first of which, the $\hat{a}-frame$, is an inertial frame located at point O'. The second, the $\hat{b}-frame$ is located at the tip of the beam on the neutral axis, points S, and is formed by rotating the $\hat{a}-frame$ with an angle $\partial v(x,t^*)/\partial x|_{x=L}$ about $\hat{a}_3$. The third frame, $\hat{c}-frame$, is also located at point S and is formed by

rotating the $\hat{b} - frame$ with an angle $\psi(L, t^*)$ about $\hat{b}_1$. Finally, the $\hat{d} - frame$ is a body-coordinate frame located at the center of gravity, G, of the tip rigid body.

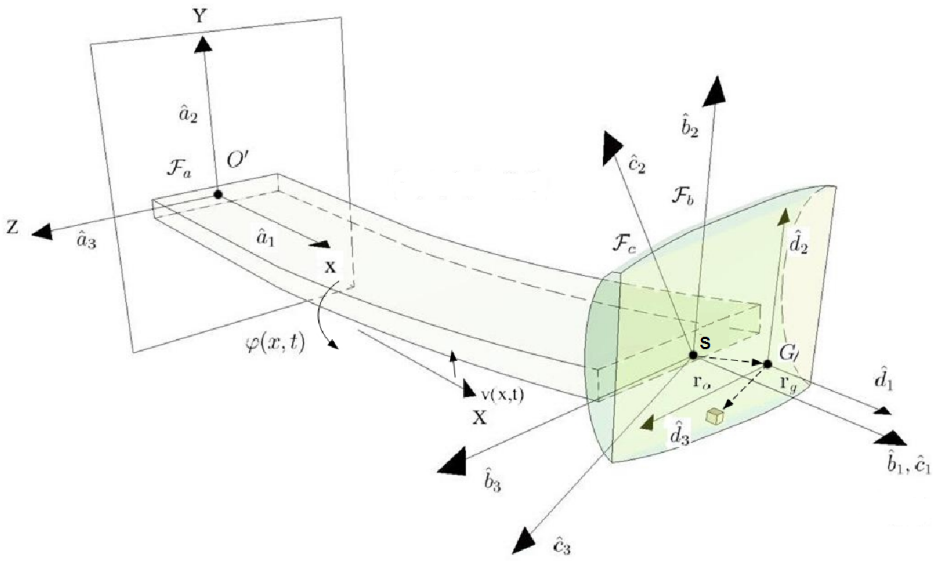

Figure 5.1: Schematic of the cantilever beam with a tip rigid body and the coordinate frames used to describe its motion.

To derive the equations of motion, we adopt the linear Euler-Bernoulli's beam theory and write the total kinetic energy as

$$\boxed{\mathbb{T} = \frac{1}{2}\int_{m_b} \dot{r}_b \cdot \dot{r}_b \, dm_b + \frac{1}{2}\int_{m_t} \dot{r}_m \cdot \dot{r}_m \, dm_t,} \tag{5.1}$$

where the overdot represents a derivative with respect to time, t^*, m_b denotes the mass of the beam, m_t denotes the mass of the rigid body;

$$r_b = x\hat{a}_1 + v(x, t^*)\hat{a}_2 - z\psi(x, t^*)\hat{b}_2 + y\psi(x, t^*)\hat{b}_3 \tag{5.2}$$

is the position vector to a differential beam element; and

$$r_m = L\hat{a}_1 + v(L, t^*)\hat{a}_2 + r_o + r_g \tag{5.3}$$

is the position vector to a differential element of the rigid body, all measured with respect to point O'. Here, $r_o = o_x\hat{c}_1 + o_y\hat{c}_2 + o_z\hat{c}_3$. The velocity of the beam element as described in the inertial frame can be written as

$$\dot{r}_b = \dot{v}\hat{a}_2 - z\dot{\psi}\hat{b}_2 + y\dot{\psi}\hat{b}_3 + \dot{v}'_L\hat{b}_3 \times (-z\psi\hat{b}_2 + y\psi\hat{b}_3), \tag{5.4}$$

where the prime denotes a derivative with respect to the spatial coordinate x, $\times$ represents the cross product, and $\dot{v}'_L \equiv \dot{v}'(L,t)$. Similarly, the velocity of the differential tip-mass element can be described as

$$\dot{r}_m = \dot{v}_L\hat{a}_2 + (\dot{v}'_L\hat{a}_3 + \dot{\psi}_L\hat{c}_1) \times r_o + \dot{r}_g. \tag{5.5}$$

Substituting Equation (5.5) and Equation (5.4) into Equation (5.1), we obtain

$$\begin{aligned}\mathbb{T} =& \frac{1}{2}\rho A\int_0^L \dot{v}^2 dx + \frac{1}{2}\rho\kappa^2\int_0^L \dot{\psi}^2 dx + m_t[\dot{v}_L(\dot{v}'_L o_x + \dot{\psi}_L o_z)] \\ &+ \frac{1}{2}m_t[\dot{v}_L^2 + (o_x^2 + o_y^2)\dot{v}_L'^2 + 2o_x o_z\dot{\psi}_L\dot{v}'_L + (o_y^2 + o_z^2)\dot{\psi}_L^2] \\ &+ \frac{1}{2}\int_{m_t} \dot{r}_g \cdot \dot{r}_g dm_t + H.O.T,\end{aligned} \tag{5.6}$$

where ρ is the mass density of the beam, A is its cross-sectional area, $H.O.T$ is used to represent higher order terms that yield nonlinearities in the equations of motion, and

$$\kappa^2 = \int_{-t_b/2}^{t_b/2}\int_{-w/2}^{w/2} (y^2 + z^2)dydz \tag{5.7}$$

is the radius of gyration of the beam's cross section. The last term in Equation (5.6) can be further simplified to

$$\frac{1}{2}\int_{m_t} \dot{r_g} \cdot \dot{r_g} dm_t = \frac{1}{2}(I_{11}\dot{\psi}^2 + I_{33}\dot{v}_L'^2) + I_{13}\dot{v_L'}\dot{\psi} + H.O.T \tag{5.8}$$

where I_{11}, I_{33}, and I_{13} are the principle and product mass moment of inertias of the rigid body as calculated in the body rotating frame.

Substituting Equation (5.8) into Equation (5.6) and rearranging, we obtain

$$\begin{aligned}\mathbb{T} =&\frac{1}{2}\rho A\int_0^L \dot{v}^2 dx + \frac{1}{2}\rho\kappa^2\int_0^L \dot{\psi}^2 dx + \frac{1}{2}m_t\dot{v}_L^2 + m_t\dot{v}_L(\dot{v}'_L o_x + \dot{\psi}_L o_z)\\ &+\frac{1}{2}(I_{11}+m_t(o_y^2+o_z^2))\dot{\psi}_L^2 + \frac{1}{2}(I_{33}+m_t(o_x^2+o_z^2))\dot{v}_L'^2\\ &+(I_{13}+m_t o_x o_z)\dot{\psi}_L\dot{v}'_L + H.O.T.\end{aligned} \tag{5.9}$$

The potential energy of the system, $\mathbb{U}$, can be written as

$$\boxed{\mathbb{U} = \frac{1}{2}EI_z\int_0^L v''^2 dx + \frac{1}{2}GJ\int_0^L \psi''^2 dx + m_t g o_y \sin\psi_L,} \tag{5.10}$$

where E is the Young's modulus of the beam, G is its Shear modulus, $I_z = \frac{1}{12}wt_b^3$ is the second moment of area of the beam's cross-section around the $z-axis$, $J = \frac{16w^4}{3}\left[1 - \frac{192(w/t_b)}{\pi^5}\sum_{n=0}^{\infty}\frac{1}{(2n+1)^5}\tanh\frac{(2n+1)^5}{2(w/t_b)}\right]$ is the polar moment of inertia of the beam accounting for cross-sectional warping effects, and g is the gravitational acceleration.

To apply the control effort, a piezoelectric actuator is attached to the surface of the beam as shown in Fig. 5.2. The work done by applying a voltage to this actuator can be written as

$$\boxed{\mathbb{W}^a = \frac{1}{2}\int_0^L M_z v'' dx + \frac{1}{2}\int_0^L T\psi' dx,} \tag{5.11}$$

where M_z and T represent, respectively, the bending moment and torque exerted by the actuator on the beam. These are given by

$$M_z = \alpha_1^* V_a(t^*)[H(x-s_1) - H(x-s_2)]\cos\beta, \tag{5.12a}$$

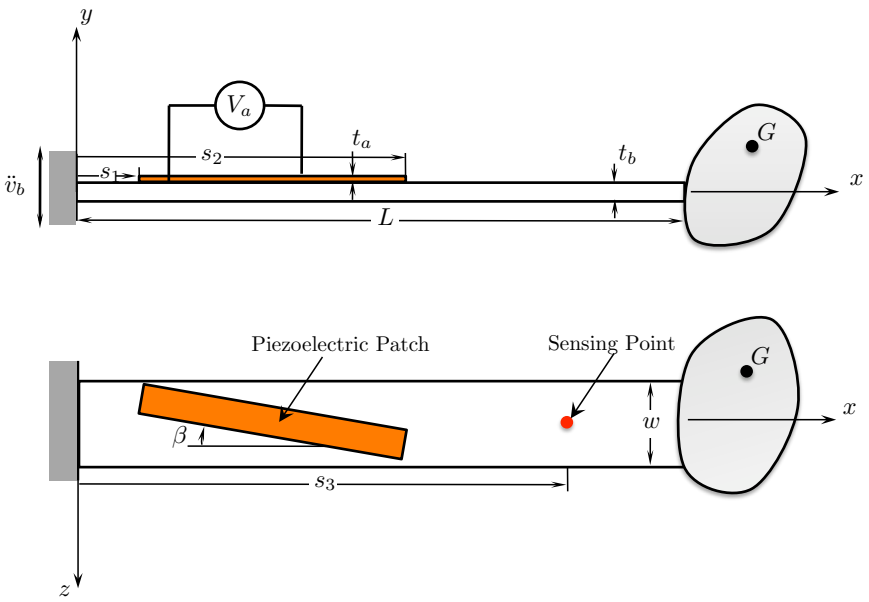

Figure 5.2: Schematic of a cantilever beam with attached tip rigid body and piezoelectric actuator.

$$T = \alpha_2^* V_a(t^*)[H(x - s_1) - H(x - s_2)] \sin\beta, \tag{5.12b}$$

where β is the angle that the patch makes with the $x - axis$ and

$$\alpha_1^* = b_a d_{31} E_a (t_a + t_b), \qquad \alpha_2^* = b_a d_{31} G_a (t_a + t_b). \tag{5.13}$$

Here, b_a and t_a are the width and thickness of the piezoelectric patch, E_a and G_a are its Elastic and Shear modulii, d_{31} is the piezoelectric constant, s_i are the starting and ending position of the actuator, V_a is the applied voltage, and $H(x)$ is the heaviside function. When β is equal zero, the actuation voltage yields a pure moment around the $z - axis$.

The non-conservative virtual work done by the external damping forces and an

external base excitation can be written as

$$\boxed{\delta\mathbb{W}^{nc} = -\int_0^L \rho A \ddot{v}_b \delta v dx - \int_0^L (C_b \dot{v}\delta v + C_t \dot{\psi}\delta\psi) dx,} \tag{5.14}$$

where C_b and C_t are viscous damping terms associated with the damping and torsional dynamics, and $\ddot{v}_b$ is the base acceleration.

With these definitions, the partial differential equation of motion and the associated boundary conditions can be derived using Hamilton's principle which states that

$$\boxed{\int_{t_1}^{t_2} \delta(\mathbb{T} - \mathbb{U}) + \delta(\mathbb{W}^a + \mathbb{W}^{nc}) dt = 0.} \tag{5.15}$$

This yields

$$\rho A\ddot{v} + C_b\dot{v} + EI_z v'''' = M_z'' - \rho A\ddot{v}_b, \tag{5.16a}$$

$$\rho\kappa^2\ddot{\psi} + C_t\dot{\psi} - GJ\psi'' = T', \tag{5.16b}$$

$$v(0,t^*) = v'(0,t^*) = 0, \tag{5.17a}$$

$$m_t\ddot{v}(L,t^*) + m_t o_x \ddot{v}'(L,t^*) + m_t o_z \ddot{\psi}(L,t^*) - EI_z v'''(L,t^*) = 0, \tag{5.17b}$$

$$\begin{aligned} &m_t o_x \ddot{v}(L,t^*) + (I_{33} + m_t(o_x^2 + o_y^2))\ddot{v}'(L,t^*) + (I_{13} + m_t o_x o_z)\ddot{\psi}(L,t^*) \\ &+ EI_z v''(L,t^*) = 0, \end{aligned} \tag{5.17c}$$

$$\psi(0,t^*) = 0, \tag{5.17d}$$

$$\begin{aligned} &m_t o_z \ddot{v}(L,t^*) + (I_{13} + m_t o_x o_z)\ddot{v}'(L,t^*) + (I_{11} + m_t(o_y^2 + o_z^2))\ddot{\psi}(L,t^*) \\ &+ GJ\psi'(L,t^*) = -m_t g o_y. \end{aligned} \tag{5.17e}$$

Note that the resulting system dynamics are coupled only through the boundary conditions at the free end. To homogenize the last boundary condition, Equation 5.17e,

we introduce the following:

$$\gamma(x,t^*) = \psi(x,t^*) + \frac{m_t g}{GJ} o_y x. \tag{5.18}$$

This yield the following homogeneous boundary conditions:

$$v(0,t^*) = v'(0,t^*) = 0, \tag{5.19a}$$

$$m_t\ddot{v}(L,t^*) + m_t o_x \ddot{v}'(L,t^*) + m_t o_z \ddot{\gamma}(L,t^*) - EI_z v'''(L,t^*) = 0, \tag{5.19b}$$

$$\begin{aligned} &m_t o_x \ddot{v}(L,t^*) + (I_{33} + m_t(o_x^2 + o_y^2))\ddot{v}'(L,t^*) + (I_{13} + m_t o_x o_z)\ddot{\gamma}(L,t^*) \\ &+ EI_z v''(L,t^*) = 0, \end{aligned} \tag{5.19c}$$

$$\gamma(0,t^*) = 0, \tag{5.19d}$$

$$\begin{aligned} &m_t o_z \ddot{v}(L,t^*) + (I_{13} + m_t o_x o_z)\ddot{v}'(L,t^*) + (I_{11} + m_t(o_y^2 + o_z^2))\ddot{\gamma}(L,t^*) \\ &+ GJ\gamma'(L,t^*) = 0. \end{aligned} \tag{5.19e}$$

5.3 Mode Shapes and The Frequency Equation

For simplicity, we introduce the following set of scaling parameters

$$\begin{cases} \zeta := \frac{x}{L}, \quad w := \frac{v}{L}, \quad w_b := \frac{v_b}{L}, \quad a_i := \frac{o_i}{L}, i \in [x,y,z], \\ \lambda_i^4 := \frac{\rho A L^4 \omega_i^2}{EI_z}, \quad \mathcal{X}^2 := \frac{EI_z}{GJ}, \quad \mu^2 := \frac{\kappa^2}{AL^2}, \\ M_t := \frac{m_t}{\rho AL}, \quad \mathcal{I}_{ij} := \frac{I_{ij}}{\rho AL^3} \quad i,j \in [1,2,3], \\ t := t^*\omega_1, \quad \Omega_i := \frac{\omega_i}{\omega_1}, \\ c_b := \frac{C_b}{\rho A \omega_1}, \quad c_t := \frac{C_t}{\rho \kappa^2 \omega_1}, \quad \alpha_1 := \frac{\alpha_1^*}{\rho AL^3\omega_1^2}, \quad \alpha_2 := \frac{\alpha_2^*}{\rho L^2\kappa^2\omega_1^2}, \end{cases} \tag{5.20}$$

where ω_1 is the frequency of the fundamental vibration mode. With these definitions, the resulting partial differential equations and boundary conditions can be re-written

as:

$$\begin{aligned}\ddot{w} + c_b\dot{w} + \frac{\Omega_i^2}{\lambda_i^4}w'''' &= \alpha_1 V_a \cos\beta[H''(\zeta - s_1/L) - H''(\zeta - s_2/L)] - \ddot{w}_b,\\ \ddot{\psi} + c_t\dot{\psi} - \frac{\Omega_i^2}{\mathcal{X}^2\mu^2\lambda_i^4}\psi'' &= \alpha_2 V_a \sin\beta[H'(\zeta - s_1/L) - H'(\zeta - s_2/L)],\end{aligned} \tag{5.21}$$

$$w(0,t) = w'(0,t) = 0, \tag{5.22a}$$

$$\ddot{w}(1,t) + a_x\ddot{w}'(1,t) + a_z\ddot{\gamma}(1,t) - \frac{1}{\lambda_1^4 M_t}w'''(1,t) = 0, \tag{5.22b}$$

$$a_x\ddot{w}(1,t) + \frac{1}{M_t}[\mathcal{I}_{33} + M_t(a_x^2 + a_y^2)]\ddot{w}'(1,t) + \frac{1}{M_t}[\mathcal{I}_{13} + M_t a_x a_z]\ddot{\gamma}(1,t) + \frac{1}{\lambda_1^4}w''(1,t) = 0, \tag{5.22c}$$

$$\gamma(0,t) = 0, \tag{5.22d}$$

$$a_z\ddot{w}(1,t) + \frac{1}{M_t}[\mathcal{I}_{13} + M_t a_x a_z]\ddot{w}'(1,t) + \frac{1}{M_t}[\mathcal{I}_{11} + M_t(a_y^2 + a_z^2)]\ddot{\gamma}(1,t) + \frac{1}{\lambda_1^4\mathcal{X}^2}\gamma'(1,t) = 0. \tag{5.22e}$$

Now, the primes represent derivatives with respect to the spatial variole ζ and the dots represent derivatives with respect to the temporal variable t. To find the system's characteristic equation and the associated mode shapes, we solve the unforced undamped eigenvalue problem associated with Equations (5.21)- (5.22e). To that end, we express the beam's deflection and rotation angle in terms of the following sparable solutions:

$$w(\zeta,t) = V(\zeta)e^{\imath\omega_i t}, \quad \text{and} \quad \gamma(\zeta,t) = \Gamma(\zeta)e^{\imath\omega_i t}, \tag{5.23}$$

where $V(\zeta)$ and $\Gamma(\zeta)$ are the mode shapes associated with the flexural and torsional motions, respectively. Substituting Equation (5.23) back into Equations (5.21-5.22e) yields

$$V'''' - \lambda_i^4 V = 0, \tag{5.24a}$$

$$\Gamma'' + \lambda_i^4\mu^2\mathcal{X}^2\Gamma = 0, \tag{5.24b}$$

$$V(0) = V'(0) = 0, \tag{5.25a}$$

$$\lambda_i^4 M_t[V(1) + a_x V'(1) + a_z \Gamma(1)] + V'''(1) = 0, \tag{5.25b}$$

$$\lambda_i^4 \left[M_t a_x V(1) + [\mathcal{I}_{33} + M_t(a_x^2 + a_y^2)]V'(1) + [\mathcal{I}_{13} + M_t a_x a_z]\Gamma(1)\right] - V''(1) = 0, \tag{5.25c}$$

$$\Gamma(0) = 0, \tag{5.25d}$$

$$\mathcal{X}^2 \lambda_i^4 \left[M_t a_z V(1) + [\mathcal{I}_{11} + M_t(a_y^2 + a_z^2)]\Gamma(1) + [\mathcal{I}_{13} + M_t a_x a_z]V'(1)\right] - \Gamma'(1) = 0. \tag{5.25e}$$

The solution of Equations (5.24a) and (5.24b) subjected to the boundary conditions (5.25a) and (5.25d) takes the form

$$V(\zeta) = C_1[\sin(\lambda_i \zeta) - \sinh(\lambda_i \zeta)] + C_2[\cos(\lambda_i \zeta) - \cosh(\lambda_i \zeta)], \tag{5.26}$$

$$\Gamma(\zeta) = C_3 \sin(\lambda_i^2 \mathcal{X} \mu \zeta). \tag{5.27}$$

Substituting Equations (5.26) and (5.27) back into Equations (5.25b), (5.25c), and (5.25e), we obtain the following eigenvalue problem

$$\mathcal{F}_{3\times 3}\mathcal{C}_{3\times 1} = 0, \quad \mathcal{C} = [C_1 \; C_2 \; C_3]^T. \tag{5.28}$$

For a non-trivial solution of Equation (5.28), we set the determinant of the coefficient matrix equal to zero, $Det(\mathcal{F}) = 0$, this yields a transcendental characteristic equation which can be solved for the infinite eigenvalues, λ_i. Associated with each eigenvalue, an eigenvector $\mathcal{C}_i$ is obtained using Equation (5.28). It is worth noting that with every eigenvalue (frequency), a coupled mode shape consisting of $V(\zeta)$ and $\Gamma(\zeta)$ can be constructed with the relative contribution of both components determined by the associated eigenvector. This eigenfunction are the normalized using

the following orthogonality condition [92]:

$$\begin{aligned}
&\int_0^1 (V_i V_j + \mu^2 \Gamma_i \Gamma_j) d\zeta + M_t V_i(1) V_j(1) + \mathcal{I}_{11t} \Gamma_i(1) \Gamma_j(1) \\
&+ M_t a_x (V_i'(1) V_j(1) + V_i(1) V_j'(1)) + \mathcal{I}_{33t} V_i'(1) V_j'(1) \\
&+ M_t a_z (V_i(1) \Gamma_j(1) + \Gamma_i(1) V_j(1)) + \mathcal{I}_{13t} (V_i'(1) \Gamma_j(1) + \Gamma_i(1) V_j'(1)) = \delta_{ij},
\end{aligned} \tag{5.29}$$

5.4 Model Validation

To validate the theoretical model and the resulting frequency equation, we considered two cantilever beams with two rigid bodies as listed in Tables 5.1 and 5.2. The first three modal frequencies were obtained experimentally by subjecting the system to a coupled torsion-bending initial conditions at the beam tip, then recording the fast fourier transform (FFT) of the resulting time history. For the purpose of verification, the experiment was also repeated by subjecting the beam to a chirp base-acceleration signal spanning the range between 1 and 200 Hz. The base acceleration was supplied to the beam through an electrodynamic shaker as depicted in Fig. 5.4. The peak frequencies in the FFT spectrum and the chirp response were averaged and recorded in Table 5.4. The frequency equation is then solved numerically for the parameters listed in Table 5.1 and 5.2 and the results are compared in Table 5.4.

In general, there is a good agreement between the theoretical and experimental results in the three cases considered. Visual inspection of the mode shapes during the experimental testing, revealed that the first coupled mode is dominated by a bending component which is essentially associated with the first bending mode of a cantilever beam. The second coupled mode shape is dominated by a bending component associated with the second bending mode of the beam. However, in this case, torsional oscillations were more prevalent. The third mode was observed

Table 5.1: Geometric and material properties of the beam and tip mass (refer to Fig. 5.3).

Property	**Beam I: Steel**	**Beam II: Steel**
Modulus of elasticity, $E[GPa]$	200	210
Density, $\rho[kg/m^3]$	7500	7500
Length, $l[mm]$	270	250
Width, $w[mm]$	24.8	19.05
Thickness, $t_b[mm]$	0.7366	0.4445

Table 5.2: Geometric and material properties of the rigid body (refer to Fig. 5.3).

Property	Rigid Body I	Rigid Body II
Density, $\rho_t[Kg/m^3]$	7550	7550
Diameter, $D[mm]$	15.875	6.350
Height, $h_1[mm]$	3.099	25.4
Height, $h_2[mm]$	18.923	25.4

Table 5.3: Geometric and material properties of the piezoelectric actuator.

MFC (MFC M8528)	
Electromechanical coupling coefficient, $d_{31}[m/V]$	-210×10^{-12}
Modulus of elasticity, $E[GPa]$	30
Thickness, $t_a[mm]$	0.3
Length, $s_2 - s_1[mm]$	84
Width, $b[mm]$	24
piezoelectric actuator start point, $s_1[mm]$	20
piezoelectric actuator end point, $s_2[mm]$	104
position measurement point, $s_3[mm]$	260

to be torsion dominated (first torsional mode of a cantilever beam) with a small second-mode bending component. These results agree with the theoretical findings of the mode shapes shown in Figs. 5.5, 5.6 and 5.7 for the two beams and two rigid bodies considered. Indeed, similar to what is observed experimentally, the first and the second coupled mode shapes are bending dominated in the three cases. On the other hand, the third mode shape is torsion dominated.

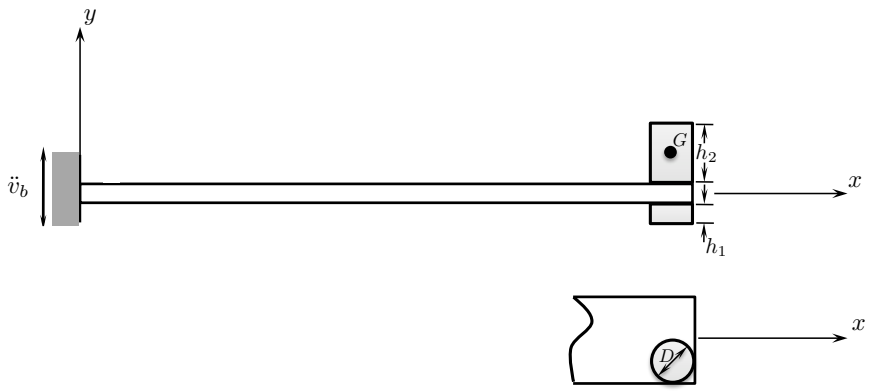

Figure 5.3: Schematic of the beam and rigid body used in the experiments.

Table 5.4: Comparison of the first three theoretical and experimental modal frequencies of the beam.

	Experimental Freq. [Hz]	Analytical Freq. [Hz]	Error [%]
Beam I–Rigid Body I	4.2	4.5	6.7
	39.4	39.4	0.0
	59.0	60.6	2.6
Beam II–Rigid Body I	2.1	2.06	1.9
	25.5	27.25	6.4
	33.8	35.92	5.9
Beam II–Rigid Body II	3.0	3.0	0.0
	25.9	28.7	9.8
	37.1	36.6	1.4

5.5 Reduced-Order Model

To implement the control algorithm, we discretize the system of PDEs into a finite set of coupled linear ODEs using the following Galerkin expansion:

$$v(\zeta,t)=\sum_{i=1}^{m}V_i(\zeta)q_i(t),\quad \gamma(\zeta,t)=\sum_{i=1}^{m}\Gamma_i(\zeta)q_i(t), \tag{5.30}$$

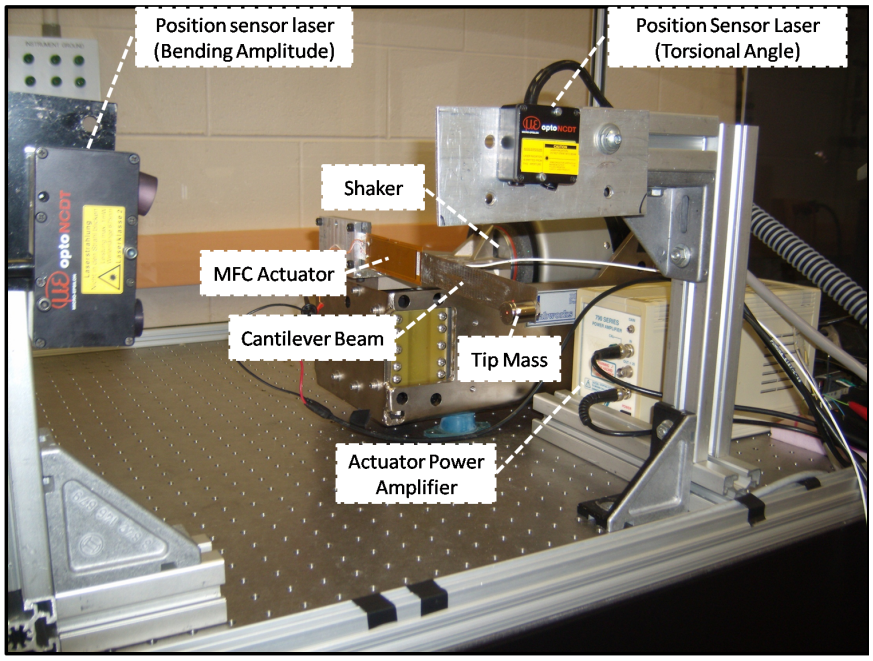

Figure 5.4: Experimental setup of the tip-loaded cantilever beam.

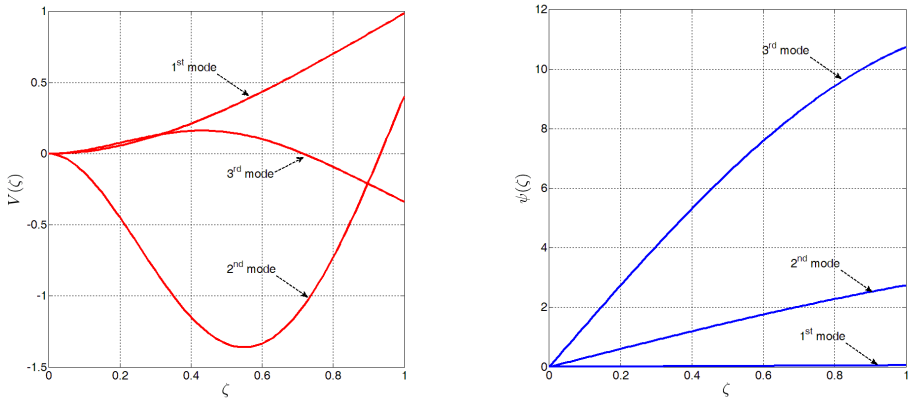

(a) (b)

Figure 5.5: The first three mode shapes of Beam I–Rigid Body I. a) flexural component of the mode shape, and b) torsional component of the mode shape.

where $V_i(\zeta)$ and $\Gamma_i(\zeta)$ are the flexural and torsional components of the mode shapes obtained in the previous section, $q_i(t)$ are generalized temporal coordinates, and m is the number of modes kept in the series expansion. To obtain a reduced-order model

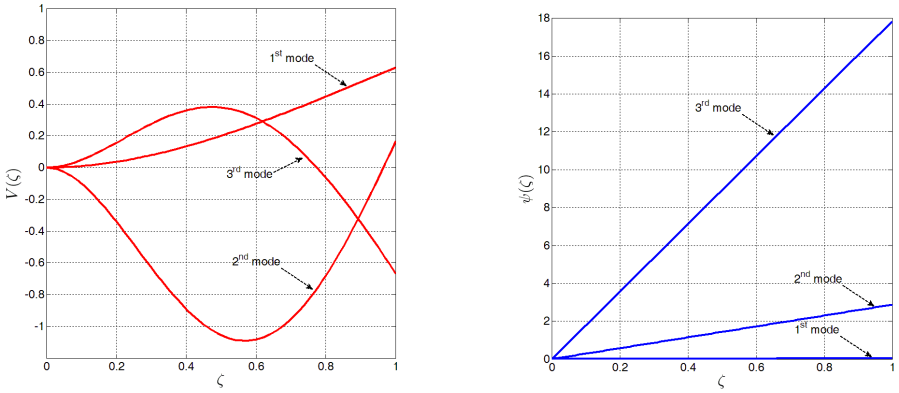

(a) (b)

Figure 5.6: The first three mode shapes of Beam II–Rigid Body I. a) flexural component of the mode shape, and b) torsional component of the mode shape.

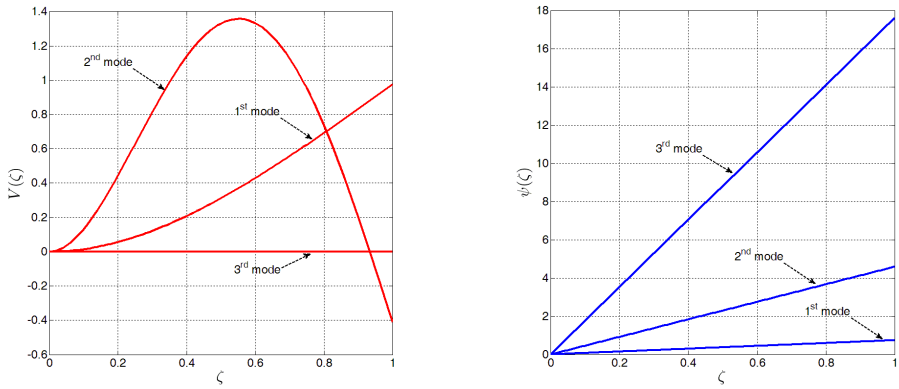

(a) (b)

Figure 5.7: The first three mode shapes of Beam II–Rigid Body II. a) flexural component of the mode shape, and b) torsional component of the mode shape.

of the system, we substitute Equation (5.30) into Equations (5.21), and obtain

$$\sum_{i=1}^{m}\left(V_i\ddot{q}_i + c_b V_i\dot{q}_i + \frac{\Omega_i^2}{\lambda_i^4}V_i''''q_i\right) = \alpha_1 V_a[H''(\zeta - s_1/L) - H''(\zeta - s_2/L)]\cos\beta - \ddot{w}_b, \tag{5.31}$$

$$\sum_{i=1}^{m}\left(\Gamma_i\ddot{q}_i + c_t\Gamma_i\dot{q}_i - \frac{\Omega_i^2}{\mathcal{X}^2\mu^2\lambda_i^4}\Gamma_i''q_i\right) = \alpha_2 V_a[H'(\zeta - s_1/L) - H'(\zeta - s_2/L)]\sin\beta, \quad (5.32)$$

Pre-multiplying Equation (5.31) by V_j and Equation (5.32) by Γ_j, integrating over the length of the domain, and adding the resulting equations, yields

$$\begin{aligned}
&\sum_{i=1}^{m}\left(\int_0^1 (V_jV_i + \Gamma_j\Gamma_i)d\zeta\ddot{q}_i + \int_0^1 (c_bV_jV_i + c_t\Gamma_j\Gamma_i)d\zeta\dot{q}_i + \frac{\Omega_i^2}{\lambda_i^4}\int_0^1 (V_jV_i'''' - \frac{1}{\mathcal{X}^2\mu^2}\Gamma_j\Gamma_i'')d\zeta q_i\right)\\
&= \alpha_1 V_a\cos\beta\int_0^1 V_j[H''(\zeta - s_1/L) - H''(\zeta - s_2/L)]d\zeta\\
&+ \alpha_2 V_a\sin\beta\int_0^1 \Gamma_j[H'(\zeta - s_1/L) - H'(\zeta - s_2/L)]d\zeta - \ddot{w}_b\int_0^1 V_j d\zeta.
\end{aligned}$$

Using the following integral simplifications

$$\int_0^1 V_jV_i''''d\zeta = \lambda_i^4\int_0^1 V_jV_i d\zeta, \qquad \int_0^1 \Gamma_j\Gamma_i''d\zeta = -\lambda_i^4\mathcal{X}^2\mu^2\int_0^1 \Gamma_j\Gamma_i d\zeta, \quad (5.33)$$

and rearranging, we obtain in matrix form

$$\begin{aligned}
\mathbf{M}\ddot{\mathbf{q}} + \mathbf{C}\dot{\mathbf{q}} + \mathbf{K}\mathbf{q} &= \alpha_1 V_a\cos\beta[\mathbf{V}'(s_2/L) - \mathbf{V}'(s_1/L)]\\
&\quad + \alpha_2 V_a\sin\beta[\mathbf{\Gamma}(s_2/L) - \mathbf{\Gamma}(s_1/L)] - \mathbf{f}\ddot{w}_b.
\end{aligned} \quad (5.34)$$

Here, $\mathbf{q}$ is an $m \times 1$ vector representing the systems temporal evolution; $\mathbf{M}$, $\mathbf{C}$, and $\mathbf{K}$ are fully-populated $m \times m$ inertia, damping, and stiffness matrices, and $\mathbf{f}$ is a $m \times 1$ vector characterizing the projection of the base excitation onto the different

vibration modes. The element of these matrices are given by

$$
\begin{aligned}
M_{ij} &= \int_0^1 (V_j V_i + \Gamma_j \Gamma_i) d\zeta, \\
C_{ij} &= c_b \int_0^1 V_j V_i d\zeta + c_t \int_0^1 \Gamma_j \Gamma_i d\zeta, \\
K_{ij} &= \Omega_i^2 \int_0^1 (V_j V_i + \Gamma_j \Gamma_i) d\zeta, \\
f_i &= \int_0^1 V_i d\zeta.
\end{aligned}
\tag{5.35}
$$

Additionally, $\mathbf{V}' = [V_1' \; V_2' \; \ldots \; V_m']^T$, $\mathbf{\Gamma} = [\Gamma_1 \; \Gamma_2 \; \ldots \; \Gamma_m]^T$ are $m \times 1$ vectors.

Figure 5.8 depicts time histories of the free tip response to an initial condition as the number of modes is increased. Because of the linear coupling between the modes, the addition of more modes in the Galerkin expansion has a clear influence on the response behavior, especially the flexural component. For bending, seven modes were kept in the series before the addition of any more modes did not have a clear influence on the time history. For torsion, seven modes were also necessary to converge to the actual response. As such, unlike the case where the beam's dynamics consist only of flexural motions and the discretized system yields a linearly-decoupled system of equations where the higher modes can be safely neglected unless they are directly excited; higher modes in this scenario seem to have a clear influence on the response. As such, extreme care should be taken in the process of neglecting the higher vibration modes.

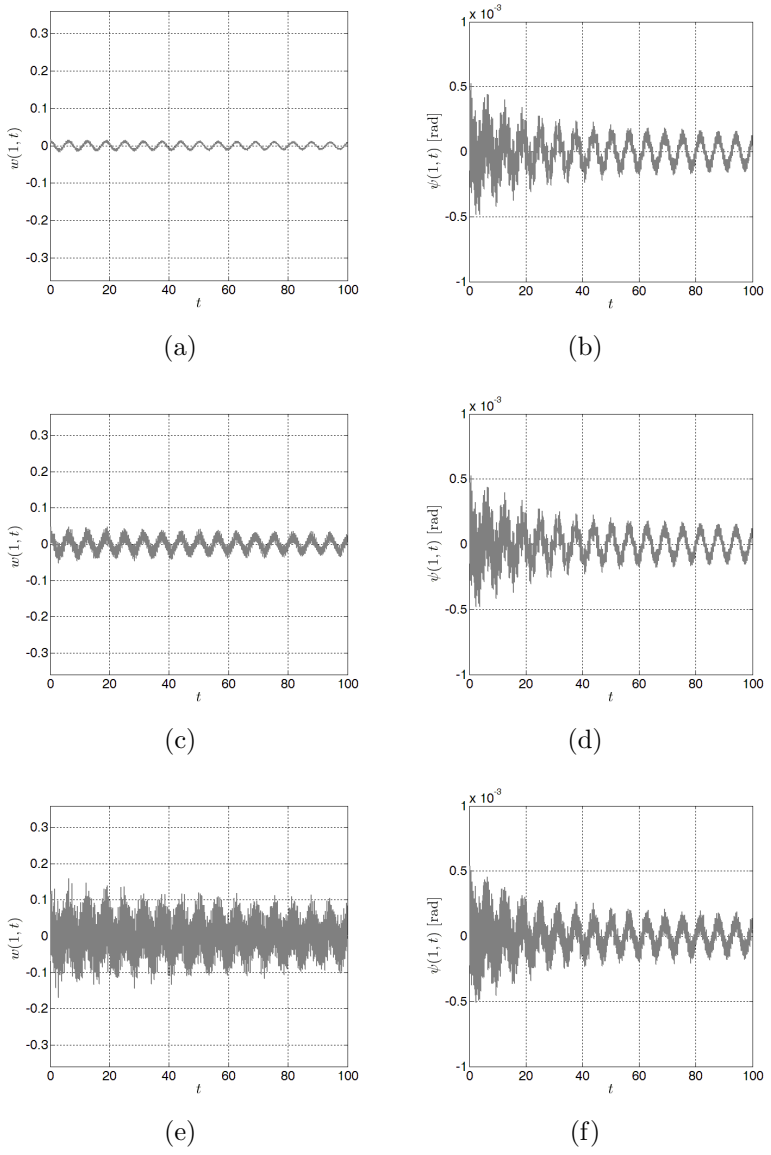

Figure 5.8: Time histories of the beam's tip response (Beam II–Rigid Body I) to an initial condition ($q_1(0) = 0.001$) (a, b) three-mode reduced-order model; (c, d) five-mode reduced-order model; and (e, f) seven-mode reduced-order model.

5.6 Delayed-Position Feedback:

To suppress the linearly-coupled multi-modal dynamic responses of the beam, we consider a delayed-position feedback controller that measures and feeds back a combination of the beam's deflection and torsion. Experimentally, the vertical deflection at a point located on the neutral axis as well as the torsional angle of the beam at a distance s_3 are measured using two laser sensors, then delayed in time and fedback to the piezoelectric actuators, see Fig. 5.4 for the actual experimental setup. The feedback signal takes the form

$$y_f(t) = k_{s1} w(s_3/L, t) + k_{s2} \gamma(s_3/L, t) = (k_{s1} \mathbf{V}^T(s_3/L) + k_{s2} \mathbf{\Gamma}^T(s_3/L))\mathbf{q}, \quad (5.36)$$

where k_{s1} and k_{s2} are the gains of the sensors. To reject the effect of the higher modes and eliminate the effect of noise, the feedback signal is filtered using a Butterworth low-pass filter (BLPF). The filtered signal, y_1 can be related to the sensors signal, y_f via

$$b_k \epsilon^k y_1^{(k)} + b_{k-1} \epsilon^{k-1} y_1^{(k-1)} + ... + b_1 \epsilon \dot{y}_1 + b_0 y_1 = y_f(t), \quad (5.37)$$

where k is the order of the filter, b_k are constants that can be obtained using Equations (3.4a and 3.4b) in Chapter 3, $\epsilon = \omega_1/\omega_{cf}$, and ω_{cf} is the cut-off frequency of the filter. The controller's actuation voltage is obtained when the filtered signal is amplified by a proper gain, delayed by a proper delay, and then supplied to the piezoelectric actuator as an input voltage which can be written as

$$V_a = -K y_1(t - \tau), \quad (5.38)$$

where τ is a non-dimensional time delay, $\tau := \tau^* \omega_1$. Substituting Equations (5.37) and (5.38) into Equation (5.34), we obtain in state-space matrix form

$$\frac{d\mathbf{p}}{dt} = \mathbf{A}\mathbf{p} + \mathbf{A}_d \mathbf{p}(t - \tau), \quad (5.39)$$

where $\mathbf{p} = [q_1\ q_2 \dots q_m\ \dot{q}_1\ \dot{q}_2 \dots \dot{q}_m\ y_{11}\ y_{12} \dots y_{1k}]$, $y_{1k} = y_1^{(k-1)}$, and $\mathbf{A}$ and $\mathbf{A}_d$ are $2m + k \times 2m + k$ matrices given by

$$\mathbf{A} = \begin{bmatrix} 0_{m\times m} & \mathbf{I}_{m\times m} & 0_{m\times k} \\ -\mathbf{M}^{-1}\mathbf{K}_{m\times m} & -\mathbf{M}^{-1}\mathbf{C}_{m\times m} & 0_{m\times k} \\ 0_{k-1\times m} & 0_{k-1\times m} & \mathbf{I}_{k-1\times k} \\ \frac{1}{b_k\epsilon^k}(k_{s1}\mathbf{V}^T(s_3) + k_{s2}\mathbf{\Gamma}^T(s_3))_{1\times m} & 0_{1\times m} & \mathbf{F}_{1\times k} \end{bmatrix}, \quad \text{and} \tag{5.40}$$

$$\mathbf{A}_d = \begin{bmatrix} 0_{m\times m} & 0_{m\times m} & 0_{m\times 1} & 0_{m\times k-1} \\ 0_{m\times m} & 0_{m\times m} & \mathbf{LL}_{m\times 1} & 0_{m\times k-1} \\ 0_{k\times m} & 0_{k\times m} & 0_{k\times 1} & 0_{k\times k-1}. \end{bmatrix}$$

Here, $\mathbf{F} = [-b_0/(b_k\epsilon^k)\ -b_1/(b_k\epsilon^{k-1})\ \dots\ -b_{k-1}/(b_k\epsilon)]$, and

$$\mathbf{LL} = -\alpha_1 K \cos\beta \mathbf{M}^{-1}[\mathbf{V}'(s_1/L) - \mathbf{V}'(s_2/L)] - \alpha_2 K \sin\beta \mathbf{M}^{-1}[\mathbf{\Gamma}(s_1/L) - \mathbf{\Gamma}(s_2/L)].$$

5.7 Linear Stability Analysis:

To assess the stability of the closed-loop system in the gain-delay space, we implement the numerical scheme explained earlier in Section (2.2.3) in which the DDEs of Equation (5.39) are transformed into an equivalent PDE. The PDE is then discretized into a set of ODEs in the delay space using the method of lines. To that end, we substitute Equation (5.39) into Equation (2.25), then find the eigenvalues of the resulting matrix $\mathcal{A}_N$ which represent the eigenvalues of the closed-loop system for a given K and τ. Obviously, in this approximation scheme, the number of eigenvalues is finite and increases as the number of lines considered in the discretization of the equivalent PDE is increased. Furthermore, the closeness of the resulting eigenvalues to the actual eigenvalues increases with the number of ODEs resulting from the discretization of the equivalent PDE.

To illustrate these facts, we consider a three-mode reduced-order model of the beam

dynamics. In other words, m is chosen to be equal to three in Equation (5.39). We also choose a first-order BLPF filter with $\epsilon = 50$ and only include flexural feedback, the piezoelectric parameters listed in Table 5.3. The number of lines in the discretization of the equivalent system is then increased from $N = 5$ to 10, 20, 40 and the eigenvalues of the matrix in Equation (2.25) are obtained. The process is repeated for values of $-1 \leq K \leq 1$ and $0 < \tau \leq 1$, then the gain-delay space is mapped into stable and unstable regions as depicted in Figs. 5.9(a), 5.9(b), 5.9(c), and 5.9(d). The shaded regions represent stable gain-delay combinations and the resulting contours represent the magnitude of the real part of the eigenvalue closest to the imaginary axis which can be used as a measure of the effective damping of the system for a given controller gain and delay.

When comparing the stability maps shown in Fig. 5.9, it becomes evident that the approximation improves as the number of lines N is increased. When the number of lines used to discretize the equivalent PDE is small, $N = 5$, the stability maps are only accurate for very small delays $\tau < 0.1$, see Fig. 5.9(a). However, as the number of lines is increased to $N = 10$, almost half of the first stability pocket is well approximated. By carrying this convergence analysis for the system at hand, we concluded that at least 40 lines are necessary to accurately predict the first two stability pockets as shown in Fig. 5.9(d). The same convergence study was repeated for higher values of m and k. Again, we found that 40 lines are sufficient to approximate the first two stability pockets.

5.8 Effect of Filters on the Performance of the Controller

In this section, we analyze the influence of the filter's order and cut-off frequency on the stability of the closed-loop system. Towards that end, we generate the sta-

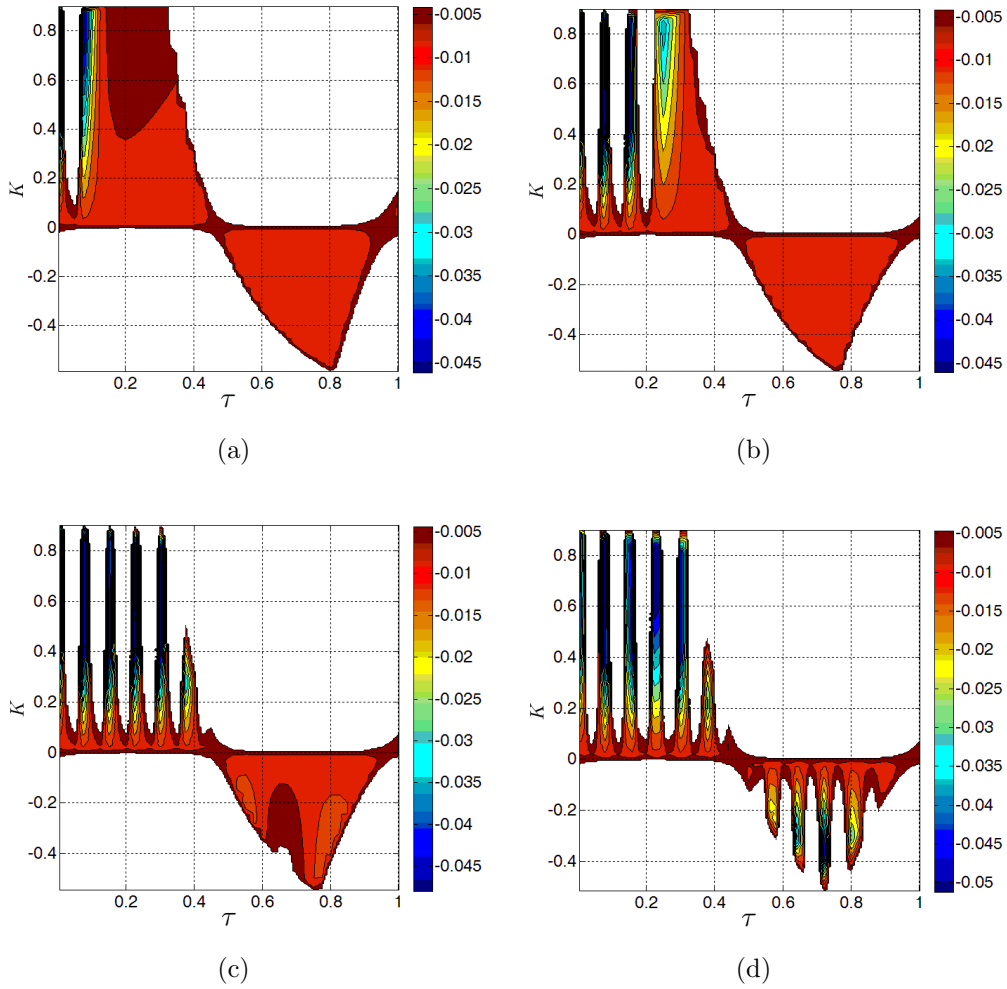

Figure 5.9: Theoretical stability maps using a three-mode reduced-order model of the tip-loaded beam. Results are obtained for Beam II–Rigid body I. (a) Discretization using 5 lines ($N = 5$), (b) discretization using 10 lines ($N = 10$), (c) discretization using 20 lines ($N = 10$), and (d) discretization using 40 lines ($N = 40$).

bility maps for different filter orders and cut-off frequencies as depicted in Fig. 5.10. We limit the analysis to only flexural feedback and use a three-mode reduced-order model to generate the stability pockets. While a higher-order model is expected to produce more accurate predictions, generation of the stability maps is very computationally intensive prompting the inclusion of only the first three modes in the numerical analysis. The effect of the higher modes on the controlled response will

be addressed in Section 5.10.

As can be seen in Fig. 5.10(a), when no filter is implemented, all the vibration modes are permitted into the feedback. This has the adverse influence of shrinking the stability pockets as it becomes very challenging to find a single gain-delay combination that stabilizes all modes simultaneously. Usually, for systems that can be represented by a single-mode approximation, two large stability pockets can be attained between $0 < \tau < 1$ (Note that the delay is normalized with respect to the first modal period, i.e., $0 < \tau^* < T$). The first stability pocket only exists for positive gains and spans the region between $0 < \tau^* < T/2$, while the second exists for negative gains and spans the region between $T/2 < \tau^* < T$. When inspecting Fig. 5.10(a), it becomes evident that the inclusion of the higher modes leads to the generation of about thirteen unstable pockets within these two first pockets. This number is not arbitrary and is resulting from the inclusion of the second mode dynamics which has a frequency that is about thirteen times the frequency of the first mode, see Table 5.5. As the gain is increased, the width of these unstable pockets increases because of the influence of the third mode. If higher modes are included in the stability analysis, one would expect that the stable regions will shrink even further making it even harder to find a gain-delay combination that stabilizes all modes simultaneously when no filter is included.

When a first-order filter with a cut-off frequency that is five times the first modal frequency is implemented, we notice an increase in the size of the stability pockets, see Fig. 5.10(b). Specifically, we can clearly see that the width of the stable pockets increases especially for large gains. This stems from the rejection of the third mode dynamics from the feedback. Note that, although the cut-off frequency is chosen such that it is smaller than the second modal frequency of the beam, see Table 5.5; we still observe that, within every large pocket of stability, there still exists almost six smaller unstable pockets resulting from the second-mode dynamics passing through the feedback due to the large roll-off slope of the first-order filter. When the cut-off

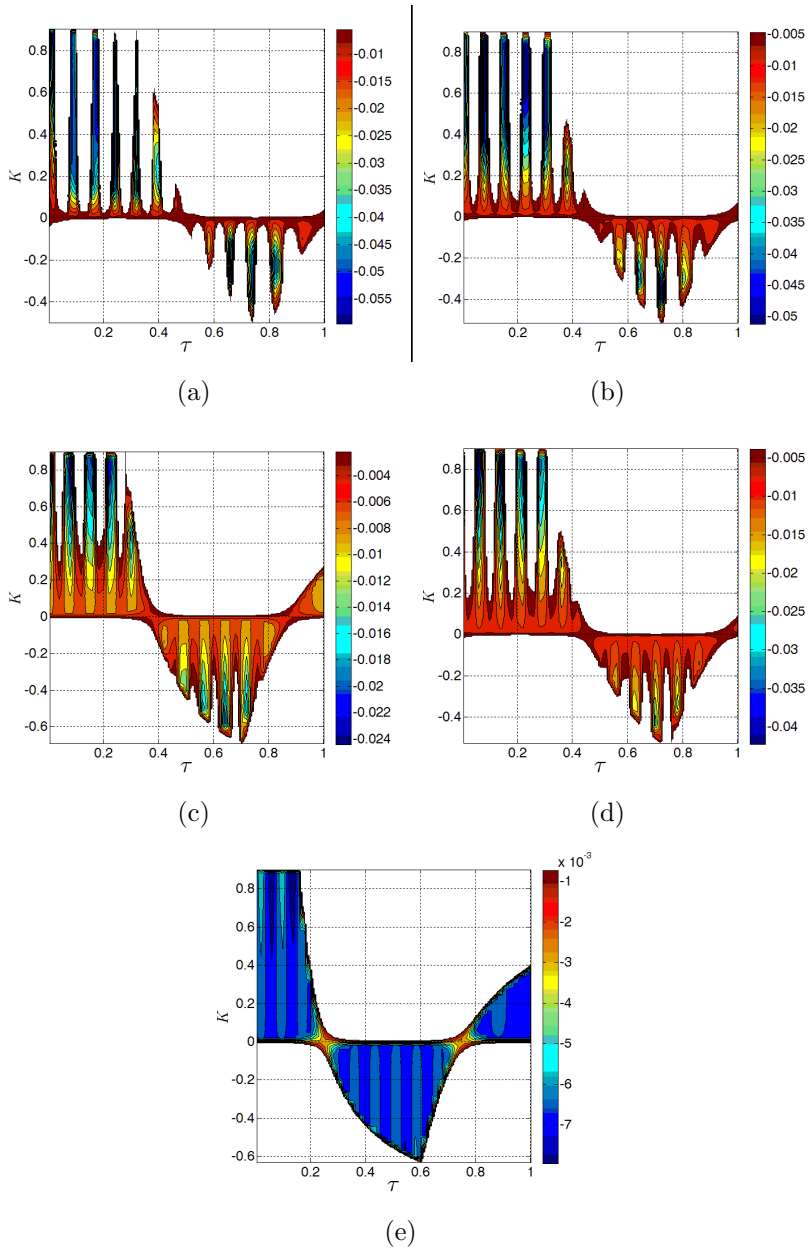

Figure 5.10: Theoretical stability maps using a three-mode reduced-order model. Results are obtained for Beam II–Rigid body I, and $\beta = 0$ using (a) no filter, (b) first-order filter with $\epsilon = 1/5$, (c) first-order filter with $\epsilon = 1$, (d) second-order filter with $\epsilon = 1/5$, and (e) second-order filter with $\epsilon = 1$.

frequency is decreased such that its equal to the first modal frequency, we observe three distinct variations in the stability maps. Firstly, the whole stability diagram

h!

Table 5.5: First five modal frequencies of the beam.

	ω_1 [Hz]	ω_2 [Hz]	ω_3 [Hz]	ω_4 [Hz]	ω_5 [Hz]
Beam II–No rigid body	10.3	64.4	180.4	353.5	584.3
Beam II–Rigid body I	2.06	27.25	35.92	76.34	128.4
Beam II–Rigid body II	3.0	28.7	36.6	87.4	171.4

shifts to the left due to the increased delay introduced by the filter. This has the adverse influence of shrinking the first and larger pocket of stability. Secondly, the smaller unstable pockets resulting from the higher modes shift upwards toward larger gains and outside the first stability pocket. As a result, the controller becomes more robust to variations in its gain and delay. Finally, it is observed that the magnitude of the effective damping within the stability pockets decreases to almost half of its original value making the controller less effective in rejecting external disturbances.

When compared to the first-order filter, a second-order filter has a sharper roll-off slope and is more effective in rejecting the higher modes from the feedback. Figure 5.10(d) illustrates that, when a second-order filter is implemented, the smaller unstable pockets associated with the second mode shift even further toward larger gains increasing the robustness of the controller. However, this comes at the cost of decreasing the effective damping in the system. Indeed, as shown in Fig. 5.10(e), by using a second-order filter and decreasing the cut-off frequency such that it is equal to that of the first mode, one can completely reject the influence of the higher order modes and obtain one large stabilizing pocket. However, it is clear again, that this comes at the expense of the effective damping which is significantly reduced.

These finding can be further demonstrated by inspecting time histories of the beam's tip response to an initial condition as depicted in Figs. 5.11 and 5.12. The beam was perturbed at the tip with a first mode initial condition. Since the first mode is bending dominated, the uncontrolled response is clearly dominated by a bend-

ing component at a frequency equal to the first modal frequency, with the higher modes having lesser influence on the beam's response. However, due to the linear coupling, torsional motion of the beam can still be excited. When compared to the uncontrolled response, it is evident that the controller is capable of suppressing both flexural and torsional oscillations of the beam and significantly enhancing the vibrations settling time.

The effect of the filter on the effectiveness of the controller is deduced by comparing the response settling time and the amplitude of residual oscillations for the same gain-delay combinations. This can be clearly seen by inspecting Figs. 5.11(a)-5.11(f). Since increasing the order of the filter and decreasing its cut-off frequency reduces the effective damping of the controller for the same gain-delay combinations, the controller is clearly more effective in suppressing beam's oscillations for the lower-order filters. However, in a real life scenario, where there are modeling uncertainties, this comes at the expense of the controller's robustness to variations in its parametric gain and delay. In the case of lower-order filters, any small variations of the controller's parameters around their nominal values can destabilize the controller because of the smaller size of the stability pockets in the gain-delay space.

Within each stability pocket, varying the gain and delay can significantly increase or decrease the effective damping introduced by the controller as evident by the color shadings of the damping contours. For instance, when the gain is increased to $K = 0.8$ for the same delay $\tau = 0.02$, the effective damping increases significantly in the case of the first-order filter with $\epsilon = 1/5$, see Fig. 5.10(b). This significantly improves the ability of the controller to reject external disturbances as shown in Figs. 5.12(a) and 5.12(a). However, when ϵ is increased to one, this same gain-delay combination which now lies very close to the stability boundary of the closed-loop system as shown in Fig. 5.10(b) yields little enhancement in the response characteristics of the beam as shown in Figs. 5.12(c) and 5.12(d).

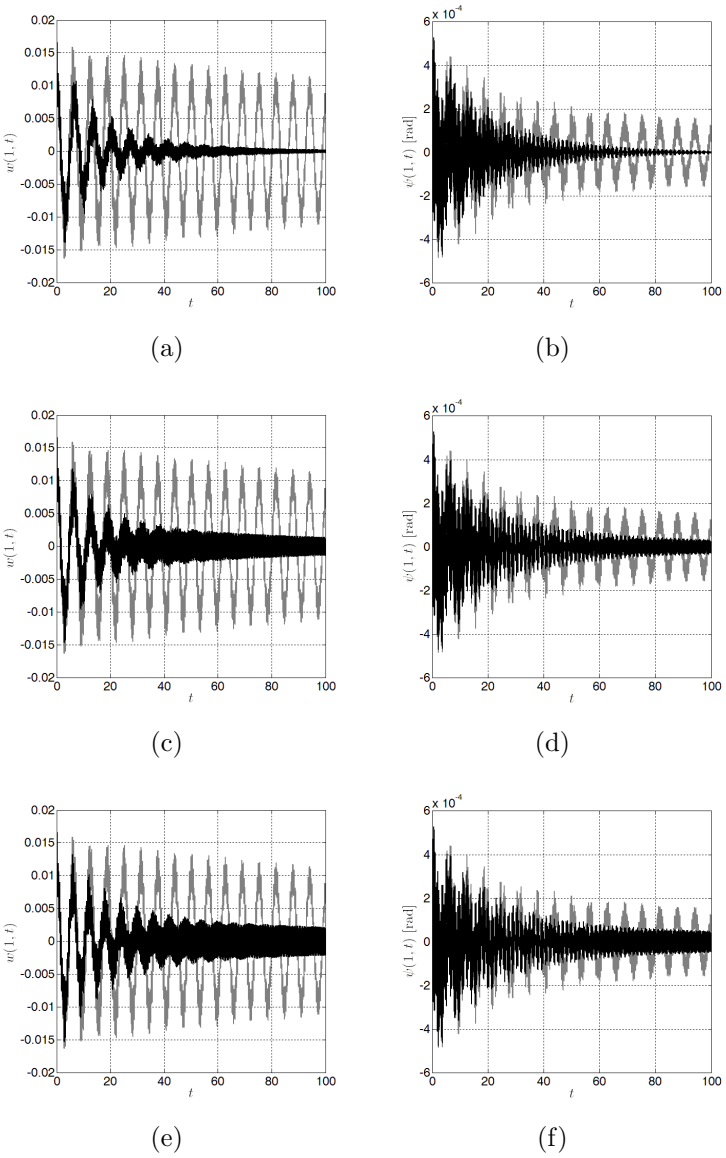

Figure 5.11: Time histories of the beam's (Beam II–Rigid Body I) tip response for an initial condition $q_1 = 0.01$. Uncontrolled (gray line) and controlled (black line). Results are obtained for a gain-delay combination of ($K = 0.2$, $\tau = 0.08$) and (a, b) first-order filter with $\epsilon = 1/5$, (c, d) first-order filter with $\epsilon = 1$; and (e, f) second-order filter with $\epsilon = 1$.

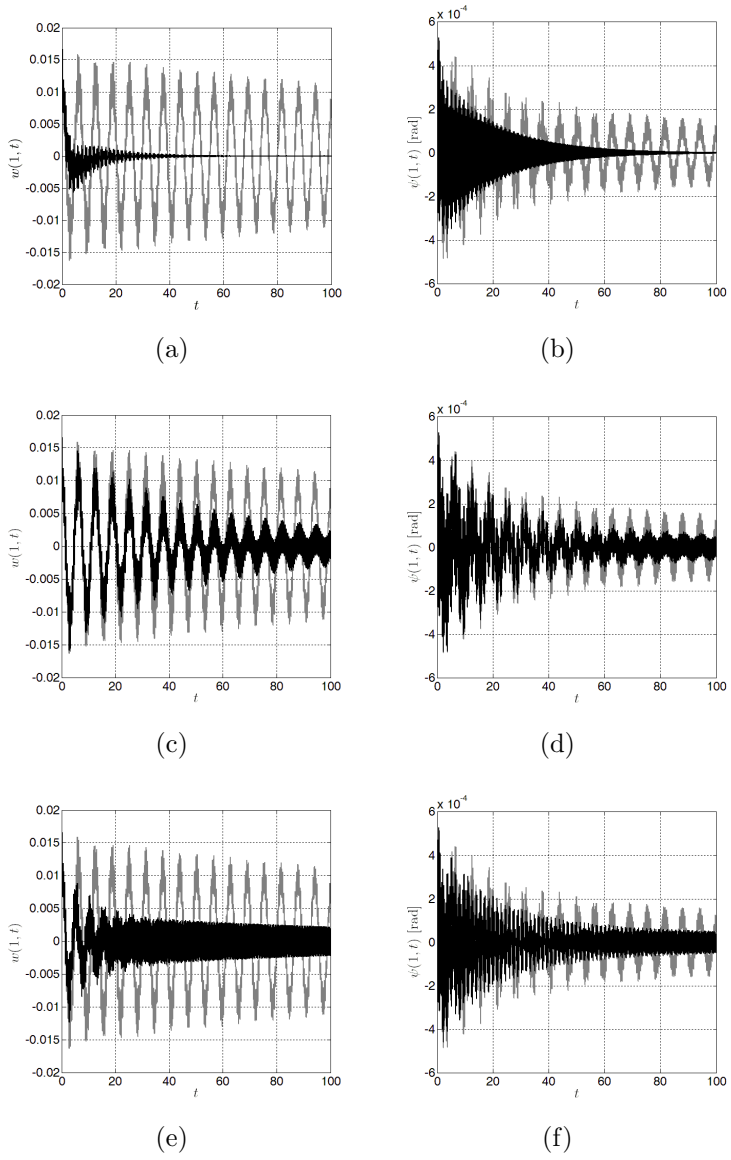

Figure 5.12: Time histories of the beam's (Beam II–Rigid Body I) tip response to an initial condition $q_1 = 0.01$. Uncontrolled (gray line) and controlled (black line). Results are obtained for a gain-delay combination of ($K = 0.8$, $\tau = 0.08$) and (a, b) first-order filter with $\epsilon = 1/5$, (c, d) first-order filter with $\epsilon = 1$; and (e, f) second-order filter with $\epsilon = 1$.

5.9 Influence of the Piezoelectric Patch Orientation on the Performance and Stability of the Controller

Up to this point, we only considered the response of the system to an initial condition in the first mode, i.e., q_1, which is bending dominated. We illustrated that, by using a proper gain-delay combination, the controller is very effective in suppressing the resulting multi-modal oscillations. In this section, we try to investigate the effectiveness of the controller in rejecting oscillations resulting from initial conditions in the higher modes, especially torsional initial conditions. Previous research experiences [104] have indicated that a controller would be most effective in rejecting torsional responses when the piezoelectric patch is oriented at a 45 degree angle with respect to the horizontal axis of the beam ($x - axis$ in this case). To understand how the piezoelectric patch orientation influences the performance of the controller, we generate the stability pockets of the closed-loop system for different orientation angles, β, as shown in Fig. 5.13.

When comparing the stability diagrams at different angles, we observe striking similarities between the stability pockets along the delay axis. The only difference between the resulting diagrams is that the stable regions get stretched along the gain axis. In other words, as the orientation angle is increased from zero, larger controller gains are necessary to destabilize the closed-loop system for the same controller delay. This is expected because, as the angle increases, the controller effort gets distributed among two components, bending and torsion, as can be deduced from Equation (5.34). Since the projection of the controller's input voltage onto the bending component is larger as the orientation angle is increased, the net influence of the controller on the beam decreases, requiring larger controller gains to generate the same effort.

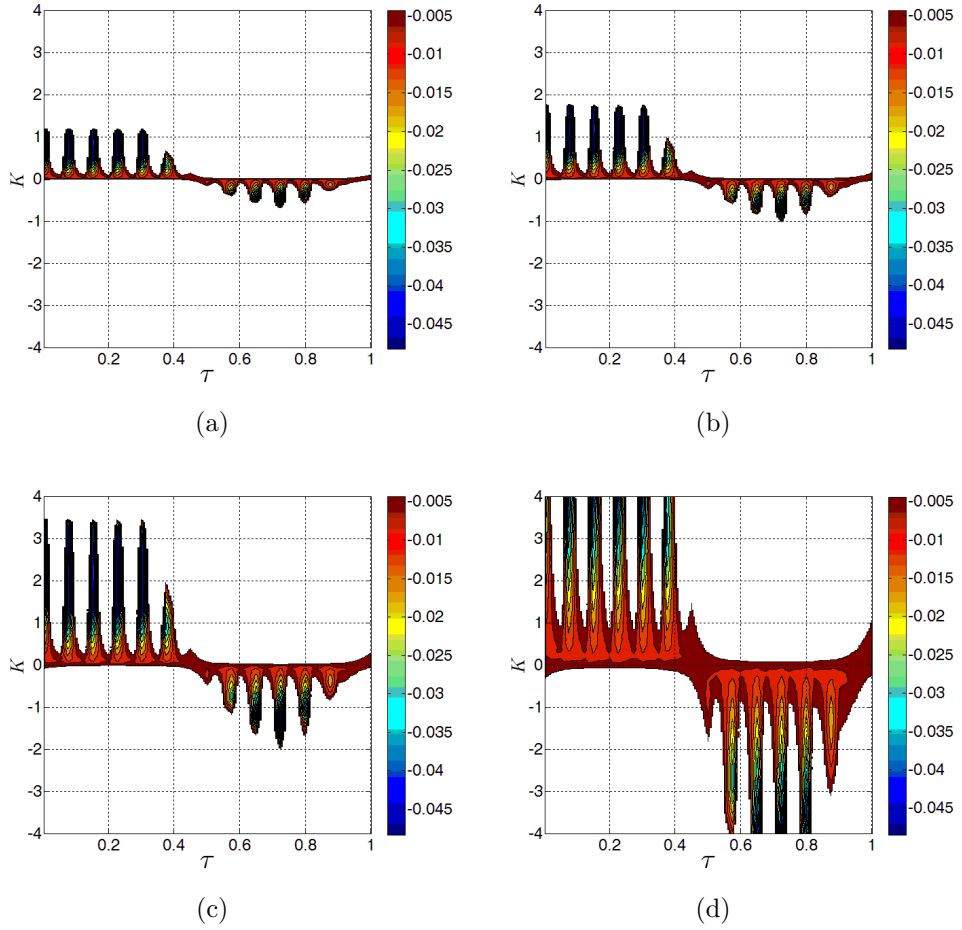

Figure 5.13: Theoretical stability maps using a three-mode reduced-order model of the tip-loaded beam. Results are obtained for Beam II–Rigid body I and (a) $\beta = 30^o$, (b) $\beta = 45^o$, (c) $\beta = 60^o$, and (d) $\beta = 75^o$. A first-order filter with $\epsilon = 1/5$ is implemented in these simulations.

In Figs. 5.14 and 5.15, we simulate the response of the system to an initial condition in the first mode and different patch orientations. The controller gain is increased in each case such that the gain-delay combination produces almost the same amount of maximum effective damping in the closed-loop system. It is evident that the controller is capable of suppressing the beam's oscillations with similar effectiveness using different patch angles as long as the gain is altered in each case to produce the same amount of damping in the system.

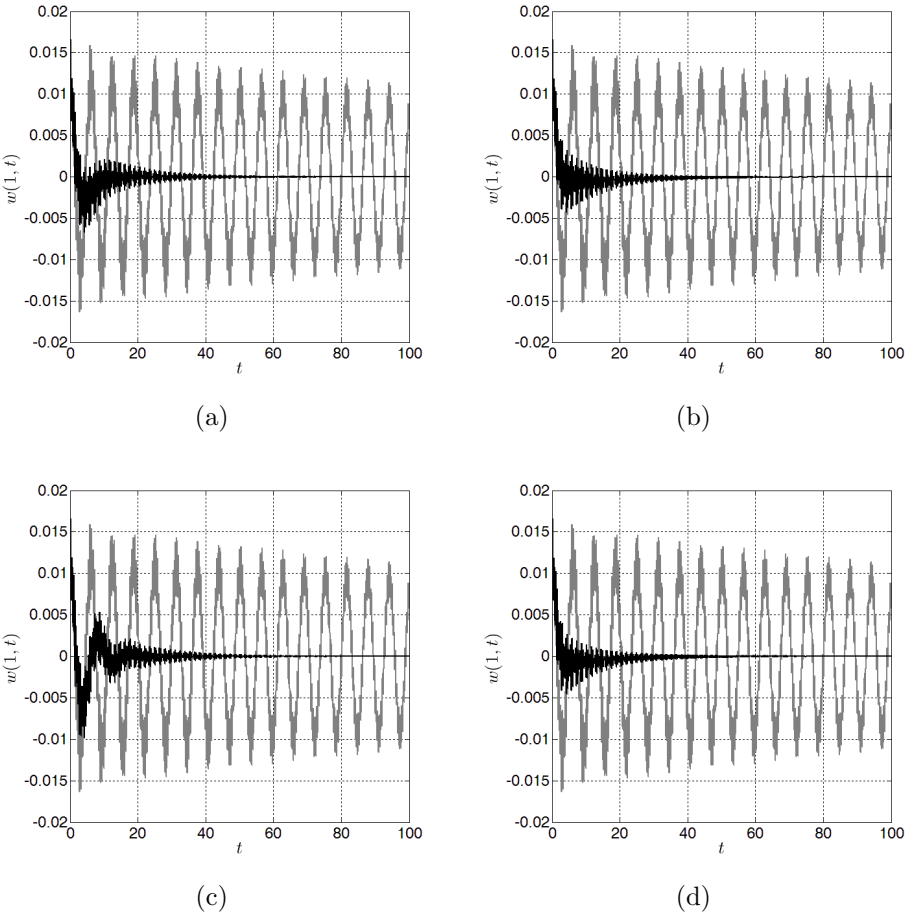

Figure 5.14: Bending time histories of the beam's (Beam II–Rigid Body I) tip response to an initial condition $q_1 = 0.01$. Uncontrolled (gray line) and controlled (black line). Results are obtained for (a) $\beta = 30^o$ and a gain-delay combination $K = 1.0$, $\tau = 0.075$, (b) $\beta = 45^o$ and a gain-delay combination $K = 1.7$, $\tau = 0.075$, (c) $\beta = 60^o$ and a gain-delay combination $K = 2.0$, $\tau = 0.075$, and (d) $\beta = 75^o$ and a gain-delay combination $K = 12.0$,$\tau = 0.075$. A first-order filter with $\epsilon = 1/5$ is implemented in these simulations.

Figure 5.15 investigates the controller's effectiveness in rejecting external disturbances that are not bending dominated and resulting from a combination of initial conditions. The controller is still capable of suppressing beam's oscillations in both bending and torsion but is more effective in controlling the bending component of motion. Even when changing the patch orientation, the performance of the controller remains almost the same provided that the gain is chosen in each case to

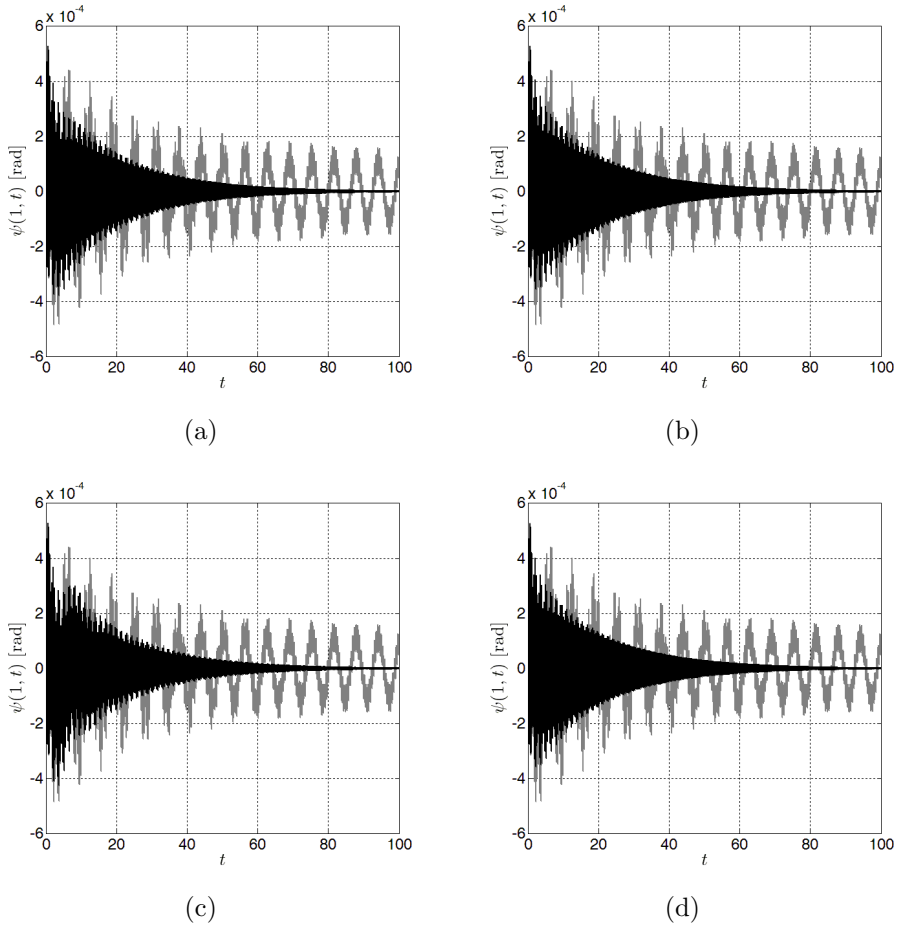

Figure 5.15: Torsion time histories of the beam's (Beam II–Rigid Body I) tip response to an initial condition $q_1 = 0.01$. Uncontrolled (gray line) and controlled (black line). Results are obtained for (a) $\beta = 30^o$ and a gain-delay combination $K = 1.0$, $\tau = 0.075$, (b) $\beta = 45^o$ and a gain-delay combination $K = 1.7$, $\tau = 0.075$, (c) bending response when $\beta = 60^o$ and a gain-delay combination $K = 2.0$, $\tau = 0.075$, and (d) $\beta = 75^o$ and a gain-delay combination $K = 12.0$,$\tau = 0.075$. A first order filter with $\epsilon = 1/5$ is implemented in these simulations.

produce the maximum possible damping. However, when comparing the actuator's input voltage in each scenario, we note that the controller requires less voltage (x-axis) to produce the same output when the patch is oriented at 45^o in reference to the horizontal axis of the beam. This is in agreement with the results of Park and Chopra [104] who illustrated that the piezoelectric patch is most effective in producing torsional moments when it is oriented at or near 45^o.

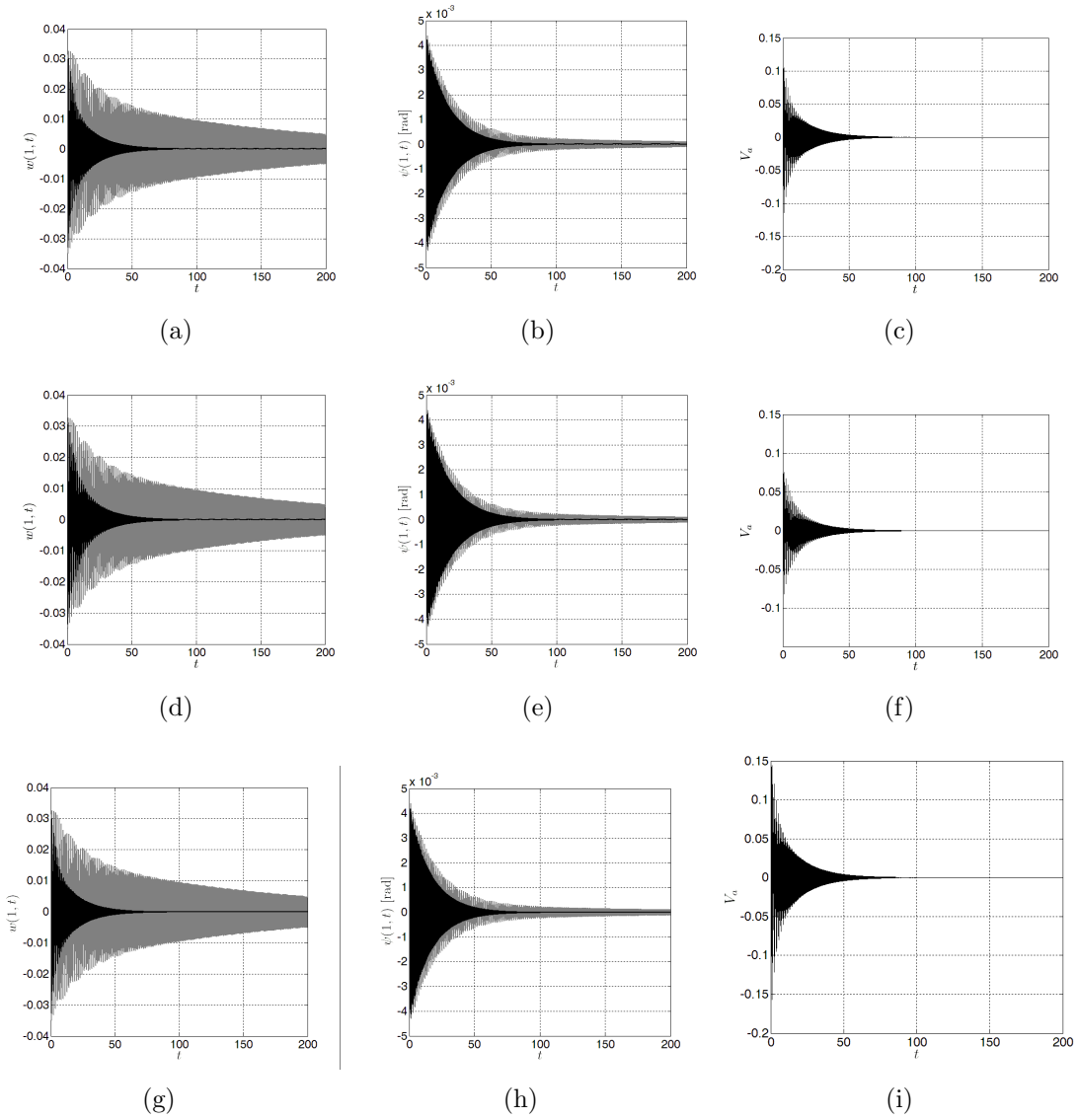

Figure 5.16: Time histories of the beam's (Beam II–Rigid Body I) tip response and controller's input voltage to an initial condition ($q_1 = 0.001$, $q_2 = 0.001$ and $q_3 = 0.0001$). Uncontrolled (gray line) and controlled (black line). Results are obtained for (a, b ,c) $\beta = 0$, $K = 0.8$, and $\tau = 0.02$; (d, e, f) $\beta = 45^o$, $K = 1.7$, and $\tau = 0.02$; and (g, h, i) $\beta = 75^o$, K=10.0, and $\tau = 0.02$.

5.10 Influence of the Higher Modes on the Performance of the Controller

In this section, we investigate the influence of higher modes on the performance of the controller. To that end, we choose a stabilizing gain-delay combination from the stability pockets that are based on the three-mode reduced-order model and use them to simulate the tip response to initial conditions using three-mode and seven-mode reduced-order models as depicted in Figs. 5.17 and 5.18. Results illustrate that the performance of the controller is not significantly altered by the addition of the higher modes. The gain-delay combination remains a stabilizing one with the effectiveness slightly sacrificed as the settling time of the flexural motion is increased. These results are further confirmed in our experimental results presented in section 5.12 which illustrate that gain-delay combinations chosen based on the three-mode reduced-order model are capable of stabilizing the actual infinite-dimensional beam's response.

5.11 Reduction of Beam's Response Amplitude Under Persistent Harmonic Base Excitations

Next, we investigate the effectiveness of the controller in suppressing the response of the beam to harmonic base excitations. To that end, the steady-state frequency response curves are generated near the first three modal frequencies with and without control. Figures 5.19(a) and 5.19(b) depict variation of the steady-state response amplitude, flexural and torsional, near the first modal frequency when the piezoelectric patch is oriented at zero angle. By increasing the effective damping of the system, the controller is capable of significantly reducing the response amplitude over a wide bandwidth of frequencies near the fundamental mode. Furthermore, for

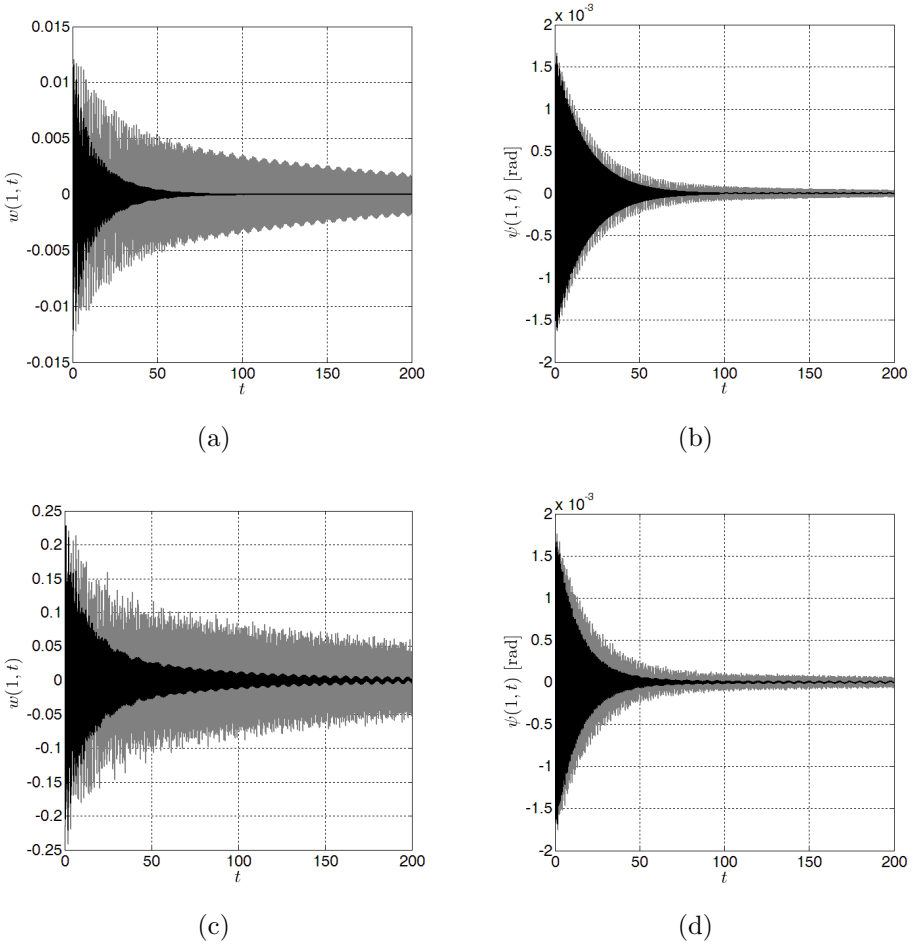

Figure 5.17: Time histories of the beam's (Beam II–Rigid Body I) tip response to initial condition $q_3 = 0.0001$ and $\beta = 45^o$. Uncontrolled (gray line) and controlled (black line). Results are obtained for (a, b) $K = 0.9$ and $\tau = 0.02$ using a three-mode approximation, and (c, d) $K = 0.9$ and $\tau = 0.02$ using a seven-mode approximation.

this gain-delay combination, the controller shifts the first peak frequency to the left toward smaller frequencies. Since, in general, the location of the peak frequency in the frequency spectrum has a periodic dependance on the delay, other values of the controller's parametric delay can shift the peak frequency toward higher frequencies. The influence of the delay on the peak frequency is discussed in significant details in Chapter 4.

The same gain-delay combination can also significantly reduce the response ampli-

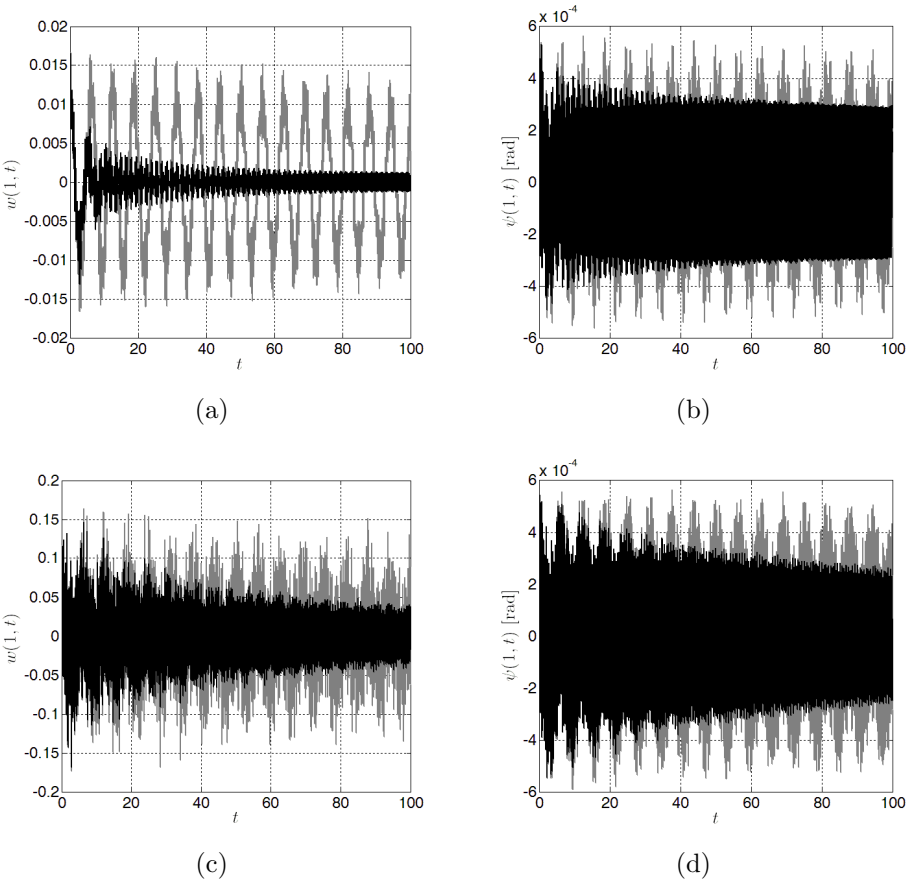

Figure 5.18: Time histories of the beam's (Beam II–Rigid Body I) tip response to initial condition $q_1 = 0.01$ and $\beta = 0^o$. Uncontrolled (gray line) and controlled (black line). Results are obtained for (a, b) $K = 0.5$ and $\tau = 0.25$ using a three-mode approximation, and (c, d) $K = 0.5$ and $\tau = 0.25$ using a seven-mode approximation.

tude near the second modal frequency as depicted in Figs. 5.19(c) and 5.19(d). This constitutes one of the most important characteristics of the controller, which is evidently capable of reducing the response near multiple modes without the need to change the gain-delay combination of the controller. In Figs. 5.19(e) and 5.19(f), the response of the controller is simulated near the third mode, a torsion-dominated mode. Since the base excitation is perpendicular to the axis of the beam along the bending direction, it was difficult to excite large amplitude responses near the third modal frequency using the same levels of input acceleration. As such, we simulated

the response for a base acceleration that is 100 times larger. Simulations shown in Figs. 5.19(e) and 5.19(f) reveal that the same gain-delay combination can actually amplify the response amplitude by reducing the effective damping associated with the third mode. However, the response remains stable and the amplification constant is relatively small.

Next, we repeat the same simulations with the piezoelectric patch oriented at 45^o angle. When compared to the pervious scenario, it is evident in Fig. 5.20 that the controller is now less effective in reducing the amplitude of the response near the first mode. This stems from the fact that, for the same gain-delay combination, the controller produces less damping when the piezoelectric patch is oriented at 45^o as can be seen in Fig. 5.13. On the other hand, orienting the patch at 45^o increases the effectiveness of the controller in mitigating the vibration of the torsional component of the third torsion-dominated mode. This can be attributed to the larger input torque that the patch can provide for the same gain-delay combinations when oriented at 45^o angle.

5.12 Experimental Implementation

Throughout this experimental study, we limit the investigation to only bending feedback and use one piezoelectric patch oriented at zero degree angle (single-input single-output). In Fig. 5.21, we compare the stability diagrams of the controller as obtained experimentally to those obtained theoretically in the previous sections. Two cases are considered using first-order filters with different cut-off frequencies, namely $\epsilon = 0.1$ and $\epsilon = 0.2$. The experimental results are generated by choosing a certain controller delay then increasing the gain slowly until the system loses stability. For every gain-delay combination, the beam is subjected to an initial condition and the response is monitored. If the response dies out and returns to the

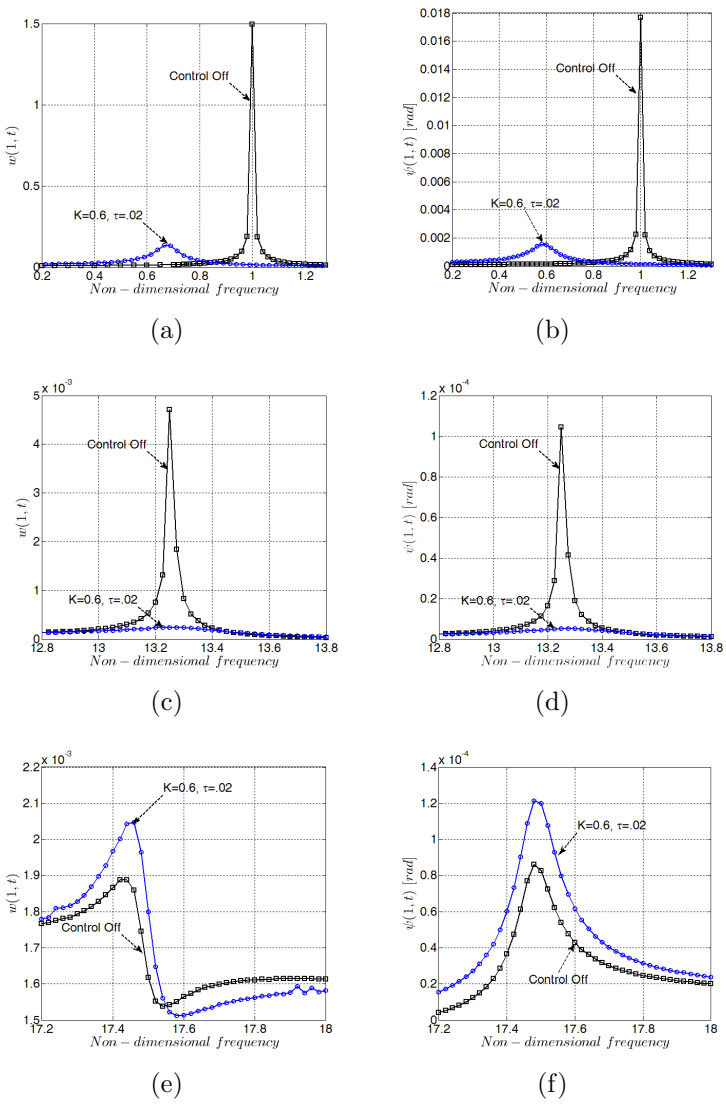

Figure 5.19: Frequency-response curves of the beam's tip (Beam II–Rigid body I). The controller is applied using a first-order filter ($\epsilon = 1/50$) and a piezoelectric patch oriented at $\beta = 0^o$. Results are obtained near (a, b) the first mode using $\ddot{w}_b = 0.1$; (c, d) the second mode using $\ddot{w}_b = 0.1$; and (e, f) the third mode and $\ddot{w}_b = 10.0$.

stable fixed point, then the gain-delay combination is considered stable. Otherwise, if the response grows exponentially to infinity or to a limit cycle then the gain-delay combination is considered linearly unstable. The process in repeated to generate the stability boundaries shown in Fig. 5.21.

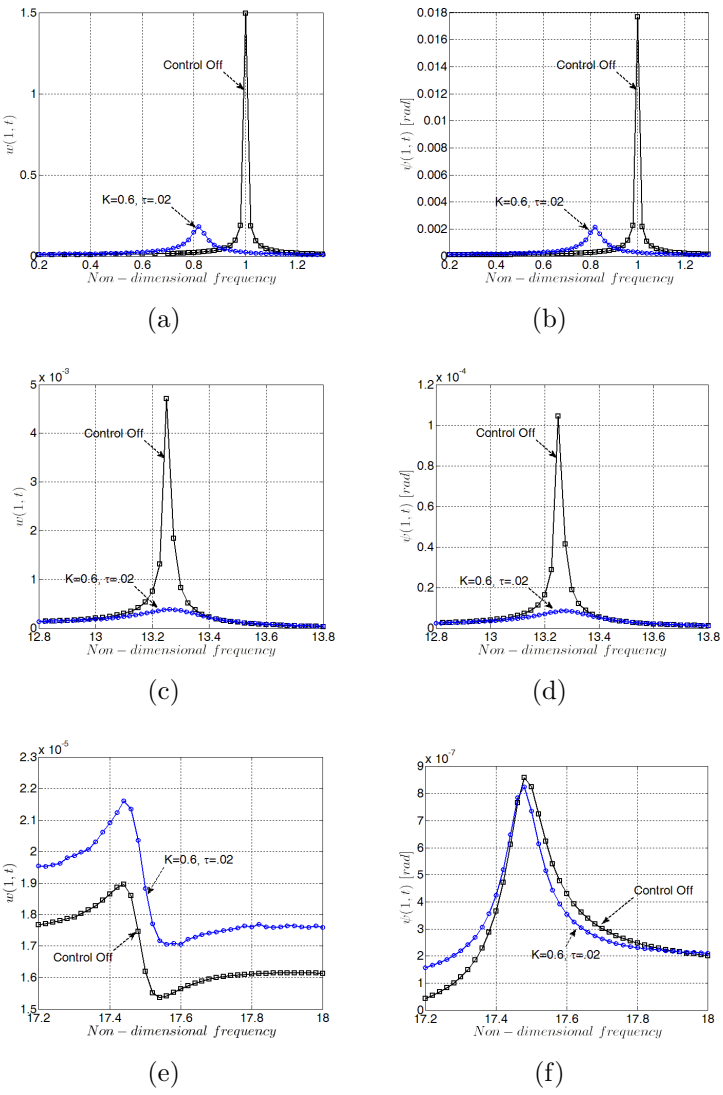

Figure 5.20: Frequency-response curves of the beam's tip (Beam II–Rigid body I). The controller is applied using a first-order filter ($\epsilon = 1/50$) and a piezoelectric patch oriented at $\beta = 45^o$. Results are obtained near (a, b) the first mode using $\ddot{w}_b = 0.1$; (c, d) the second mode using $\ddot{w}_b = 0.1$; and (e, f) the third mode and $\ddot{w}_b = 10.0$.

Since it was very difficult to relate the controller gains obtained experimentally to those used in the theoretical study because of various modeling uncertainties, a scaling factor was implemented to shift the stability boundaries obtained experimentally until they coincide with those obtained theoretically. The delay axis however is kept the same without any scaling (Note that the scaling factor is kept constant in all

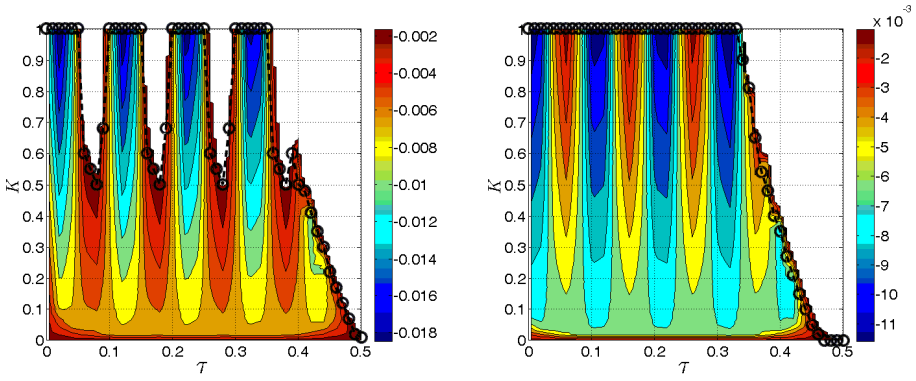

(a) (b)

Figure 5.21: Stability maps of the controller using the theoretical model (solid line) and experimental data (circles). Results are obtained for Beam I–Rigid body I using (a) a first-order BLPF with $\epsilon = 0.1$; and (b) a first-order BLPF with $\epsilon = 0.2$.

experiments). After implementing the correct scaling factor, one can observe excellent qualitative agreement between the theory and experiments. The stability boundaries are well estimated and the effect of adding a filter on the stability diagram is well reflected. Furthermore, in agreement with the theoretical findings, the influence of increasing the cut-off frequency of the filter on the first stability pocket is clear in that it shifts the unstable pockets toward larger gains creating one large pocket of stability, thereby enhancing the robustness of the controller to parameter uncertainties.

To investigate the effectiveness of the controller in rejecting external disturbances, the beam is subjected to an impulse using the electrodynamic shaker and the response is subsequently monitored using a laser sensor. Figure 5.22 compares the controlled and uncontrolled responses of the beam's tip deflection using different gain-delay combinations. Results demonstrate that, for all gain-delay combinations utilized in the experiments, the settling time of the controlled response is much shorter than the natural response of the beam. Additionally, in agreement with the theoretical damping contours depicted in Fig. 5.21 (b), the gain-delay combination

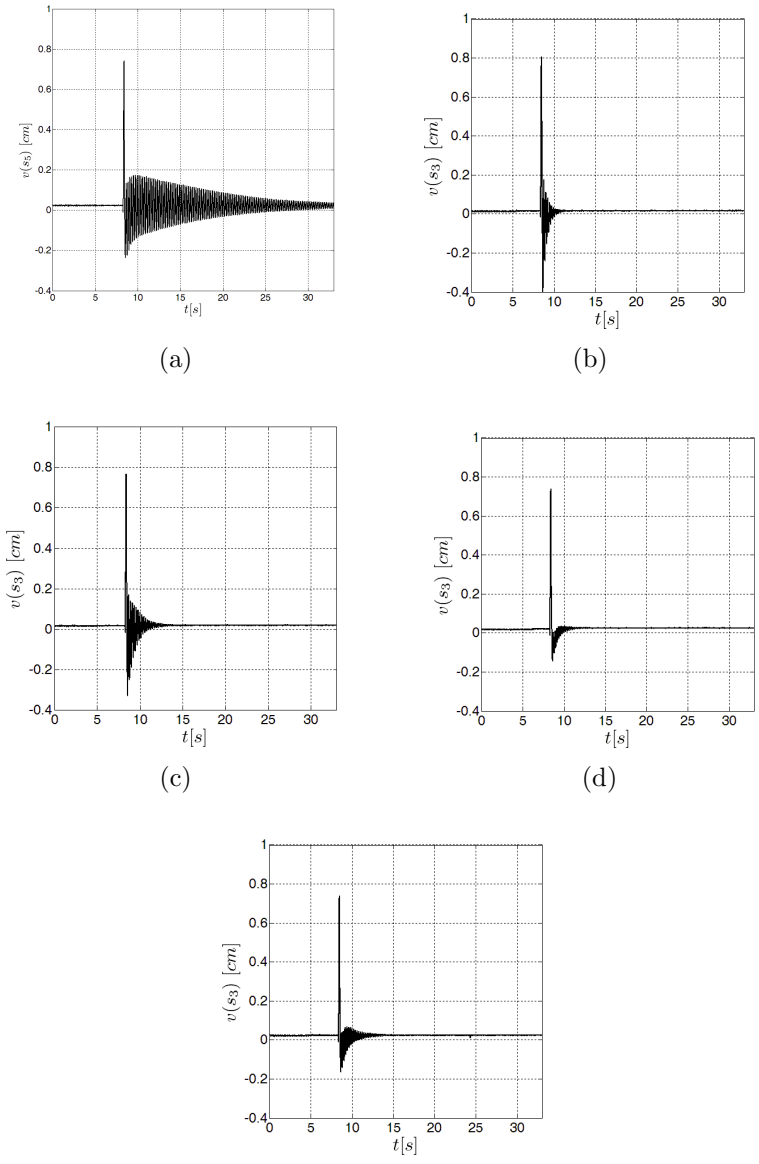

Figure 5.22: Experimental time histories of the beam's response to an impulse (Beam-I Rigid Body-I). (a) Natural decay, (b) controlled response using a first-order BLPF with ϵ= 0.2, $K = 0.4$, and $\tau = 0.07$, (c) controlled response using a second-order BLPF with ϵ= 0.2, $K = 0.2$, and $\tau = 0.07$, (d) controlled response using a first-order BLPF with ϵ= 0.2, $K = 0.4$, and $\tau = 0.33$, (e) controlled response using a second-order BLPF with ϵ= 0.2, $K = 0.2$, and $\tau = 0.33$.

$K = 0.4$ and $\tau = 0.33$ seems to produce larger damping when compared to $K = 0.4$ and $\tau = 0.07$ as evident from the shorter settling of the response, see Figs. 5.22 (b) and (d). Most importantly, none of the gain-delay combinations chosen from the stability pockets has a destabilizing influence on the impulse response of the beam which contains a wide spectrum of frequencies, further demonstrating the effectiveness of the controller in stabilizing the infinite linearly-coupled modes of this structure.

The effectiveness of the controller in reducing the beam's response amplitude under persistent harmonic base excitations is also investigated experimentally in Fig. 5.23. In the case of the first mode, two different gain-delay combinations are chosen from Fig. 5.21 (b). Both of these combinations are very effective in significantly reducing the bending component of the tip response as shown in Fig. 5.23(a). Since, as mentioned previously, the delay has a periodic influence on the location of the peak frequency. One of these combinations shifts the peak frequency to the left while the other shifts it to the right. For the beam considered and the base acceleration used in this experiment (0.084 m/sec^2), the torsion component associated with the first mode was very small (within the noise limit of the sensors).

The bending and torsion components of the beam's tip response near the second vibration mode are shown in Fig. 5.23 (b) and (c). The controller is capable of reducing the tip response of the beam near the second mode using the same gain-delay combination used for the first mode. As such, the gain-delay combination of the controller need not be changed to suppress large amplitude oscillations near multiple vibration modes constituting an important characteristic of the controller. It can also be noted that the frequency-response curves are bent slightly to the left, a characteristic of a nonlinear softening behavior usually associated with the second-mode dynamics of cantilever beams. The influence of such nonlinearities have been neglected in the theoretical part of this investigation.

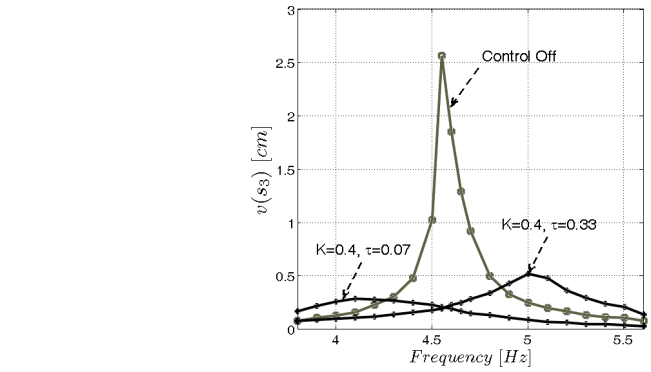

(a)

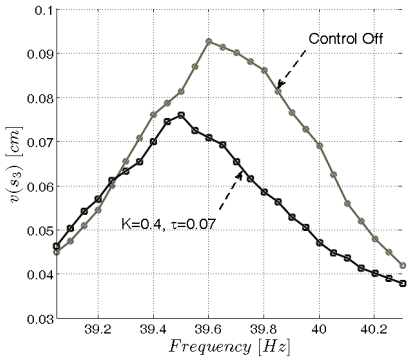

(b)

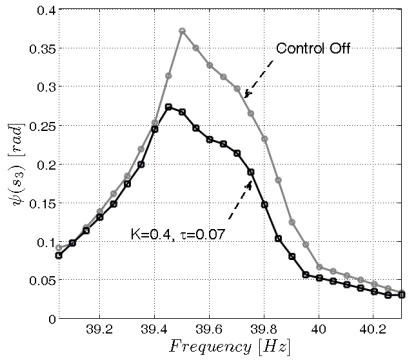

(c)

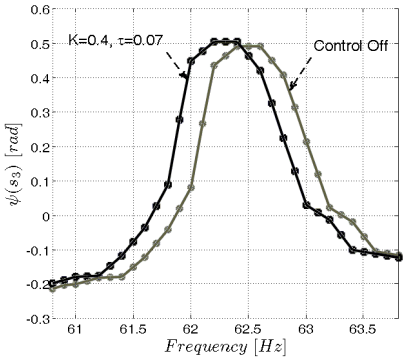

(d)

Figure 5.23: Frequency-response curves of Beam I–Rigid body I. (a) First mode response using a base acceleration of 0.084 m/sec^2, (b,c) second mode response using a base acceleration of 0.53 m/sec^2, (d) third mode response using a base acceleration of 7.07 m/sec^2. Controlled results are obtained using a first-order BLPF and $\epsilon = 0.2$.

As mentioned previously, since the base excitation is perpendicular to the axis of the beam along the bending direction, it was very difficult to excite large amplitude responses near the third, torsion–dominated modal frequency using the same levels of input acceleration. As such, we increased the base acceleration by almost a hundred times to about 7.07 m/sec^2. Using the same gain-delay combinations and a piezoelectric patch that is oriented at zero degree angles with respect to the axis of the beam, the controller was not effective in reducing the torsional vibrations near the third mode. This is in agreement with the theoretical findings depicted in Fig. 5.19 (f). In agreement with figure 5.19(f) the bending component of this mode was very small to be effectively measured using the laser sensors.

Chapter 6

On Primary Resonances of Weakly Nonlinear Delay Systems With Cubic Nonlinearities

This Chapter discusses the theoretical implementation of the Method of Multiple Scales to investigate primary resonances of a weakly-nonlinear second-order delay system with cubic nonlinearities. In contrast to previous studies where the implementation is confined to the assumption of linear delay terms with small coefficients [54, 55]; in this chapter, we propose a modified approach which alleviates that assumption and permits treating a problem with arbitrarily large gains. The modified approach lumps the delay state into unknown linear damping and stiffness terms that are function of the gain and delay. These unknown functions are determined by enforcing the linear part of the steady-state solution acquired via the Method of Multiple Scales to match that obtained directly by solving the forced linear problem. We examine the validity of the modified procedure by comparing its results to solutions obtained via a Harmonic Balance approach. Several examples are discussed demonstrating the ability of the proposed methodology to predict the ampli-

tude, softening-hardening characteristics, and stability of the resulting steady-state responses. Analytical results also reveal that the system can exhibit responses with different nonlinear characteristics near its multiple delay frequencies.

6.1 Introduction

Despite the large number of research studies on delay systems, most of the previous efforts were directed towards characterizing the stability of the free response by proposing various methodologies to predict and estimate the location of the eigenvalues relative to the imaginary axis [52, 53]. Little attention has been paid to understanding the effect of time delays on the response of nonlinear *externally-excited systems* [54, 55]. In particular, the nonlinear response of a delayed system to primary-resonance excitations has yet to be addressed comprehensively. Such studies were not very prevalent in the past due to the limited number of applications in which time delays and external excitations coexisted in the operation of a dynamic system. Currently, and due to the the emergence of microdevices as the next generation sensors and actuators, this type of analysis is becoming more imperative. For instance, to realize large dynamic responses, microdevices are usually excited at one of their resonant frequencies. To enhance their dynamic characteristics, feedback control algorithms are being implemented to close the loop and provide real-time information about the states. However, due to their high natural frequencies, the presence of the infinitesimal measurement delays in the control loop can be of the same order of magnitude of the response period, thereby channeling energy into or out of the system at incorrect time intervals and producing instabilities that render traditional controllers' performance ineffective [56].

To resolve this issue, there is a growing interest in the control and dynamic communities to utilize delayed-feedback controllers for vibration mitigation and control of

dynamic systems. In such controllers, system's delays are carefully augmented into a larger delay period to enhance the damping characteristics [43]. In one demonstration, delayed-feedback algorithms have been successfully implemented at the macroscale to mitigate potentially hazardous oscillations of suspended objects on various types of cranes [36, 38, 105] and active vibration control of externally-excited macrobeams [106, 107, 35, 33, 108, 109, 62, 110, 111]. Most recently, the same idea was also adapted to control microcantilevers in dynamic force microscopy [57], to eliminate chaotic motions in taping-mode atomic force microscopy [58], for sensor sensitivity enhancement in nanomechanical cantilever sensors [112] and to control the quality factor in dynamic atomic force microscopy [56]. Successful implementation of these controllers, especially when the objective is to mitigate large amplitude oscillations resulting from external excitations requires a deep analytical understanding of the primary resonance phenomenon in time-delayed systems.

In this Chapter, we investigate the response of a second-order weakly nonlinear delay system with cubic nonlinearities to primary resonance excitations. One way to achieve this understanding is to analytically construct an approximate solution using the Method of Multiple Scales (MMS) [113]. However, the implementation of this method is not trivial especially when the linear delay terms have large coefficients. As such, previous studies were restricted to the assumption that the linear delay terms have small coefficients [54, 55]. In such a case, the MMS can be directly implemented to attack the problem because the gains can be scaled at the same order of the perturbation problem as the nonlinearities, internal damping, and external excitation. For many applications, however, especially feedback control, these coefficients, referred to as gains, can be large. In that scenario, direct implementation of the MMS as demonstrated in [54, 55] yields solutions that can deviate significantly from the actual system's response. By scaling the linear gains at the higher order of the perturbation problem, one implicitly assumes that the response of the system can be approximated by one eigenfrequency that is very close to the

system's natural frequency. This assumption is clearly invalid when the gains are large.

To alleviate this problem, this Dissertation presents a modified approach that permits implementing the MMS to a weakly nonlinear delay system with large gains. To explain the proposed methodology, we will consider a second-order weakly nonlinear system whose equation of motion take the form:

$$\frac{d^2u}{dt^2} + 2\mu\frac{du}{dt} + \omega_n^2 u = -K\frac{d^j u(t-\tau)}{dt^j} - \alpha u^3 - 2\beta u\left[u\frac{d^2u}{dt^2} + \left(\frac{du}{dt}\right)^2\right] + F\cos(\Omega t)$$
$$j = 0, 1, 2 \tag{6.1}$$

where u is the state, μ is a linear damping term, ω_n is the natural frequency, K is the coefficient of the linear-delayed state, loosely referred to as the linear gain, τ is a discrete time delay, F is the level of external excitation, Ω is the excitation frequency, j is the order of the derivative associated with the linear delay term, and α and β are respectively the coefficients of geometric and inertia nonlinearities. When β is set to zero, Equation (6.1) represents an externally-excited duffing oscillator subjected to delayed-feedback control. Whereas, for nonzero values of β, the system can be used to represent the single-mode dynamics of an externally-excited cantilever beam subjected to delayed-feedback control.

To clarify the basis for the modified procedure, we first analyze the response of the linear, free and forced, system (Section 6.2). We obtain the linear steady-state solution and use it to create a distinction between the peak and delay frequencies. Subsequently, in Section 6.3, we analyze the primary resonance of the nonlinear system. We show through comparisons with the Method of Harmonic Balance that direct implementation of the MMS may result in erroneous predictions especially when the linear delay terms have large coefficients. We present the modified ap-

proach and demonstrate its ability to capture the nonlinear response and stability of the system. We implement the modified approach to analyze the response of i) a weakly nonlinear duffing oscillator with linear delayed feedback; ii) a weakly nonlinear system with geometric and inertia nonlinearities subjected to linear delayed feedback.

6.2 Linear Analysis:

6.2.1 Free Response:

Before the modified approach is presented and implemented, it is imperative to develop a good understanding of the linear response characteristics as they will define the regions of gain and delay wherein the modified approach is capable of presenting the response of the forced nonlinear system. As such, the local stability of the equilibrium solutions of the unforced system is determined by finding the eigenvalues, λ, of the linearized equation when F is equal to zero. These eigenvalues are obtained by substituting a homogeneous solution of the form, $u_h = c\ exp(\lambda t)$, into Equation (6.1) and obtaining

$$(\omega_n^2 + \lambda^2) + 2\mu\lambda + K\lambda^j e^{-\lambda\tau} = 0, \qquad j = 0, 1, 2. \tag{6.2}$$

Due to the presence of delay in the linear state, Equation (6.2) takes the form of a quasi-polynomial having infinite number of solutions associated with every set of fixed parameters (K,τ). By inspecting the form of the homogeneous solution, u_h, it becomes evident that the stability of the equilibrium solutions is determined by the sign of the real part of the eigenvalues ($\lambda = \zeta_d \pm i\omega_d$). In particular, the equilibrium solutions are locally asymptotically stable if all the eigenvalues have negative real

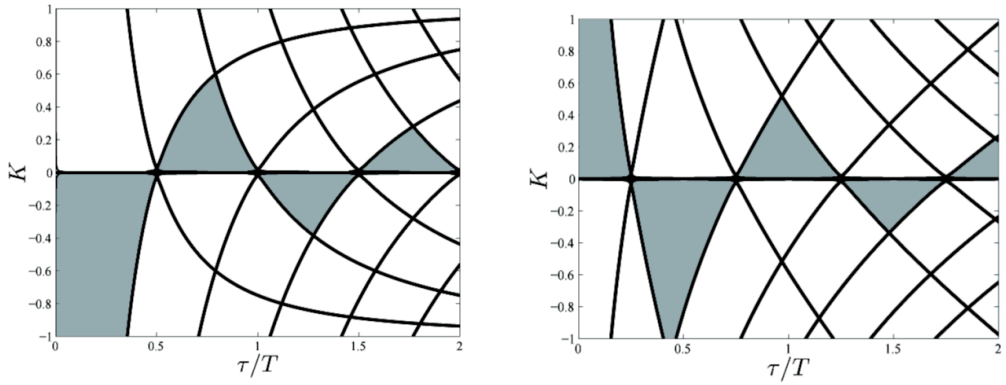

(a) $j = 0$ (b) $j = 1$

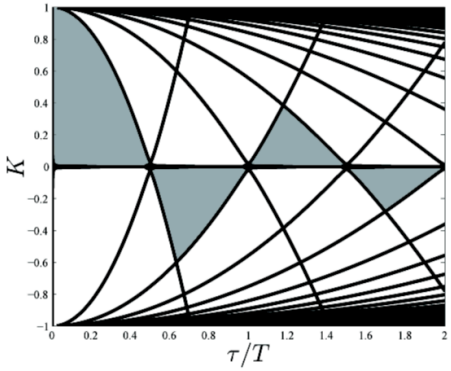

(c) $j = 2$

Figure 6.1: Stability maps of the equilibrium solutions of Equation (6.1) for a) $j = 0$, b) $j = 1$, and c) $j = 2$. Shaded regions represent asymptotically stable equilibria. Results are obtained for $\omega_n = 1$ and $\mu = 0.005$.

parts, $\zeta_d < 0$, and unstable if at least one eigenvalue has a positive real part, $\zeta_d > 0$.[1] Thus, to determine the stability boundaries, we set the real part of the eigenvalue ζ_d equal to zero and substitute $\lambda = i\omega_d$ into Equation (6.2), then separate the real and imaginary parts of the outcome to obtain

$$(\omega_n^2 - \hat{\omega}_d^2) + (-1)^j \hat{K} \frac{d^j}{d\hat{\tau}^j} \left[\cos(\hat{\omega}_d \hat{\tau})\right] = 0, \tag{6.3a}$$

[1]When $j = 2$, the delay system is of the neutral type requiring stronger conditions for stability. For more details, we refer the reader to [2].

$$2\mu\hat{\omega}_d - (-1)^j \hat{K} \frac{d^j}{d\hat{\tau}^j} \left[\sin(\hat{\omega}_d \hat{\tau})\right] = 0, \qquad j = 0, 1, 2. \tag{6.3b}$$

where the hat denotes the gain, delay, and response frequency at the stability boundaries. For a given gain $\hat{K}$, Equations (6.3) can be solved for the delay $\hat{\tau}$ and the associated frequency at the boundary, $\hat{\omega}_d$. To better visualize the stability of the equilibrium solutions, the gain-delay space is mapped into stable and unstable regions as depicted in Fig. 6.1, where shaded regions represent gain-delay combinations leading to asymptotically stable equilibria.

It is worth noting that Equations (6.3) are invariant under the transformation $\hat{\omega}_d \leftrightarrow -\hat{\omega}_d$ and have no solution when $\hat{\omega}_d = 0$. This implies that, at the stability boundaries, Equation (6.2) has a pair of complex conjugate eigenvalues, while all of its other eigenvalues have nonzero real parts. If these eigenvalues have a traversal or nonzero-speed crossing of the imaginary axis, then the stability boundaries represent *Hopf Bifurcation* curves [114, 115]. To check if the transversality condition is satisfied, we let the analytic continuation of the eigenvalues $\pm i\hat{\omega}_d$ be λ_1 and λ_2. We differentiate all the terms in Equation (6.2) with respect to the bifurcation parameter, say K, then evaluate the resulting equation at $(\hat{K},\hat{\tau},\hat{\omega}_d)$ and $\pm i\hat{\omega}_d$ to obtain

$$Re\left\{\frac{d\lambda_{1,2}}{dK}\right\}\Big|_{(\hat{K},\hat{\omega}_d,\hat{\tau})} = \begin{cases} 2\hat{\omega}_d \hat{K} \frac{\left(\hat{K}^2 + 4\mu^4 - 4\mu^2\omega_n^2\right)}{\eta_0} & j = 0 \\ 2\hat{\omega}_d^3 \frac{\left(\hat{K}^4 - (8\mu^2 - 4\omega_n^2)\hat{K}^2 + 16\mu^2(1-\omega_n^2)\right)}{\eta_1} & j = 1 \\ 2\hat{\omega}_d^5 \frac{\left(4\omega_n^2\hat{K}^2 + (4\mu^2 - 2\omega_n^2)^2 - 4\omega_n^2\right)}{\eta_2} & j = 2 \end{cases} \tag{6.4}$$

where

$$\begin{aligned} \eta_j = &- 4\hat{K}\mu\hat{\omega}_d(ij + \hat{\tau}\hat{\omega}_d)\cos(\hat{\tau}\hat{\omega}_d)(i\hat{\omega}_d)^j + 4\hat{K}\hat{\omega}_d^2(ij + \hat{\tau}\hat{\omega}_d)\sin(\hat{\tau}\hat{\omega}_d)(i\hat{\omega}_d)^j \\ &- j^2\hat{K}^2(i\hat{\omega}_d)^{2j} + \hat{K}^2\tau^2\hat{\omega}_d^2(i\hat{\omega}_d)^{2j} + 2j\hat{K}^2\hat{\tau}(i\hat{\omega}_d)^{2j+1} + 4\hat{\omega}_d^4 + 4\mu^2\hat{\omega}_d^2, \qquad j = 0, 1, 2. \end{aligned}$$

Because the real parts of $\frac{d\lambda_{1,2}}{dK}$ are nonzero except for the points where the numerator of Equation (4) vanishes. The transversality condition is satisfied everywhere except

at the points corresponding to the roots of

$$\begin{cases} \hat{K}^2 + 4\mu^4 - 4\mu^2\omega_n^2 = 0 & j = 0 \\ \hat{K}^4 - (8\mu^2 - 4\omega_n^2)\hat{K}^2 + 16\mu^2(1-\omega_n^2) = 0 & j = 1 \\ 4\omega_n^2\hat{K}^2 + (4\mu^2 - 2\omega_n^2)^2 - 4\omega_n^2 = 0 & j = 2 \end{cases} \tag{6.5}$$

At these points, the linear analysis is incapable of determining whether the stability boundary represents a Hopf Bifurcation curve. It turns out that the singular points of Equation (5) are the points of intersection between different critical frequency curves, $\hat{\omega}_d$.

6.2.2 Forced Response:

The Steady-State Solution:

Throughout this Chapter, we limit the analysis to gain-delay combinations leading to stable equilibrium solutions. In other words, we only consider gain-delay values in the shaded regions depicted in Fig. 6.1. This, however, is not equivalent to the small gain assumption as stable solutions can exist even when the gain is large. Based on this assumption, the homogeneous solution of Equation (6.1), u_h, decays with time and does not affect the steady-state response. Next, to determine the steady-state linear response of the forced system, we retain the linear terms in Equation (6.1) and assume a solution of the form

$$u_{ss}(t) = \frac{1}{2} a e^{i(\Omega t + \gamma)} + cc \tag{6.6}$$

where a and γ are respectively the steady-state amplitude and phase of the response and cc is the complex conjugate of the preceding term. Substituting Equation (6.6)

into the linearized version of Equation (6.1), we obtain

$$\begin{aligned}&\left\{\left((\omega_n^2-\Omega^2)+(-1)^jK\frac{d^j}{d\tau^j}[\cos(\Omega\tau)]\right)a-F\cos\gamma\right\}\\&+i\left\{\left(2\mu\Omega-(-1)^jK\frac{d^j}{d\tau^j}[\sin(\Omega\tau)]\right)a+F\sin\gamma\right\}=0\\&j=0,1,2.\end{aligned}\tag{6.7}$$

Now, setting the real and imaginary parts of Equation (6.7) equal to zero yields

$$\left((\omega_n^2-\Omega^2)+(-1)^jK\frac{d^j}{d\tau^j}[\cos(\Omega\tau)]\right)a=-F\cos\gamma\tag{6.8a}$$

$$\left(2\mu\Omega-(-1)^jK\frac{d^j}{d\tau^j}[\sin(\Omega\tau)]\right)a=F\sin\gamma,\qquad j=0,1,2\tag{6.8b}$$

Squaring and adding Equations (6.8) and solving the resulting equation for a gives

$$\begin{aligned}a=&\frac{F}{\sqrt{\left(\omega_n^2-\Omega^2+(-1)^jK\frac{d^j}{d\tau^j}[\cos(\Omega\tau)]\right)^2+\left(2\mu\Omega-(-1)^jK\frac{d^j}{d\tau^j}[\sin(\Omega\tau)]\right)^2}}\\&j=0,1,2\end{aligned}\tag{6.9}$$

Equation (6.9) represents the linear steady-state amplitude of the response. The corresponding steady-state phase, γ, can be obtained by using either one of Equations (6.8). By inspecting Equations (6.3) and (6.9), it becomes evident that, for gain-delay combinations at the stability boundary $(\hat{K},\hat{\tau})$, the linear response approaches infinity when the excitation frequency, Ω, approaches the corresponding delay frequency, $\hat{\omega}_d$. This singularity occurs regardless of the value of the system internal damping, μ.

Using Equations (6.6) and (6.9), the steady-state response can be written as

$$u_{ss}(t) = \frac{F}{\sqrt{\left(\omega_n^2 - \Omega^2 + (-1)^j K \frac{d^j}{d\tau^j}[\cos(\Omega\tau)]\right)^2 + \left(2\mu\Omega - (-1)^j K \frac{d^j}{d\tau^j}[\sin(\Omega\tau)]\right)^2}}$$
$$\times \cos(\Omega t + \gamma), \qquad j = 0, 1, 2 \tag{6.10}$$

where

$$\gamma = -\arctan \frac{2\mu\Omega - (-1)^j K \frac{d^j}{d\tau^j}[\sin(\Omega\tau)]}{\omega_n^2 - \Omega^2 + (-1)^j K \frac{d^j}{d\tau^j}[\cos(\Omega\tau)]} \tag{6.11}$$

Peak Versus Delay Frequencies:

When analyzing the primary resonance of a delay system, it is essential to create a distinction between the delay and peak frequencies. While a delay system possesses infinite delay frequencies, not every delay frequency yields a resonance peak in the frequency response. The presence of a response peak depends on the amount of damping associated with that delay frequency. To further illustrate this important notion, we determine the peak frequencies of the response by minimizing the denominator of Equation (6.9). At the local extrema, the derivative of the denominator with respect to Ω vanishes yielding the following equation:

$$\begin{aligned} R = &-(-1)^{2j} j K^2 \Omega_p^{2j} - 2\Omega_p^4 - 4\mu^2\Omega_p^2 + 2\omega_n^2\Omega_p^2 \\ &+ (-1)^j K \Omega_p^j \left((j + 2\mu\tau + 2)\Omega_p^2 - j\omega_n^2\right) \cos\left(\frac{\pi j}{2} + \tau\Omega_p\right) \\ &+ (-1)^j K \Omega_p^{j+1} \left(2(j+1)\mu + \tau\left(\omega_n^2 - \Omega_p^2\right)\right) \sin\left(\frac{\pi j}{2} + \tau\Omega_p\right) = 0, \quad j = 0, 1, 2. \end{aligned} \tag{6.12}$$

For local minima, we impose the condition

$$\frac{d^2 R}{d\Omega_p^2} > 0 \tag{6.13}$$

where Ω_p denotes the peak frequency. Equations (6.12) and (6.13) do not yield a unique solution. As such, the frequency-response curves of the forced response may exhibit more than one peak. The location and number of these peaks are influenced by the gain-delay parameters and the order of the linear derivative, j. To illustrate this fact, we consider the assumption of small internal damping, gain, and delay. In other words, we let $\mu = \epsilon\mu$, $K = \epsilon K$, and $\tau = \epsilon\tau$, then eliminate terms having higher orders of ϵ to obtain

$$\cos\left(\frac{\pi j}{2} + \tau\Omega_p\right) = \frac{2(-1)^{-j}\Omega_p^{2-j}\left(\Omega_p^2 - \omega_n^2\right)}{K\left(j(\Omega_p^2 - \omega_n^2) + 2\Omega_p^2\right)}, \qquad j = 0, 1, 2. \tag{6.14}$$

or

$$\cos\left(\frac{\pi j}{2} + \tau\Omega_p\right) - O\left(\frac{\Omega_p^{2-j}}{K}\right) = 0 \qquad j = 0, 1, 2. \tag{6.15}$$

where O denotes "*the order of*". The number of peak frequencies can be approximated by the number of real solutions of Equation (6.15) subjected to Equation (6.13). By examining Equation (6.15), it becomes evident that the number of peak frequencies is directly proportional to both j and the magnitude of K. For example, when $j = 0$, Equation (6.15) comprises of two functions: a bounded function represented by $\cos(\tau\Omega_p)$ and a quadratically varying (increasing/decreasing) function represented by Ω_p^2/K. The number of intersections between these curves and hence the number of peak frequencies is directly proportional to K.

Increasing the order of the derivative to $j = 1$ while keeping K constant yields a larger number of peak frequencies. In this situation, Equation (6.14) comprises of a bounded sinusoidal function, $\cos\left(\frac{\pi}{2} + \tau\Omega_p\right)$, and a linearly varying function, Ω_p/K. These functions can intersect a larger number of times because of the slower rate of change of Ω_p/K when compared to Ω_p^2/K. When $j = 2$, Equation (6.14) consists of two bounded curves, a sinusoid and a constant, $1/K$. For large values of K, these curves can intersect infinite number of times, thusly producing an infinite number of peak frequencies.

These findings are also demonstrated numerically in Table 1 which lists the first three peak frequencies at $\tau = 1.2\pi$ and different values of j and K. For a given j, the gains were

Table 6.1: The first three peak frequencies as calculated via Equation (6.12). Results are obtained for $\omega_n = 1$, $\mu = 0.005$, and $\tau = 1.2\pi$.

$j = 0$								
$K = 0.05$			$K = 0.2$			$K = 0.3$		
Ω_{p1}	Ω_{p2}	Ω_{p3}	Ω_{p1}	Ω_{p2}	Ω_{p3}	Ω_{p1}	Ω_{p2}	Ω_{p3}
0.9766	–	–	0.884345	–	–	0.833409	–	–
$j = 1$								
$K = -0.05$			$K = -0.2$			$K = -0.4$		
Ω_{p1}	Ω_{p2}	Ω_{p3}	Ω_{p1}	Ω_{p2}	Ω_{p3}	Ω_{p1}	Ω_{p2}	Ω_{p3}
1.01703	–	–	1.1133	–	–	0.721655	1.23672	–
$j = 2$								
$K = -0.05$			$K = -0.2$			$K = -0.4$		
Ω_{p1}	Ω_{p2}	Ω_{p3}	Ω_{p1}	Ω_{p2}	Ω_{p3}	Ω_{p1}	Ω_{p2}	Ω_{p3}
0.977379	–	–	0.906992	3.1689	4.90623	0.841806	1.61982	3.29911

chosen such that the gain-delay combination always lies inside the shaded regions depicted in Fig. 6.1. For small gains, there is only one peak frequency regardless of the order of the linear derivative, j. When the order of the linear derivative is increased to $j = 1$, and the magnitude of the gain is increased to $K = 0.4$ a new peak frequency appears at a smaller value of Ω.

When $j = 2$, the frequency response has only one peak for small gains but exhibits a very large number of peaks when $K = -0.2$ and -0.4 (only the first three are listed in Table 1). It is also worth noting that, in general, the smaller the gain is, the closer is the first peak frequency to the system's natural frequency.

Similar to delay-free systems, where the existence and convergence of the peak frequency to the natural frequency is characterized by the system's internal damping; in delay systems, the existence and convergence of a given peak frequency to the associated delay frequency is characterized by the absolute value of the damping parameter ζ_d, Fig. 6.2(b). Figure 6.2(a) illustrates the relation between the peak frequencies, Ω_p, and the imaginary parts of the eigenvalues, ω_d. The figure, which displays variation of the first four peak and delay frequencies with the gain, demonstrates that the first delay frequency, ω_{d1}, coincides with the the first peak frequency, Ω_{p1}, over the whole gain range. The second peak frequency,

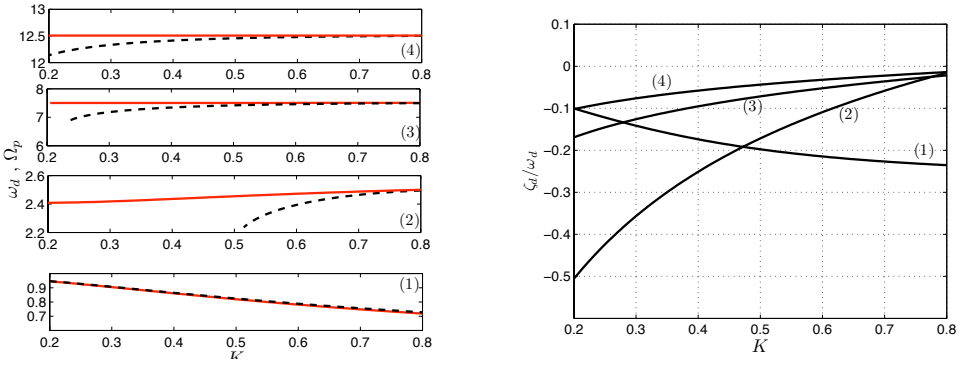

(a) (b)

Figure 6.2: a) Variation of the first four delay frequencies, ω_d, (solid lines) and the associated peak frequencies, Ω_p, (dashed lines) with the gain K. b) Variation of the associated damping ratios ζ_d/ω_d with the gain K. Results are obtained for a fixed delay $\tau = 0.2\pi$, $\omega_n = 1$, $\mu = 0.005$ and $j = 2$.

ω_{p2}, however exists only for values of K greater than $K \approx 0.5$ and approaches the second-delay frequency, ω_{d2}, only when the gain is large.

These results clearly indicate that the peak frequencies exist over a wider range of the gain and converge to the associated delay frequencies as the magnitude of ζ_d decreases. For example, consider the second-delay frequency, ω_{d2}. For small gains, ζ_{d2} is very large and there is no peak frequency associated with ω_{d2}. However, as the gain increases and approaches $K \approx 0.5$, the peak frequency appears because ζ_{d2} decreases beyond a critical value.

By the preceding discussion, we meant to illustrate that delay systems can exhibit primary resonances at a large number of frequencies. Depending on the gain and delay values, these resonances may occur at frequencies that are far from the natural frequency ω_n. Furthermore, not every delay frequency, ω_d, obtained via the linear unforced eigenvalue problem yields a peak frequency. This can be realized by simply noting that, while the free response always yields infinite number of eigenfrequencies, ω_d, associated with every nonzero set of parameters (K, τ), the forced response might exhibit only one peak for the same parameter set. As such it is safe to conclude that *not every delay frequency yields a peak frequency, but every peak frequency is associated with a delay frequency.*

6.3 Nonlinear Analysis:

6.3.1 Analytical Solution of The Nonlinear Problem

Direct Application of The Method of Multiple Scales:

Throughout this Chapter, we will try to analyze the primary resonance of Equation (6.1) near the resulting multiple peak frequencies discussed in the previous section. Previously, Hu et al. [54] and Ji and Leung [55] utilized the MMS to study the primary resonance of a duffing system with linear delay terms. Both studies were confined to the assumption of very weak gains. As such, the resulting analytical solutions only predicted the response behavior near the natural frequency and obviously cannot predict the response near the multiple resonances of delay systems. To understand the limitations of the direct approach, we first attack the problem in a manner similar to [54, 55]. We limit the analysis to linear delay terms (i.e., $G = 0$), and seek a second-order nonlinear solution in the form

$$u(T_0, T_1) = u_0(T_0, T_1) + \epsilon u_1(T_0, T_1) + O(\epsilon^2), \tag{6.16}$$

where $T_n = \epsilon^n t$ and ϵ is a small bookkeeping parameter. In terms of the T_n, the time derivative becomes

$$\frac{d}{dt} = D_0 + \epsilon D_1, \tag{6.17}$$

where $D_n = \partial/\partial T_n$. We order the amplitude of excitation, F, and the feedback gain, K, so that they appear in the same perturbation equation as the damping, μ, and nonlinear terms described by the coefficients α and β. As such, we let

$$\mu = \epsilon\mu, \qquad F = \epsilon F, \qquad K = \epsilon K, \qquad \alpha = \epsilon\alpha, \qquad \beta = \epsilon\beta. \tag{6.18}$$

To investigate the response near the primary resonance ($\Omega \approx \omega_n$), we introduce a detuning parameter, σ, that characterizes the nearness of the excitation frequency, Ω, to the natural frequency, and let

$$\Omega = \omega_n + \epsilon\sigma. \tag{6.19}$$

It is worth noting that Equation (6.19) is invalid when the response has more than one peak frequency or when the response frequency is not very close to ω_n. These conditions are satisfied only when the gain is very small. Substituting Equations (6.16–6.19) into Equation (6.1) and equating coefficients of like powers of ϵ, we obtain

$$O(1): \quad D_0^2 u_0 + \omega_n^2 u_0 = 0, \tag{6.20}$$

$$\begin{aligned} O(\epsilon): \quad D_0^2 u_1 + \omega_n^2 u_1 = & -2D_0 D_1 u_0 - \mu D_0 u_0 + F\cos(\omega_n T_0 + \sigma T_1) - \alpha u_0^3 \\ & - 2\beta(u_0(D_0 u_0)^2 + D_0^2 u_0 u_0^2) - K D_0^{(j)} u_0(T_0 - \tau, T_1),\ j = 0, 1, 2. \end{aligned} \tag{6.21}$$

The solution of the first order equation, Equation (6.20), can be written as

$$u_0 = A(T_1)e^{i\omega_n T_0} + \bar{A}(T_1)e^{-i\omega_n T_0}, \tag{6.22}$$

where $A(T_1)$ is an unknown complex function that will be determined by imposing the solvability conditions at the next level of approximation and $\bar{A}(T_1)$ is its complex conjugate. Substituting Equation (6.22) into Equation (6.21) and eliminating the secular terms (i.e., terms leading to $e^{\pm i\omega_n T_0}$) yields

$$-2i\omega_n D_1 A - 2\mu i\omega_n A + \frac{F}{2}e^{i\sigma T_1} + (4\beta\omega_n^2 - 3\alpha)A^2\bar{A} - K(i\omega_n)^j A e^{-i\omega_n \tau} = 0. \tag{6.23}$$

In solving Equation (6.23), we find it convenient to express $A(T_1)$ in the polar form

$$A(T_1) = \frac{1}{2}a(T_1)e^{i\psi(T_1)}, \qquad \bar{A}(T_1) = \frac{1}{2}a(T_1)e^{-i\psi(T_1)}, \tag{6.24}$$

where a and ψ are real functions of time. Substituting Equation (6.24) into Equation (6.23) and separating the real and imaginary parts of the resulting equation, we obtain

$$\omega_n a' = -\mu_{eff}\omega_n a + \frac{F}{2}\sin\gamma, \tag{6.25a}$$

$$\omega_n a\gamma' = (\sigma\omega_n + \Sigma)a - N_{eff}a^3 + \frac{F}{2}\cos\gamma, \tag{6.25b}$$

where the primes are derivatives with respect to T_1, $\gamma = \sigma T_1 - \psi$,

$$N_{eff} = \frac{3\alpha}{8} - \frac{\omega_n^2 \beta}{2}, \tag{6.26}$$

is the coefficient of effective nonlinearity which determines the softening-hardening characteristics of the response, and

$$\mu_{eff} = (\mu - (-1)^j \frac{K}{2\omega_n} \frac{d^j}{d\tau^j}[\sin(\omega_n \tau)]), \qquad j = 0, 1, 2, \tag{6.27}$$

is a measure of the effective damping in the system which is clearly dependent on the gain, K, and the delay, τ. Consequently, depending on the sign of $(-1)^j K \frac{d^j}{d\tau^j}[\sin(\omega_n \tau)]$ which is periodic in τ, the presence of delays can increase or decrease the amount of damping introduced into the system. Further, the term

$$\Sigma = (-1)^{j+1} \frac{K}{2} \frac{d^j}{d\tau^j}[\cos(\omega_n \tau)], \qquad j = 0, 1, 2, \tag{6.28}$$

represents a linear shift in the response frequency from ω_n. Equations (6.25a) and (6.25b) represent the modulation equations of the response and are used to study time evolution of the response amplitude and phase. For steady-state solutions, we set $a\prime = \gamma\prime = 0$, which corresponds to the singular points of Equations (6.25a) and (6.25b) that are obtained by solving

$$\mu_{eff} \omega_n a_0 = \frac{F}{2} \sin \gamma_0, \qquad -(\sigma \omega_n + \Sigma) a_0 + N_{eff} a_0^3 = \frac{F}{2} \cos \gamma_0. \tag{6.29}$$

Squaring and adding Equations (6.29), one obtains the following frequency-response equation:

$$\mu_{eff}^2 \omega_n^2 a_0^2 + \Big((\sigma \omega_n + \Sigma) a_0 - N_{eff} a_0^3) \Big)^2 = \frac{F^2}{4}. \tag{6.30}$$

For given system parameters and certain level of external excitation, F, Equation (6.30) can be solved for the steady-state response amplitude, a_0. The corresponding phase, γ_0, can be obtained by utilizing either one of Equations (6.29).

The stability of the resulting steady-state solutions is assessed by finding the eigenvalues of the Jacobian of the modulation equations evaluated at the roots (a_0, γ_0). Using

Equations (6.25a) and (6.25b), the characteristic equation can be written as

$$s^2 + 2\mu_{eff}s + \mu_{eff}^2 + \frac{1}{\omega_n^2}\left(\sigma\omega_n + \Sigma - N_{eff}a_0^2\right)\left(\sigma\omega_n + \Sigma - 3N_{eff}a_0^2\right) = 0. \tag{6.31}$$

The roots (a_0, γ_0) are asymptotically stable, if all the eigenvalues, s, have negative real parts and are unstable if at least one eigenvalue has a positive real part. Using the Routh-Hurwitz criterion, one can easily show that Equation (6.31) admits solutions with negative real parts if and only if the following two conditions are satisfied:

$$\mu_{eff} > 0, \qquad \mu_{eff}^2 + \left(\sigma\omega_n + \Sigma - N_{eff}a_0^2\right)\left(\sigma\omega_n + \Sigma - 3N_{eff}a_0^2\right) > 0. \tag{6.32}$$

Under the small gain assumption, i.e., when $\hat{\omega}_d \approx \omega_n$, the first condition in Equation (6.32) is equivalent to Equation (6.3b).

To validate the steady-state analytical solution, the frequency-response curves are generated and compared to those obtained using the Method of Harmonic Balance [32]. In the Method of Harmonic Balance, the number of harmonics kept in the series is increased until the solution converges to that obtained via long-time integration of Equation (6.1). Since Equation (6.1) only has cubic nonlinearities, only odd harmonics contribute to the solution. We found that, even for large response amplitudes, two odd harmonics are sufficient to yield accurate results. The stability of solutions acquired via the Method of Harmonic Balance was further assessed using the Floquet Theory. Since the details of this analysis is beyond the scope of this work, we refer the reader to [32][2].

For small gains, Equations (6.25a) and (6.25b) represent a good approximation of the response as illustrated in Fig. 6.3(a) and demonstrated previously in [54, 55]. When $\beta = 0$ and $\alpha > 0$ (*hardening response*), the perturbation solution closely predicts the response obtained using the Method of Harmonic Balance. On the other hand, when $\beta = 0$ and $\alpha < 0$ (*softening response*), the perturbation solution slightly underestimates the numerical solution. To understand the source of the discrepancy, it is necessary to realize that for

[2]Implementation of the Method of Harmonic Balance and the Floquet Theory to study the response and stability of Time-Delay Systems has been comprehensively studied in the literature. For example, the reader can refer to the work by Nayfeh et al. on chatter tool dynamics [116].

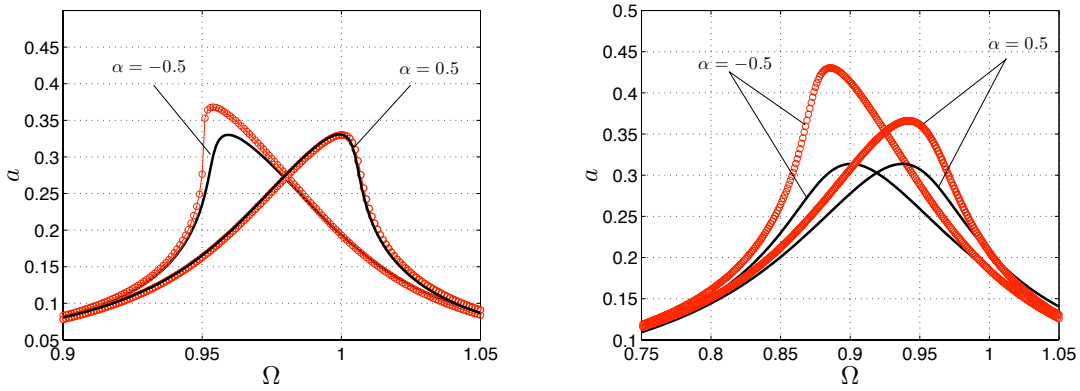

(a) (b)

Figure 6.3: Nonlinear frequency-response curves obtained using the Method of Harmonic Balance (circles) and the approximate perturbation solution (solid line). Results are obtained for a) $K = 0.05, \tau = 0.2\pi, j = 2$, and $F = 0.013$ and b) $K = 0.2, \tau = 0.2\pi, j = 2$, and $F = 0.04$.

the gain-delay combination considered, the first peak frequency, Ω_{p1}, occurs at a value very close to but less than $\omega_n = 1$. As a consequence, when $\alpha > 0$, the frequency-response curves bend to the right towards larger values of Ω and closer to ω_n. As such, by virtue of Equation (6.19), the perturbation solution is expected to closely predict the numerical response near ω_n. For softening-type responses however, large amplitude motions occur at smaller values of Ω and further away from ω_n. As a result, the approximate perturbation solution underestimates the actual response.

As the gain is increased to $K = 0.2$, Fig. 6.3(b), the perturbation solution deviates significantly from the actual solution. This basically stems from the large deviation between the peak frequency and the natural frequency. In addition, since Equation (6.30) is invariant under the transformation

$$\sigma\omega_n + \Sigma \Longleftrightarrow -(\sigma\omega_n + \Sigma), \qquad N_{eff} \Longleftrightarrow -N_{eff}, \tag{6.33}$$

the frequency-response curves obtained using the perturbation solution are mirror images around an axis passing through $\sigma\omega_n + \Sigma$, as shown in Figs. 6.3(a) and 6.3(b). However, solutions acquired via the Method of Harmonic Balance yield frequency-response curves

that are not mirror images around that axis. Consequently, one may conclude that, for large gains, N_{eff}, μ_{eff}, and Σ cannot be accurately described by Equations (6.26), (6.27), and (6.28).

The Modified Approach

The preceding discussion motivates a new approach to study primary resonances of delays systems near peak frequencies that are not necessarily close to ω_n. Towards that end, we propose a modification to the approach presented earlier. Again, we make use of the MMS but this time we extract the delay from the linear states and write Equation (6.1) in the following form:

$$\frac{d^2u}{dt^2} + 2|f_1(K,\tau)|\frac{du}{dt} + |f_2(K,\tau)|u = F\cos(\Omega t) - \alpha u^3 - 2\beta u\left[u\frac{d^2u}{dt^2} + \left(\frac{du}{dt}\right)^2\right], \quad (6.34)$$

where G is taken to be zero, and f_1 and f_2 are unknown nonzero functions of K and τ that will be determined at a later stage in the perturbation analysis. The motivation behind lumping the delayed state into stiffness and damping terms stems from previous knowledge that the linear delay will affect the effective stiffness and damping of the system. For the times being, we will assume that this influence is unknown and yet to be determined. As mentioned earlier, since the analysis is limited to asymptotically stable free responses, absolute values of the unknown functions are used to guarantee this condition. Next, we express the solution of Equation (6.34) in the form

$$u(T_0,T_1) = u_0(T_0,T_1) + \epsilon u_1(T_0,T_1) + O(\epsilon^2). \quad (6.35)$$

We order the amplitude of excitation and nonlinearities so that they appear in the same perturbation equation as the effective unknown damping function, f_1. In other words, we let

$$f_1 = \epsilon f_1, \qquad F = \epsilon F, \qquad \alpha = \epsilon\alpha, \qquad \beta = \epsilon\beta. \quad (6.36)$$

We express the nearness of the excitation frequency, Ω, to the unknown frequency function, f_2, by introducing a detuning parameter and letting

$$\Omega^2 = |f_2| + \epsilon\sigma. \tag{6.37}$$

For small ϵ, Equation (6.37) can be written as

$$\Omega \approx \sqrt{|f_2|} + \frac{1}{2\sqrt{|f_2|}}\epsilon\sigma. \tag{6.38}$$

Substituting Equation (6.35), (6.36), and (6.38) into Equation (6.34) and equating coefficients of like powers of ϵ, we obtain

$$O(1): \quad D_0^2 u_0 + |f_2| u_0 = 0, \tag{6.39}$$

$$O(\epsilon): \quad D_0^2 u_1 + |f_2| u_1 = -2D_0 D_1 u_0 - 2|f_1| D_0 u_0 + F\cos(\sqrt{|f_2|}T_0 + \sigma\sqrt{|f_2^{-1}|}T_1) - \alpha u_0^3 \tag{6.40}$$

$$- 2\beta(u_0(D_0 u_0)^2 + D_0^2 u_0 u_0^2).$$

The solution of the first order equation, Equation (6.39), can be written as

$$u_0 = A(T_1)e^{i\sqrt{|f_2|}T_0} + \bar{A}(T_1)e^{-i\sqrt{|f_2|}T_0}. \tag{6.41}$$

Substituting Equation (6.41) into Equation (6.40) and eliminating the secular terms yield

$$-2i\sqrt{|f_2|}D_1 A - 2i|f_1|\sqrt{|f_2|}A + \frac{F}{2}e^{i\sigma\sqrt{|f_2^{-1}|}T_1} - (3\alpha - 4\beta|f_2|)A^2\bar{A} = 0. \tag{6.42}$$

To construct the modulation equations, we substitute Equation (6.24) into Equation (6.42), then separate the real and imaginary parts of the outcome to obtain

$$\sqrt{|f_2|}a\prime = -(|f_1|\sqrt{|f_2|})a + \frac{F}{2}\sin\gamma, \tag{6.43a}$$

$$\sqrt{|f_2|}a\gamma\prime = \frac{(\Omega^2 - |f_2|)}{2}a - \left(\frac{3\alpha}{8} - \frac{|f_2|\beta}{2}\right)a^3 + \frac{F}{2}\cos\gamma, \tag{6.43b}$$

where $\gamma = \sigma\sqrt{|f_2^{-1}|}T_1 + \beta$. Now, substituting $T_1 = \epsilon t$ into Equations (6.43), then setting the bookkeeping parameter ϵ equal to 1 yields

$$\sqrt{|f_2|}\dot{a} = -(|f_1|\sqrt{|f_2|})a + \frac{F}{2}\sin\gamma, \tag{6.44a}$$

$$\sqrt{|f_2|}a\dot{\gamma} = \frac{(\Omega^2 - |f_2|)}{2}a - \left(\frac{3\alpha}{8} - \frac{|f_2|\beta}{2}\right)a^3 + \frac{F}{2}\cos\gamma, \tag{6.44b}$$

where the dot denotes derivative with respect to time, t. For the steady-state response, $\dot{a} = \dot{\gamma} = 0$. It follows from Equations (6.44a) and (6.44b) that

$$f_1^2|f_2|a_0^2 + \left(\frac{(|f_2| - \Omega^2)}{2}a_0 - \left(\frac{3\alpha}{8} - \frac{|f_2|\beta}{2}\right)a_0^3\right)^2 = \frac{F^2}{4}, \tag{6.45}$$

and

$$\tan\gamma_0 = \frac{|f_1|\sqrt{|f_2|}a_0}{\frac{(|f_2|-\Omega^2)}{2}a_0 - \left(\frac{3\alpha}{8} - \frac{|f_2|\beta}{2}\right)a_0^3}, \tag{6.46}$$

where a_0 and γ_0 are, respectively, the steady-state amplitude and phase of the response.

Setting α and β equal to zero in Equations (6.45) and (6.46), one expect to obtain the linear steady-state amplitude and phase of the response as given by Equations (6.9) and (6.11). Therefore, f_1 and f_2 are determined by enforcing the linear steady-state amplitude and phase obtained via Equations (6.45) and (6.46) to equal those acquired via the linear solution. Imposing these conditions, we obtain

$$\begin{aligned} f_2 &= \omega_n^2 + (-1)^j K\frac{d^j}{d\tau^j}[\cos(\Omega\tau)], \\ f_1 &= \frac{1}{2\sqrt{|f_2|}}(2\mu\Omega - (-1)^j K\frac{d^j}{d\tau^j}[\sin(\Omega\tau)]) \qquad j = 0, 1, 2. \end{aligned} \tag{6.47}$$

As one would expect, for small values of K and σ, f_2 approaches ω_n^2 and f_1 approaches μ. It follows from Equation (6.47) that the effective damping and nonlinearity can be written

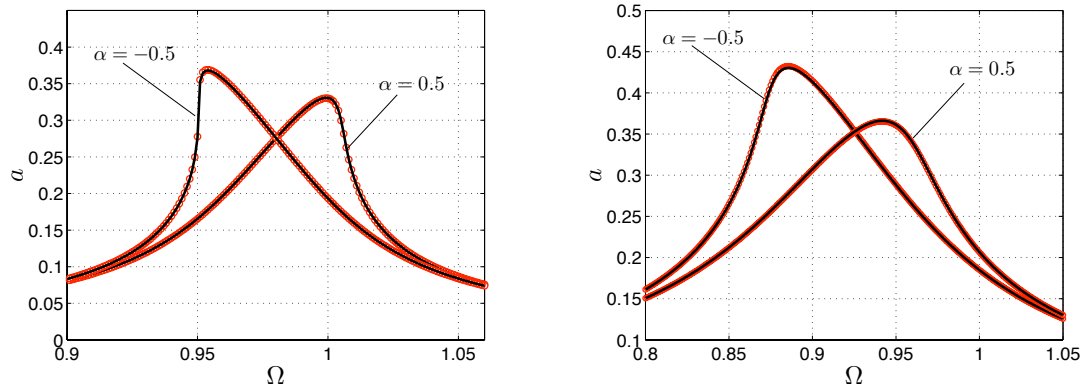

Figure 6.4: Nonlinear frequency-response curves obtained using the Method of Harmonic Balance (circles) and the modified perturbation solution (solid lines). Results are obtained for a) $K = 0.05, \tau = 0.2\pi, j = 2, \beta = 0$, and $F = 0.013$; and b) $K = 0.2, \tau = 0.2\pi, j = 2, \beta = 0$, and $F = 0.04$.

as

$$\mu_{eff} = \frac{(\mu\Omega - (-1)^j \frac{K}{2} \frac{d^j}{d\tau^j}[\sin(\Omega\tau)])}{\sqrt{|f_2|}}, \; N_{eff} = \frac{3\alpha}{8} - \frac{\omega_n^2 + (-1)^j K \frac{d^j}{d\tau^j}[\cos(\Omega\tau)]}{2}\beta, \; j = 0, 1, 2. \tag{6.48}$$

When compared to Equations (6.26) and (6.27), the new expressions for μ_{eff} and N_{eff} reflect the dependance of the response amplitude on the delayed state which, in turn, is a function of the excitation frequency, Ω, that can be far from, ω_n. As such, even when the peak frequency is not close to ω_n, the modified approach can still predict the nonlinear response with significant accuracy.

To assess the stability of the resulting solutions, we find the eigenvalues of the Jacobian of the modulation equations evaluated at the roots (a_0, γ_0). These eigenvalues can be obtained by solving the following characteristic equation:

$$s^2 + |\mu_{eff}|s + \mu_{eff}^2 + \frac{1}{|f_2|}\left(\frac{|f_2| - \Omega_n^2}{2} - N_{eff}a_0^2\right)\left(\frac{|f_2| - \Omega_n^2}{2} - 3N_{eff}a_0^2\right) = 0. \tag{6.49}$$

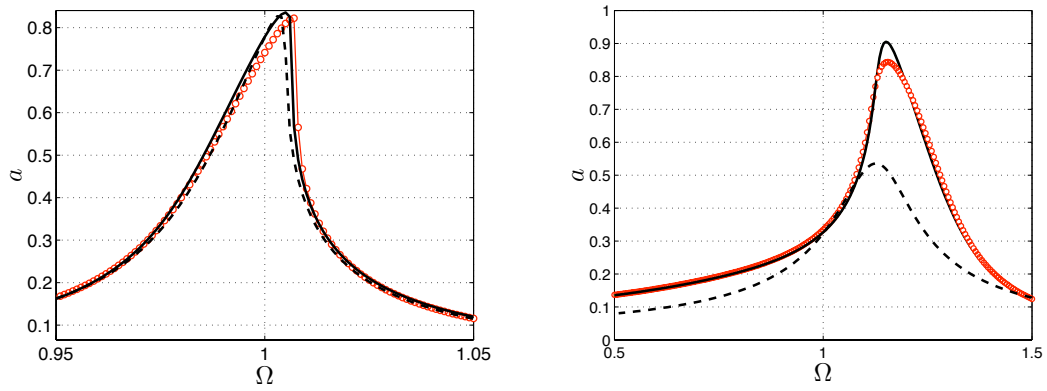

Figure 6.5: Nonlinear frequency-response curves obtained using the Method of Harmonic Balance (circles), the modified perturbation solution (solid line), and the direct approach (dashed lines). Results are obtained for a) $K = 0.02$, $\tau = 0.1\pi$, $F = 0.014, \alpha = 0.69, \beta = 0.48$, and $j = 2$; and b) $K = 0.3$, $\tau = 0.8\pi$, $F = 0.1, \alpha = 0.69, \beta = 0.48$, and $j = 2$.

Again, by virtue of the Routh-Hurwitz criterion the roots (a_0, γ_0) are asymptotically stable, if and only if

$$|\mu_{eff}| > 0, \qquad \mu_{eff}^2 + \frac{1}{|f_2|}\left(\frac{|f_2| - \Omega_n^2}{2} - N_{eff}a_0^2\right)\left(\frac{|f_2| - \Omega_n^2}{2} - 3N_{eff}a_0^2\right) > 0. \quad (6.50)$$

In Fig. 6.4, we validate the modified perturbation solution by comparing the frequency-response curves to solutions acquired via the Method of Harmonic Balance. To illustrate the superiority of the modified approach, we first generate the frequency-response curves for the same parameters utilized to generate Fig. 6.3. It is evident that the modified approach yields results that are almost indistinguishable from those obtained using the harmonic balance. It is also clear that the methodology closely predicts the frequency-response curves even for large values of K and is capable of capturing the effect of damping and nonlinearity on the amplitude of the response.

We also compare the modified approach to the traditional approach and the Method of Harmonic Balance for nonzero values of β, Fig. 6.5. Again, it is obvious that for small values of K, the three solutions are extremely close as expected. However, for larger gains,

the traditional approach, dashed lines in Fig. 6.5(b), qualitatively misrepresents the actual response behavior.

Primary Resonance of A Duffing Oscillator with Delayed Feedback

As a first example, we utilize the modified approach to analyze the effect of gain and delay variations on the primary resonance of a duffing oscillator with feedback delays. To that end, we set $\beta = 0$ in the modulation equations and analyze the response for different values of j, K, and τ.

First, we consider the delayed-acceleration feedback, i.e., $j = 2$ and study variation of the first peak frequency with K and τ as depicted in Fig. 6.6(a). When $K = 0$, and regardless of the delay value, Ω_{p1} is equal to ω_n. Increasing K for and value of $\tau \leq 0.6\pi$ shifts the peak frequency towards smaller values. As a result, large-amplitude responses shift towards smaller values of Ω. For large delays however, e.g. $\tau > 0.6\pi$, the first peak frequency increases as the gain is increased, thereby large-amplitude responses shift towards larger values of Ω. The frequency-response curves generated at $K = 0.3$ and shown in Fig. 6.6(c) also demonstrate these findings.

Figure 6.6(b) displays variation of the effective damping associated with the peak frequencies with the gain, K, for different delays. Since for a given gain-delay combination, large amplitude motions occur near the associated peak frequency, the effective damping was quantified by evaluating μ_{eff} at Ω_{p1}. As expected, for $K = 0$ and any given delay, μ_{eff} approaches μ. As the gain increases, τ determines variation of μ_{eff}. For $\tau \leq 0.6\pi$, the effective damping increases with the gain. Surprisingly, the effective damping continues to increase even when the chosen gain-delay combination approaches the stability boundary of the equilibrium solutions of the free response. This trend can be misunderstood because it suggests that the free response does not lose stability when the gain-delay combination (K, τ) approaches that at the boundary ($\hat{K}$, $\hat{\tau}$). However, one has to realize that by evaluating μ_{eff} at Ω_{p1}, we are only quantifying the amount of damping associated with first peak frequency which in turn is related to the first delay frequency, ω_{d1}. As such,

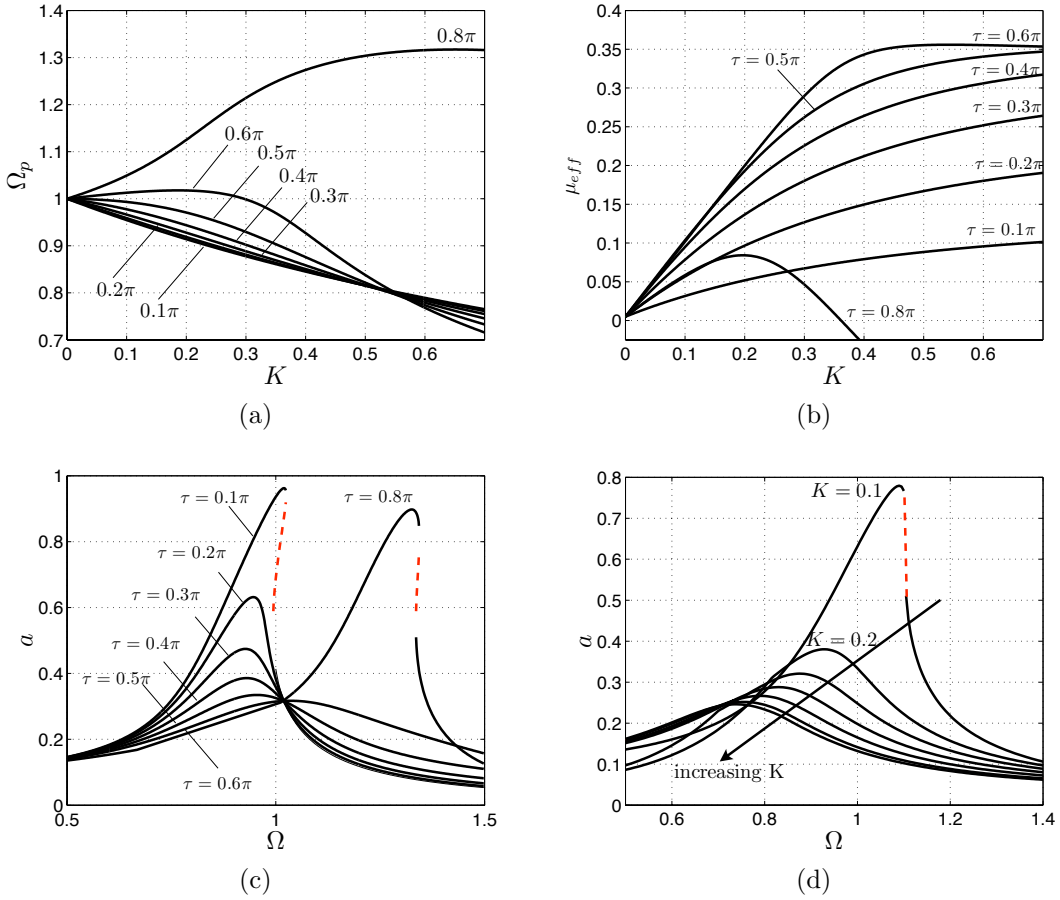

Figure 6.6: (a) Variation of the first peak frequency, Ω_{p1} with the gain K for different delays. (b) Variation of the effective damping, μ_{eff}, with the gain K for different delays. (c) Nonlinear frequency-response curves obtained at $K = 0.3$ using the modified perturbation approach. (d) Nonlinear frequency-response curves obtained at $\tau = 0.4\pi$ using the modified perturbation approach. Results are obtained for $j = 2$, $\alpha = 0.5, \beta = 0$, and $F = 0.1$. Dashed lines represent unstable solutions.

the continuous increase of the effective damping associated with the first peak frequency only implies that the damping associated with the first delay frequency is increasing. Since delay systems have infinite number of frequencies, this does not by any means, prevent the damping associated with another delay frequency from approaching zero at the stability boundaries. This fact will also be discussed later in this section.

For $\tau = 0.8\pi$, μ_{eff} increases initially as the gain is increased. However, when the gain approaches $K \approx 0.18$, μ_{eff} associated with the first peak frequency decreases approaching

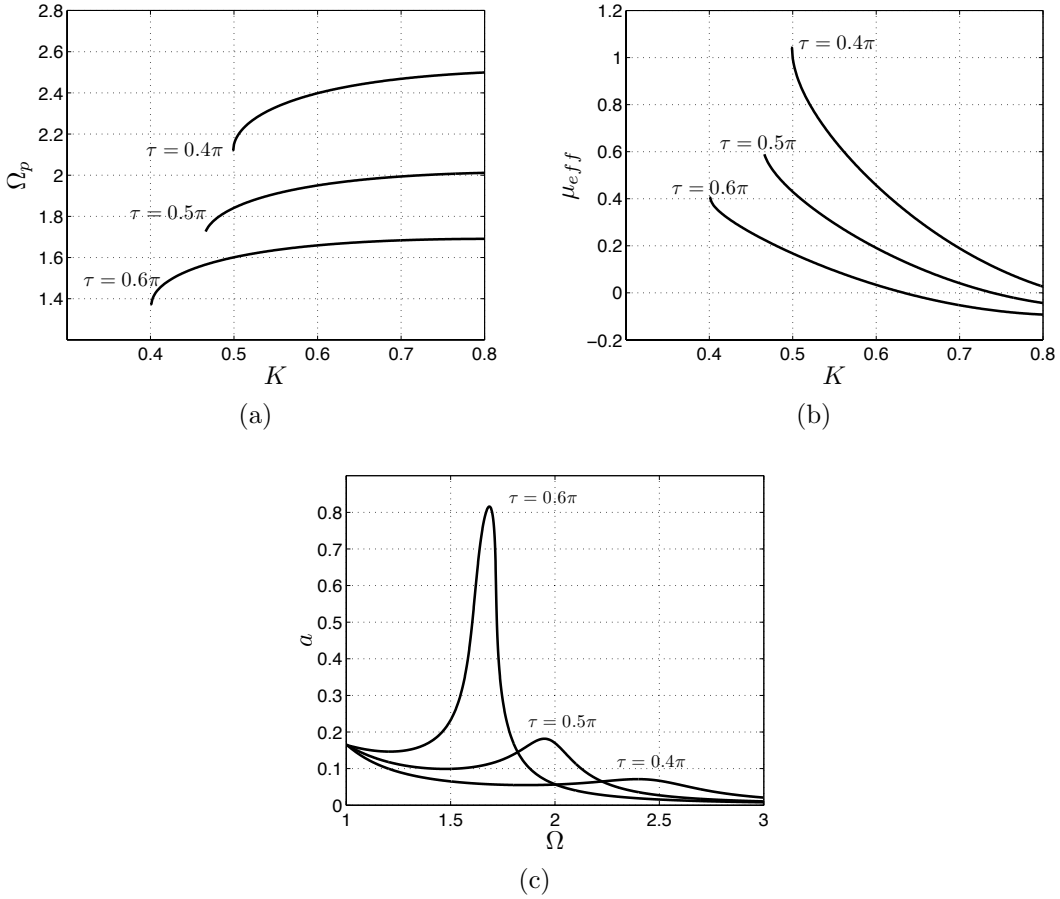

Figure 6.7: (a) Variation of the second peak frequency, Ω_{p2} with the gain K for different delays. (b) Variation of the effective damping, μ_{eff}, with the gain K for different delays. (c) Nonlinear frequency-response curves obtained at $K = 0.6$ and $F = 0.1$ using the modified perturbation approach. Results are obtained for $j = 2$, $\alpha = 0.5$, and $\beta = 0$.

zero near $K \approx 0.37$. In this situation, the equilibrium solutions of the free response lose stability through the first delay frequency. Such conclusion can also be confirmed by examining Fig. 6.1(c) and noting that at $\tau/T = 0.4$ or equivalently $\tau = 0.8\pi$, the equilibrium solutions lose stability near $K = 0.37$.

Figure 6.6(c) displays the frequency-response curves generated near the first peak frequency for $K = 0.3$ and different delays. For $\tau = 0.1\pi$, the response has a hardening-type behavior, large amplitude motions, and regions of multivalued solutions. As the delay is increased towards $\tau = 0.2\pi$, the amplitude of the response drops and slightly shifts towards

larger values of Ω. The drop in the amplitude is attributed to the increase in the effective damping as illustrated in Fig. 6.6(b). Increasing the delay further towards $\tau = 0.3\pi$ yields a smaller peak and additional shift in the peak frequency. The same behavior continues until the delay approaches $\tau = 0.6\pi$. Beyond this values (e.g., at $\tau = 0.8\pi$), the response amplitude increases significantly and the frequency-response curves shift suddenly towards larger values of Ω. This is due to a sudden shift in the peak frequency and a significant decrease in the effective damping as illustrated in Figs. 6.6(a) and 6.6(b).

Figure 6.6(c) displays the frequency-response curves near the first peak frequency for increasing gains and a constant delay, $\tau = 0.4\pi$. As evident from Fig. 6.6(a), when the gain is small, e.g. $K = 0.1$, the peak frequency occurs very close to ω_n. The amplitude of the response is large and exhibits hysteretic jumps. As the gain is increased towards $K = 0.2$, the response-amplitude drops significantly due to a significant increase in the effective damping, Fig. 6.6(b). In addition, the region of multivalued solutions disappears and the peak frequency shifts towards smaller values of Ω. As the gain is increased further, the effective damping continues to increase and the amplitude of the response continues to drop.

As discussed previously, for a given gain and $\tau \leq 0.6\pi$, the equilibrium solutions do not seem to lose stability through the first delay frequency as evident from the continuous increase in the effective damping associated with that frequency. Consequently, the modified approach should be capable of predicting a decrease in the effective damping associated with some other frequency. To illustrate this fact, we display variation of the second-peak frequency and its associated effective damping with the gain for three delay values in Figs. 6.7(a) and 6.7(b). Figure 6.7(b) demonstrates that, for a given delay, μ_{eff} associated with the second-peak frequency decreases and approaches zero as the gain is increased. For instance, for $\tau = 0.6\pi$, the effective damping decreases with the gain and approaches zero at $K \approx 0.63$. This represents the same gain-delay combination at which the free response loses stability in Fig. 6.1(c).

Fig. 6.7(b) demonstrates that the effective damping decreases as the delay is increased. This is also reflected in the frequency-response curves depicted in Fig. 6.7(c). At $\tau = 0.6\pi$,

the response exhibits very large amplitude which decreases significantly as the delay is decreased.

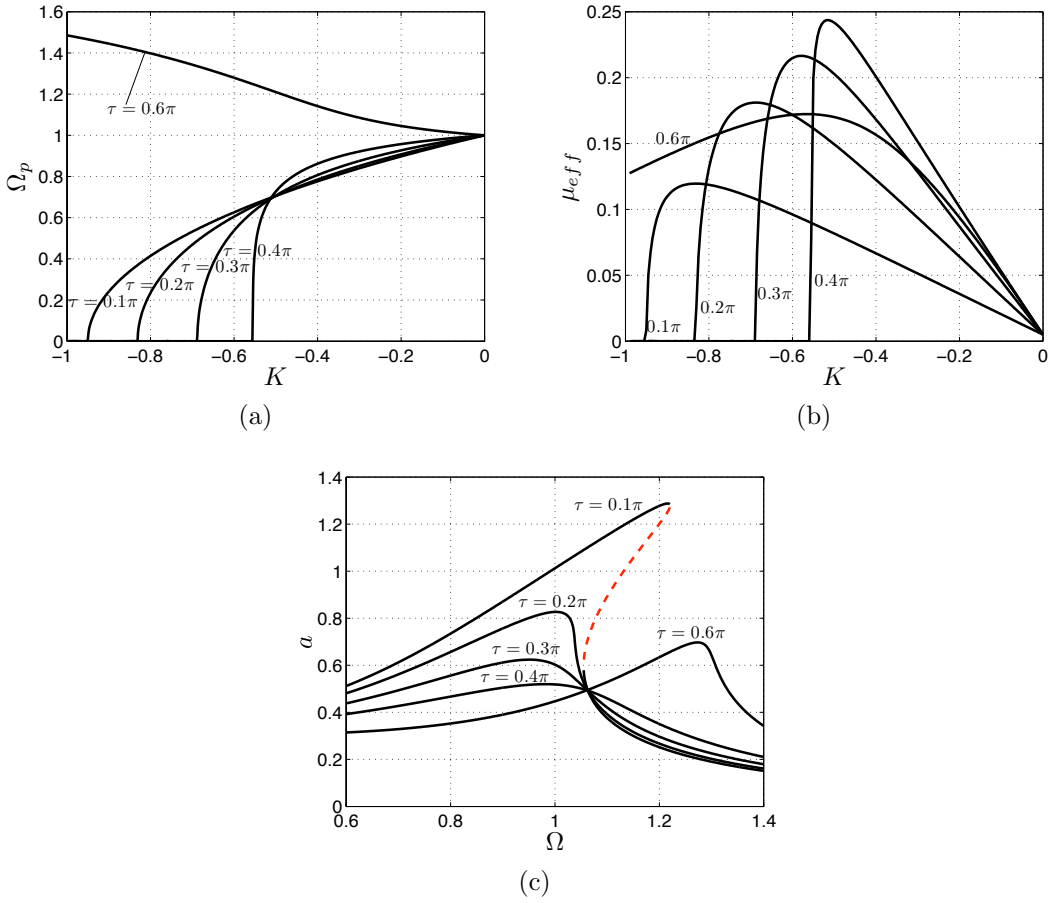

Figure 6.8: (a) Variation of the first peak frequency with the gain K for different delays. (b) Variation of the effective damping with the gain K for different delays. (c) Nonlinear frequency-response curves obtained at $K = -0.4$ and $F = 0.2$ using the modified perturbation approach. Results are obtained for $j = 0$, $\alpha = 0.5$, and $\beta = 0$.

Next, we study the primary resonance of the duffing oscillator when $j = 0$ (delayed-position feedback). Figure 6.8(a) displays variation of the first peak frequency with the gain for different time delays. For $K = 0$ and any time delay, Ω_{p1} approaches $\omega_n = 1$. When $\tau < 0.6\pi$, increasing the gain causes the first peak frequency to decrease approaching zero at a critical value. This implies that the first peak frequency no longer exists. At these gains, the associated effective damping also approaches zero, Fig. 6.8(b). It is worth

noting that, increasing the gains beyond these critical values, does not cause the effective damping to cross zero. Hence, by approaching zero, the effective damping only indicates that Ω_{p1} has vanished and by no means reflect that the equilibrium solutions of the free response lose stability at these gains. Figure 6.8(c) displays the frequency-response curves for the case $K = -0.4$ and different time delays.

Primary Resonance of A Delayed System with Geometric and Inertia Nonlinearities

For a duffing oscillator, the effective nonlinearity does not seem to be influenced by the presence of delay in the linear feedback as evident from Equation (6.48). However, when the inertia nonlinearities are present, $\beta \neq 0$, the effective nonlinearity becomes a function of the gain, delay, and the excitation frequency.

We study the effect of the inertia nonlinearities on the response behavior by investigating the frequency-response characteristics. Figure 6.9(a) displays variation of the steady-state response amplitude with the excitation frequency for different time delays. For the purpose of comparison, the curves are generated for the same gain-delay values used earlier in Fig. 6.7(c). For $\tau = 0.1\pi$, the frequency-response curve exhibits a hardening behavior because the effective nonlinearity is positive as shown in Fig. 6.9(b). As the delay is increased, the response amplitude drops because of the increase in the effective damping. In addition, the response becomes less and less hardening because the magnitude of the effective nonlinearity decreases. As the delay is increased to $\tau = 0.8\pi$, the behavior of the frequency-response curve switches to the softening type.

This behavior can also be deduced by examining Fig. 6.9(b) which displays variation of the effective nonlinearity coefficient with the gain for different delays. To quantify the effective nonlinearity near a given peak frequency, N_{eff} is evaluated at Ω_p. For $K = 0$ and our choice of α and β, N_{eff} is positive and the response is clearly hardening. As the gain is increased, the delay determines the nonlinear response behavior. For small delays, e.g., when $\tau < 0.1\pi$, the effective nonlinearity remains positive and increases as the gain is

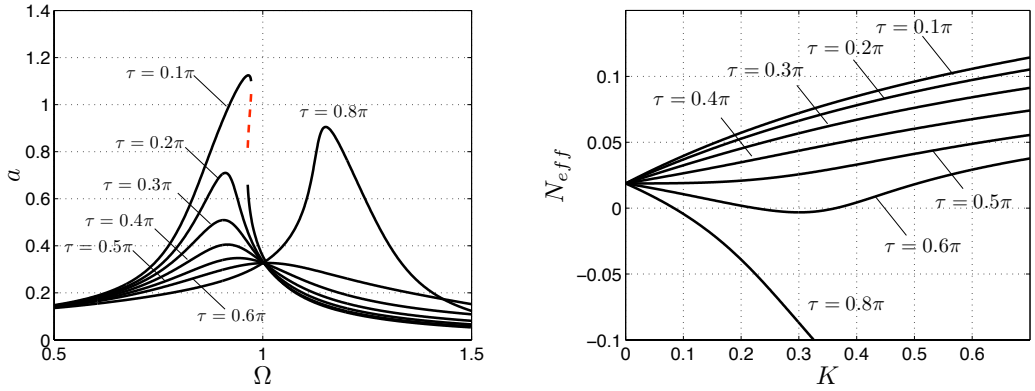

Figure 6.9: (a) Nonlinear frequency-response curves obtained at $K = 0.3$ and $F = 0.1$ using the modified perturbation solution. (b) Variation of the effective nonlinearity coefficient with the gain K . Results are obtained for $j = 2$, $\alpha = 0.69, \beta = 0.48$, and $F = 0.1$. Dashed lines represent unstable solutions.

increased. For $\tau = 0.6\pi$ however, the effective nonlinearity decreases initially and becomes negative within the range $0.22 < K < 0.38$ where the frequency response curves exhibit a softening behavior. As the gain is increased further, the effective nonlinearity increases and becomes positive. As such, the response regains its hardening characteristics. For $\tau = 0.8\pi$, the effective nonlinearity decreases as the gain is increased and is positive only for very small gains, $K < 0.08$.

It is quite interesting to demonstrate that a linear-delayed feedback is capable of altering the nonlinear characteristics of the response. For example, by a proper choice of the gain and delay, it is possible to make the effective nonlinearity approach zero. This entails that, in a local sense, a nonlinear system can be linearized using a linear feedback. Such idea could find interesting applications in nonlinear control theory especially in feedback linearization.

Chapter 7

Conclusions and Future Work

7.1 Augmentation of Low-pass Filters into Time-Delay controllers to Suppress Vibrations in Multi-Degree-of-Freedom and Structural Systems Using a Single-Input Single-Output Control Approach

In Chapters 3 and 4, we evaluated the prospectus of purposefully augmenting filters to enhance the stability margins of delayed-feedback algorithms utilized for mitigating vibrations of single-, multi-degree-of-freedom, and structural systems. Specifically, we investigated the effect of augmenting a Butterworth low-pass filter (BLPF) on the performance of a delayed-position feedback algorithm by studying the influence of the filter's order and cut-off frequency on the stability margins in the controller's gain-delay domain. It was observed that, in the case of single-degree-of-freedom systems, as the order of the filter is increased, the stable pockets shift to the left along the delay axis causing the largest stability pocket to shrink significantly adversely affecting the stability margins of the controller.

This was attributed to the filter's inherent delay. In the case of multi-degree-of-systems, increasing the filter's order resulted in two distinct shifts. Again, the first shift reduces the size of the first stability pocket due to the filter's inherent delay. The second, on the other hand, rejects the unstable pockets introduced by the higher modes from the stability maps. This, in turn, has the influence of increasing the stability margins of the controller. As such, it was concluded that a proper BLPF can aid in enhancing the stability margins of delayed-feedback controllers applied to multi-degree-of-freedom systems. However, it was also noted that a high-order BLPF can lower the effective damping of the controller for the same controller gains. Therefore, a balance between increasing the stability margins in the gain-delay space and the effective damping should always be sought.

To validate these findings, the controller is experimentally implemented on two structural systems whose system's model can be described by a set of linearly-uncoupled ordinary differential equations. In the first experiment, a filter-augmented delayed-position feedback algorithm is applied to mitigate the multi-modal vibrations of a macrocantilever beam using a piezoelectric patch and a laser sensor. First, the effect of the filter order and cut-off frequency on the stability pockets was evaluated experimentally showing excellent agreement with the theoretical findings. Subsequently, and using a single gain-delay combination, the controller was shown to be capable of rejecting external disturbances and significantly reducing the beam vibrations under persistent harmonic excitations.

In the second case study, a filter-augmented delayed-velocity feedback algorithm is applied to mitigate the multi-modal vibrations of a microcantilever sensor. Throughout several experimental studies, it was successfully illustrated that, system's delays which are prevalent at the microscale may be augmented into a larger delay period, which when combined with a proper velocity-feedback gain and a proper filter, can be utilized as an effective mechanism for vibration mitigation at the micro-scale.

7.2 Implementation of Filter-Augmented Delayed-Feedback Algorithms on a Structural System Which Can Only be Represented by a Set of Linearly-Coupled ODEs

In Chapter 5, we took the implementation of delayed-feedback algorithms on structures one step further by investigating their performance on a continuous system that can only be discretized into a set of linearly-coupled ordinary differential equations (ODEs). As an example, we considered the problem of suppressing the coupled flexural-torsional oscillations of a cantilever beam with an asymmetric tip rigid body using a single piezoelectric patch and a single laser sensor. Following Euler-Bernoulli's beam theory, we developed and validated a system model consisting of two PDEs and the associated boundary conditions. To implement the controller and analyze the stability of the closed-loop system, we reduced the resulting system of PDEs and boundary conditions into a set of linearly-coupled ODEs using a Galerkin discretization scheme.

Once the model was obtained, validated, and discretized, we turned our attention into investigating the stability of the closed-loop system in the gain-delay space and in the presence of low-pass filters. Towards that end, we utilized a technique that involves transforming the resulting set of Delay Differential Equations (DDEs) into an equivalent PDE followed by a numerical discretization of the PDE in the delay space using the method of lines. The resulting set of N ODEs was then utilized to obtain the first approximate N eigenvalues of the closed-loop system. This technique reduced the computational intensity required to solve a large set of transcendental equations numerically and allowed us to treat a problem with a large number of coupled modal equations. For the problem at hand, it was observed that $N = 40$ lines are necessary to accurately approximate the first two stability pockets of the controller. Additionally, this numerical approach allowed us, for the first time, to generate damping contours within the stability pockets to facilitate obtaining the controller's optimal gain delay combinations.

Using the resulting stability maps, we investigated theoretically and experimentally the effectiveness of the controller in rejecting external disturbances and suppressing large-amplitude oscillations resulting from initial conditions and harmonic-base excitations for different tip rigid bodies, filters, and piezoelectric patch orientations. It was observed that a BLPF filter aids in rejecting the influence of the higher destabilizing vibration modes from the feedback, thereby yielding larger regions of stability in the gain-delay space. This has the influence of increasing the robustness of the controller to parameter's uncertainties, but comes at the expense of reducing the effective damping of the controller.

Using several gain-delay combinations from the developed stability maps based on a three-mode approximation, it was clearly observed that the controller is capable of rejecting external disturbances and reducing the settling time significantly even when it was implemented on a seven-mode reduced-order model or, experimentally, on the infinite-dimensional structure. This was only possible when a proper BLPF filter is implemented in the feedback. Without a filter, the stability pockets shrink significantly making it almost impossible to find a gain-delay combination that stabilizes all modes simultaneously.

The influence of orientating the piezoelectric patch at different angles was also investigated theoretically. It was observed that when the orientation angle is increased from 0^o to 45^o with respect to the horizontal axis of the beam, larger controller gains were necessary to destabilize the closed-loop system for the same controller delay. This was attributed to the distribution of the control effort between torsion and bending as the angle is varied. However, when comparing the effectiveness of the controller in rejecting initial conditions using different orientation angles, it was observed that, gain-delay combinations that produce similar effective damping in the system, yield almost similar response behavior in torsion and bending regardless of the angle. The only difference is that the control effort is significantly reduced when the patch is oriented at $45°$ angle with respect to the horizontal axis. A result that corroborates previous research efforts on the coupled flexural-bending response of beams which indicate that $45°$ is the optimal angle for enhanced controller's performance [117].

Finally, an experimental verification of the theoretical results was carried out in the labo-

ratory to illustrate the controller's performance in rejecting harmful structural vibrations. In all experiments, a piezoelectric patch oriented at zero angle and only bending feedback were utilized. In the first scenario, the tip-loaded beam was subjected to impulse loadings using an electrodynamic shaker. Experimental results clearly indicated that a delayed-feedback controller augmented with a proper BLPF filter and a proper gain-delay combination can effectively reject external disturbances and reduce the settling time without destabilizing the higher vibration modes. In the second scenario, the tip-loaded beam was subjected to harmonic base inputs with an excitation frequency near the first, second, and third modal frequencies of the coupled system. It was observed that the controller is capable of reducing the steady-state response amplitude (torsion and bending) significantly near the first two bending-dominated modes using the same gain-delay combination. Near the third torsion-dominated mode, the controller was not effective in reducing the response amplitude but did not destabilize the response either. We believe that this might be attributed to either saturation of the controller input or the orientation of the piezoelectric patch.

7.3 Primary Resonances of Weakly-Nonlinear Delay Systems

In Chapter 6, we presented a modified multiple scaling perturbation approach that allows for investigating primary resonances of weakly nonlinear delay systems with arbitrarily large coefficients of the delayed states. When these coefficients are large, the frequency-response of the system can exhibit a large number of peak frequencies that are not necessarily close to the natural frequency of the system. Under such conditions, direct implementation of the method of multiple scales as demonstrated previously in [54, 55] is incapable of predicting the qualitative behavior of the response near different peak frequencies. This is due to the inability of the traditional approach to account for large deviations between the response (peak) frequency and the system's natural frequency. The modified approach, on the other hand, extracts the delays from the linear states and lumps them

into unknown damping and stiffness functions. These functions are then determined by equating the linear solution acquired via the Method of Multiple Scales to that obtained by directly attacking the linear problem. This, in turn, permits resolving the response characteristics near frequencies that are far from the system's natural frequency. After verifying the steady-state solutions attained via the modified procedure against solutions obtained using the Method of Harmonic Balance, we utilized the modified approach to study primary resonances of a delayed duffing oscillator and a weakly nonlinear system with geometric and inertia nonlinearities. Analytical results clearly illustrated that the modified procedure can capture the effective damping, frequency-response characteristics, effective nonlinearity, and stability near the multiple peak frequencies. They also demonstrated that the nonlinear response can exhibit completely different characteristics near different delay frequencies.

7.4 Recommendations for Future work

Based on the conclusions of this Dissertation, we believe that future research efforts should be aimed to several directions that include:

- Implementation of filter-augmented delayed-feedback control algorithm along with adaptive control techniques to change the gain-delay combinations in real time based on the damping contours mentioned in Chapters 2, 3, and 4. This will allow the controller to always maintain maximum damping as the design parameters or the environmental conditions are varied.

- Extending the current approach into the Multi-Input Multi-Output (MIMO) scenario especially when the purpose is to control multiple flexural and torsional modes simultaneously. The controller performance can then be assessed through application on an actual system, e.g., a wind turbine blade or an aircraft wing.

- Generalization of the proposed filter-augmented delayed-feedback control algorithms to suppress oscillations in two-dimensional plates while paying more attention to

the influence of the piezoelectric patch location and orientation as well as sensor's location on the resulting stability maps.

- Extending the implementation of the modified Method of Multiple Scales to systems containing other types of nonlinearities as well as nonlinear delayed feedback. Additionally, experimental observation of the nonlinear resonant response near the multiple delay frequencies mentioned in Chapter 6 is essential.

Bibliography

[1] MikroMasch Inc. Csc17/cr-au microcantilever's manual, 2009.

[2] S. l. Niculescu. *Delay Effects on Stability: A Robust Control Approach.* Springer-Verlag, London, 2001.

[3] B. Lehman and E. I. Variest. Stability of a Continuous Stirred Reactor with Delay in the Recycle Steams. In *Proceedings of the 30th IEEE Conference of Decision and Control*, pages 1875–1876, Brighton, England, 1991.

[4] B. Lehman. Stability of Chemical Reactions in a CSTR with Delayed Recycle Streams. In *Proceedings of the 1994 American Control Conference*, pages 3521–3522, Baltimore, MD, 1994.

[5] J. S. Ansary. Stability of Differential-Difference Equations Representing Heat Exchangers and Certain Other Systems. *International Journal of Control*, 17:193–198, 1973.

[6] A. M. Annaswamy, O. El-Rifai, M. Fleifil, J.P. Hathout, and A.F. Ghoniem. A Model-Based Self-Tuning Controller for Thermoacoustic Instability in Premixed Combustors. *Combustion Science and Technology*, 135:213–240, 1998.

[7] P. Langhorne, A.P. Dowling, and N. Hooper. Practical Active Control System for Combustion Oscillations. *Journal of Propulsion and Power*, 6:324–333, 1990.

[8] P. A. Ioannou and C. C. Chien. Autonomous Cruise Control. *IEEE Transactions of Vehicular Technology*, 42:657–672, 1993.

[9] K. Pasino. A Mixture of Intelligent and Conventional Control Methods Maybe the Best Way to Implement Autonomous Systems. *IEEE Spectrum*, 32:55–62, 1995.

[10] P. Varaiya. Smart Cars on Smart Roads: Problems of Control. *IEEE Transactions of Automatic Control*, 38:195–207, 1993.

[11] C. M. Marcus and R. M. Westervelt. Stability of Analog Neural Networks with Delay. *Physical Review A*, 39:347, 1989.

[12] H. Logemann and R. Rebaber. The Effect of Small Time-Delays on Closed-Loop Stability of Boundary Control Systems. *Mathematics of Control, Signals, and Systems*, 9:123–151, 1996.

[13] H. Logemann and S. Townley. The Effect of Small Delays in the Feedback Loop on the Stability of Neutral Systems. *Systems and Control Letters*, 27:267–274, 1996.

[14] N. MacDonald. Time Delays in Prey Predator Models. *Mathematical Biosciences*, 28:321–330, 1976.

[15] N. MacDonald. *Biological Delay Systems: Linear Stability Theory.* Cambridge University Press, Cambridge, 1989.

[16] K. Gopalsamy. *Stability and Oscillations in Delay Differential Equations of Population Dynamics.* Kluwer Academic Publishers, London, 1992.

[17] K. Ross. *The Prevention of Malaria.* Second Edition, London: John Murray, 1911.

[18] A. J. Lotka. Contributions to The Analysis of Malaria Epidemiology:I General Part. *Supplement to American Journal of Hygiene*, 3:1–37, 1923.

[19] V. Volterra. Variazioni et Fluttuazioni del Numero D'individuali in Specie Animali Conviventi. *R. Comitato Talassografico Memoria*, 131:1–142, 1927.

[20] N. Minorski. Self-Excited Oscillations in Dynamical Systems Possessing Retarded Actions. *Journal of Applied Mechanics*, 9:65–71, 1942.

[21] K. Gu, V. Kharitonov, and Ji Chen. *Stability of Time-Delay Systems.* Birkhauser, 2003.

[22] G. Stepan. *Retarded Dynamical Systems: Stability and Characteristic Function.* Wiley, New York, 1989.

[23] E. W. Kamen. *Lectures on Algebraic Systems Theory: Linear Systems over Rings.* NASA contractor report. 3016, 1978.

[24] S. D. Brierley, J. N. Chiasson, E. B. Lee, and S. H. Zak. On Stability Independent of Delay for Linear Systems. *IEEE Transactions on Automatic Control*, AC-27:252–254, 1982.

[25] J. N. Chiasson, S. D. Brierley, and E. B. Lee. A Simplified Derivation of the Zeheb-Walach 2-D Stability Test with Application to Time-Delay Systems. *IEEE Transactions on Automatic Control*, AC-30:411–414, 1985.

[26] D. Hertz, E. J. Brierley, and E. Zeheb. Stability Independent and Dependent of Delay for Delay Differential Systems. *Journal of Franklin Institute*, 318(3), 1984.

[27] Z. V. Rekasius. Proceedings of Joint Automatic Control Conference. In *Paper No. TP9-A*, 1980.

[28] K. Walton and J. E. Marshall. Direct Method for TDS Stability Analysis. *Proceeding of The IEE, Part D*, 134(2), 1987.

[29] J. Chen, G. Gu, and C. N. Nett. A New Method for Computing the Delay Margins for Stability of Linear Delay Systems. *Systems and Control Letters*, 26(2), 1995.

[30] K. Gu. Discretized LMI set in The Stability Problem of Linear Uncertain Time-Delay Systems. *International Journal of Control*, 68:923–934, 1997.

[31] F. M. Asl and A. G. Ulsoy. Analysis of A System of Linear Delay Differential Equations. *Journal of Dynamic Systems, Measurement, and Control*, 125:215–223, 2003.

[32] A. H. Nayfeh and D. T. Mook. *Nonlinear Oscillations.* Wiley-Interscience, New York, 1979.

[33] N. Jalili and N. Olgac. A Sensitivity Study of Optimum Delayed Feedback Vibration Absorber. *Journal of Sound and Vibration*, 223:567, 1999.

[34] N. Jalili and N. Olgac. Identification and Re-tuning of Optimum Delayed Feedback Vibration Absorber. *AIAA Journal of Guidance, Control, and Dynamics*, 23:961, 2000.

[35] N. Jalili and N. Olgac. Multiple Identical Delayed-Resonator Vibration Absorbers for Multi-Degree-of-Freedom Mechanical Structures. *ASME Journal of Dynamic Systems, Measurements, and Control*, 122:314, 2000.

[36] Z. N. Masoud, A. H. Nayfeh, and A. Al-Mousa. Delayed-Position Feedback Controller for The Reduction of Payload Pendulations On Rotary Cranes. *Journal of Vibration and Control*, 8:1–21, 2002.

[37] Z. N. Masoud, N. A. Nayfeh, and A. H. Nayfeh. Sway Reduction on Container Cranes Using Delayed Feedback Controller: Simulations and Experiments. In *Proceedings of the 19th Biennial ASME Conference on Mechanical Vibrations and Noise*, Chicago, IL, 2003.

[38] Z. N. Masoud, M. F. Daqaq, and N. Nayfeh. Pendulation Reduction on Small Ship Mounted Telescopic Cranes. *Journal of Vibration and Control*, 10(8):1167–1181, 2004.

[39] A. N. Nayfeh, Z. N. Masoud, and W. Bawmann. A Comparison of Three Feedback Controllers for Container Cranes. pages Long Beach, CA, 2005.

[40] N. Olgac, H. Elmali, M. Hosek, and M. Renzulli. Active Vibration Control of Distributed Systems Using Delayed Resonator with Acceleration Feedback. *Journal of Dynamic Systems, Measurement, and Control*, 119:380, 1997.

[41] P. Phohomsiri, F. Udwadia, and H. Von Bremen. Time-delayed Positive Velocity Feedback Control Design for Active Control of Structures. *Journal of Engineering Mechanics*, 132(6):690, 2006.

[42] F. Udwadia, H. Von Bremen, and P. Phohomsiri. Time-Delayed Control Design for Active Control of Structures: Principles and Applications. *Structural Control and Health Monitoring*, 14(27):61, 2007.

[43] C. Abdallah, P. Dorato, J. Benitez-Read, and R. Byrne. Delayed Positive Feedback Can Stabilize Oscillatory Systems. In *Proceedings of the 1993 American Control Conference*, Albuquerque, NM, 1993.

[44] M. Hosek, H. Elmali, and N. Olgac. Tunable Torsional Vibration Absorber: The Centrifugal Delayed Resonator. *Journal of Sound and Vibration*, 205:151, 1997.

[45] R. D. Robinett, B. J. Petterson, and J. C. Fahrenholtz. Lag-Stabilized Force Feedback Damping. *Journal of Intelligent and Robotic Systems*, 21:277–285, 1998.

[46] Ogata K. *Modern Control Engineering*. Prentice-Hall, New Jersey, 2002.

[47] S.O.R. Moheimani and A.J. Fleming . *Piezoelectric Transducers for Vibration Control and Damping*. Springer, Germany, 2006.

[48] L. Meirovitch. *Fundamentals of Vibrations*. McGraw-Hill, New York, NY 10020, 2001.

[49] K. AlHazza, A. H. Nayfeh, and M.F. Daqaq. Delayed-Acceleration Feedback for Active-Multimode Vibration Control of Cantilever Beams. volume 5, pages 729–738, Las Vegas, NV, 2007.

[50] M. Daqaq, C. Bradley, and N. Jalili and K. AlHazza. Feedback Delays for Ultrasensitive Sensing. pages Las Vegas, NV, 2007.

[51] K. Alhazza, A. H. Nayfeh, and M. F. Daqaq. On Utilizing Delayed-feedback for Active-multimode Vibration Control of Beams. *Journal of Sound and Vibration*, 319(3-5):735–752, 2009.

[52] O. Diekmann, S. A. Van Gils, S. M. Verduyn-Lunel, and H. O. Walther. *Delay Equations, Functional, Complex and Nonlinear Analysis Difference Equations*. Springer-Verlag, New York, 1995.

[53] R. E. Bellman and K. L. Cooke. *Differential Difference Equations*. Academic Press, New York, 1963.

[54] H. Hu, E. Dowell, and L. Virgin. Resonance of a Harmonically Forced Duffing Oscillator with Time Delay State Feedback. *Nonlinear Dynamics*, 15:311, 1998.

[55] J. C. Ji and A. Y. T. Leung. Resonances of a Nonlinear SDOF System with Two Time-Delays in Linear Feedback Control. *Nonlinear Dynamics*, 253:985, 2002.

[56] R. W. Stark. Time Delay Q-Control of the Microcantilever in Dynamic Atomic Force Microscopy. In *Proceedings of 2005 5th IEEE Conference on Nanotechnology*, Nagoya, Japan, 2005.

[57] K. Yamasue and T. Hikihara. Control of Microcantilevers in Dynamic Force Microscopy Using Time-Delayed Feedback. *Review of Scientific Instruments*, 77:1–6, 2006.

[58] H. Sadeghian, M. T. Arjmand, H. Salarieh, and A. Alasty. Chaos Control in Single Mode Approximation of T-AFM Systems Using Nonlinear Delayed Feedback Based on Sliding Mode Control. In *Proceedings of the ASME 2007 International Design and Engineering Technical Conference And Computers and Information in Engineering Conference*, Las Vegas, NV, 2007.

[59] M. F. Daqaq, J. Renno, J. Farmer, and D. J. Inman. Effects of System Parameters and Damping on an Optimal Vibration-Based Energy Harvester. In *Proceedings of the AIAA Structure, Structural Dynamics, and Materials Conference.*, Honolulu, HI, 2007.

[60] M.F. Daqaq, K. A. AlHazza, and S. Stanton. Effect of Feedback Delays on Nonlinear Vibrations of Cantilever Beams. pages Las Vegas, NV, 2007.

[61] Y. Qaroush, M. F. Daqaq, R. Saeidpourazar and N. Jalili. Feedback Delays for Vibration Mitigation and External Disturbance Rejection at the Microscale. In *Proceedings of 50th AIAA/ASME/ASCE/AHS/ASC Structures*, Palm springs, CA, 2009.

[62] Y. Qaroush and M. F. Daqaq. Vibration Mitigation in Multi-Degree-of-Freedom Structural Systems Using Filter-Augmented Delayed-Feedback Algorithms. *Smart Materials and Structures*, 19:085016, 2010.

[63] M. F. Daqaq, K. Alhazza and Y. Qaroush. On Primary Resonances of Weakly Nonlinear Delay Systems With Cubic Nonlinearities. *Journal of Nonlinear Dynamics*, pages 1–25, 2010.

[64] A. Bellen and M. Zennaro. *Numerical Methods for Delay Differntial Equations*. Oxford University Press, New York, 2003.

[65] L. Dugard and E. I. Verries. *Stability and Control of Time-delay Systems*. Springer-Verlag, London, 1998.

[66] A. N. Michael, L. Hou, and D. Liu. *Stability of Dynamical Systems Continuous, Discontinuous, and Discrete Systems*. Berkhauser, Boston, 2008.

[67] G. J. Silva, A. Datta , and S. P. Bhattacharyya. *PID Controllers for Time-Delay Systems*. Berkhauser, Boston, 2005.

[68] M. Vajta. Some Remarks on Padé-Approximations. *Mathematical Problems in Engineering*, 8:195–205, 2002.

[69] F. M. Asl and A. G. Ulsoy. Analytical Solution of a System of Homogeneous Delay Differential Equations via the Lambert Function. In *Proceedings of the American Control Conference*, pages 2496–2500, Chicago, IL, 2000.

[70] Y. C. Cheng and C. Hwang. Use of The Lambert W Function for Time-Domain Analysis of Feedback Fractional Delay Systems. In *IEEE Procedings of Control Theory Applications*, pages 4283–4288, Portland, OR, 2006.

[71] S. Yi, A. G. Ulsoy, and P. W. Nelson. Solution of Systems of Linear Delay Differential Equations via Laplace Transformation. *Applied Numerical Mathematics*, 56(3–4):305–317, 2006.

[72] S. Yi and A. G. Ulsoy. Calculation of The Rightmost Characteristic Root of Retarded Time-Delay Systems via Lambert W Function. In *Proceedings of the 2006 American Control Conference*, pages 2433–2438, Minneapolis, MN, 2006.

[73] E. Jarlebring and T. Damm. The Lambert W Function And The Spectrum of Some Multidimensional Time-Delay Systems. *Automatica*, 43(12):2124–2128, 2007.

[74] R. Corless, H. Ding, N. Higham, and J. Jeffrey . The Solution of S exp(S)= A is Not Always the Lambert W Function of A. In *Proceedings of the 2007 International Symposium on Symbolic and Algebraic Computation ISSAC*, pages 116–121, Waterloo, Ontario, Canada, 2007.

[75] F. Asl, P. W. Nelson, and A. G. Ulsoy. Survey on Analysis of Time Delayed Systems via the Lambert W Function. *A Supplement, Advances in Dynamical Systems*, 14(S2):296–301, 2007.

[76] A. Bellen and S. Maset. Numerical Solution of Constant Coefficient Linear Delay Differential Equations as Abstract Cauchy Problems. *Numerische Mathematik*, 84(3):351–74, 2000.

[77] D. Breda, S. Maset, and R. Vermiglio. Pseudospectral Approximation of Eigenvalues of Derivative Operators with Non-Local Boundary Conditions. *Applied Numerical Mathematics*, 56(3):318–331, 2006.

[78] D. Breda. Solution Operator Approximations for Characteristic Roots Of Delay Differential Equations. *Applied Numerical Mathematics*, 56(3–4):305–317, 2006.

[79] S. Maset. Numerical Solution of Retareded Functional Differential Equations as Abstract Cauchy Problems. *Journal of Computational and Applied Mathematics*, 161(2):259–282, 2003.

[80] D. Breda, S. Maset, and R. Vermiglio. Computing the Characteristic Roots for Delay Differential Equations. *IMA Journal of Numerical Analysis*, 24(1):1–19, 2004.

[81] L. D. Pearman. *Design and Analysis of Analog Filters: A Signal Processing Perspective*. Kluwer Academic Publishers, USA, 2001.

[82] W. D. Stanley. *Digital Signal Processing*. Reston Publishing Co., United states of America, 1975.

[83] L. Dugard and E.I. Verrie. *Stability and Control of Time-delay Systems*. Springer-Verlag , London, 1998.

[84] E.N. Gryazina, B.T. Polyak, and A.A. Tremba. D-Decomposition Technique State-of-the-Art. *Automation and Remote Control*, 69:1991–2026, 2003.

[85] Polytech Inc. Micro System Analyzer Manual, MSA-400. *Technical Brochure, Polytec Inc., www.polytec.com*.

[86] I. Y. Shen. Bending and Torsional Vibration Control of Composite Beams Through Intelligent Constrained-Layer Damping Treatments. *Journal of Smart Material Structures*, 4:340–355, 1995.

[87] A. M. Horr and L. C. Schmidt. Closed-Form Solution for The Timoshenko Beam Theory Using a Computer-Based Mathematical Package. *Computers and structures*, 55(3):405–412, 1995.

[88] A. N. Bercin and N. Tanaka. Coupled Flexural-Torsional Vibrations of Timoshenko Beams. *Journal of Sound and Vibration*, 207(1):47–59, 1997.

[89] C. Adam. Forced Vibrations of Elastic Bending-Torsion Coupled Beams. *Journal Of Sound And Vibration*, 221(2):273–287, 1999.

[90] S. H. R. Eslami-Isfahany. Use of Generalized Mass in The Interpretation of Dynamic Response of Bending–Torsion Coupled Beams. *Journal of Sound and Vibration*, 238(2):295–308, 2000.

[91] K. H. Low. On The Methods to Derive Frequency Equations of Beams Carrying Multiple Masses. *International Journal of Mechanical Sciences*, 43:871–881, 2001.

[92] D. C. D. Oguamanam. Free Vibration of Beams with Finite Mass Rigid Tip Load and Flexural-Torsional Coupling. *International Journal of Mechanical Sciences*, 45:963–979, 2003.

[93] J. R. Banerjee. Development of an Exact Dynamic Stiffness Matrix for Free Vibration Analysis of a Twisted Timoshenko Beam. *Journal of Sound and Vibration*, 270:379–401, 2004.

[94] M. Shubov. Bending-Torsion Vibration Model With Two-End Energy Dissipation. *Applied Mathematics and Computation*, 164(2):351–372, 2005.

[95] H. Gokdag and O. Kopmaz. Coupled Bending and Torsional Vibration of a Beamwith In-Span and Tip Attachments. *Journal of Sound and Vibration*, 287(3):591–610, 2005.

[96] A. Paolone, M. Vasta, and A. Luongo. Flexural–Torsional Bifurcations of a Cantilever Beamunder Potential and Circulatory Forces I. Non–Linear model and Stability Analysis. *International Journal of Non-Linear Mechanics*, 41(4):586–594, 2006.

[97] H. Salarieh and M. Ghorashi. Free Vibration of Timoshenko Beam with Finite Mass Rigid Tip Load And Flexural-Torsional Coupling. *International Journal of Mechanical Sciences*, 48(7):763–779, 2006.

[98] Y. K. Rudavskii and I. A. Vikovich. Forced Flexural–and–Torsional Vibrations of a Cantilever Beam of Constant Cross Section. *International Applied Mechanics*, 43(8):102114, 2007.

[99] D. Sun and J. K. Mills. Combined PD Feedback and Distributed Piezoelectric-Polymer Vibration Control of a Single-Link Flexible Manipulator. In *Proceedings of the 1998 IEEE/RSJ Intl. Conference on Intelligent Robots and Systems*, pages 667–672, Victoria, B.C., Canada, 1998.

[100] P. F. Pai, B. Rommel, and M. J. Schulz . Dynamics Regulation of a Skew Cantilever Plate Using PZT Patches and Saturation Phenomenon. *Journal of Intelligent Material Systems and Structures*, 11:642, 2000.

[101] Y. Morita , Y. Kobayashi, and H. Kando. Robust Force Control of a Flexible Arm with a Nonsymmetric Rigid Tip Body. *Journal of Robotic Systems*, 18(5):221–235, 2001.

[102] N. Jalili, M. Dadfarnia, F. Hong, and S. S. Ge. Adaptive Non Model-Based Piezoelectric Control of Flexible Beams with Translational Base. In *Proceedings of the American Control Conference*, pages 3802–3807, Anchorage, AK, 2002.

[103] C. H. Park. Dynamics Modelling of Beams With Shunted Piezoelectric Elements. *Journal of Sound and Vibration*, 268:115–129, 2003.

[104] C. Park and I. Chopra. Modeling Piezoelectric Actuation of Beams in Torsion. *AIAA Journal of Guidance, Control, and Dynamics*, 34,12:2582–2589, 1996.

[105] N. A. Nayfeh and W. Baumann. Nonlinear Analysis of Time-Delay Position Feedback Control of Container Cranes. *Nonlinear Dynamics*, 53:75–88, 2008.

[106] K. A. Alhazza and M. A. Alajmi. Nonlinear Vibration Control of Beams Using Delay Feedback Controller. In *12th International Congress on Sound and Vibration*, Lisbon, Portugal, 2005.

[107] N. Jalili and N. Olgac. Identification and Re-tuning of Optimum Delayed Feedback Vibration Absorber. *AIAA Journal of Guidance, Control, and Dynamics*, 23:961, 2000.

[108] A. Maccari. Vibration Control for The Primary Resonance of A Cantilever Beam by a Time Delay State Feedback. *Journal of Sound and Vibration*, 259:241, 2003.

[109] K. A. Alhazza, A. H. Nayfeh, and M. F. Daqaq. On Utilizing Delayed Feedback for Active-Multimode Vibration Control of Cantilever Beams. *Journal of Sound and Vibration*, 319:735–752, 2009.

[110] M. F. Daqaq, K. A. Alhazza, and H. N. Arafat. Non-linear Vibrations of Cantilever Beams with Feedback Delays. *International Journal of Non-linear Mechanics*, 43:962–978, 2008.

[111] K. A. Alhazza, M. F. Daqaq, A. H. Nayfeh, and D. J. Inman. Non-linear Vibrations of Parametrically Excited Cantilever Beams Subjected to Non-linear Delayed-Feedback Control . *International Journal of Non-linear Mechanics*, 43:801–812, 2008.

[112] C. Bradely, M. F. Daqaq, A. Bibo, and N. Jalili. Sensitivity Enhancement of Cantilever-Based Sensors Using Feedback Delays. *Journal of Computational and Nonlinear Dynamics*, 5:041014, 2010.

[113] A. H. Nayfeh. *Perturbation Methods*. John Wiley Interscience, New York, 1973.

[114] A. H. Nayfeh and N. A. Nayfeh. Analysis of The Cutting Tool on A Lathe. *Nonlinear Dynamics*, 2010.

[115] A. H. Nayfeh. Order Reduction of Retarded Nonlinear Systems-The Method of Multiple Scales Versus the Center-Manifold Reduction. *Nonlinear Dynamics*, 51:483–500, 2008.

[116] A. H. Nayfeh, C. Chin, and J. Pratt. Application of Perturbation Methods to Tool Chatter Dynamics. *Dynamics and Chaos in Manufacturing Processes, F. C. Moon edition*, page 193, 1997.

[117] C. Park, C. Walz, and I. Chopra. Bending and Torsion Models of Beams with Induced-Strain Actuators. *Journal of Smart Material Structures*, 5:98–113, 1996.